UNIVERSITY OF CALIFORNIA

Los Angeles

Mechanisms of Nonlinear Oscillations in Biological Control System for Locomotion

A dissertation submitted in partial satisfaction

of the requirements for the degree

Doctor of Philosophy in Mechanical Engineering

by

Yiqin Liu

2021

ABSTRACT OF THE DISSERTATION

Mechanisms of Nonlinear Oscillations in Biological Control System for Locomotion

by

Yiqin Liu
Doctor of Philosophy in Mechanical Engineering
University of California, Los Angeles, 2021
Professor Tetsuya Iwasaki, Chair

This research uncover the internal structure and control mechanisms of oscillatory biological systems, and generalizes synthesis guidelines to embed multiple desired trajectories for robotic design, with analytically determined sensory feedback gain. First we proposed an integrated CPG-leech model amenable for theoretical study, also capable of reproducing adaptive behavior of actual leech undulation in both water and air. Using this model, the internal architecture of CPG was explored, which has never been studied before. The conservative oscillator and weak coupling structure were discovered. In current state of knowledge, the mechanism that how CPGs achieve and maintain orbital stability under perturbations, and how CPGs adjust trajectories under environmental perturbations are unknown to us. This conservative oscillator and weak coupling architecture can well-explain the CPG control mechanism of stabilization and trajectory re-planning. For applications to the community, today's design of CPG controller in robotic system relies heavily on manual tuning of the the sensory feedback or mere open-loop control, lack of established theoretical support. The synthesis also needs to take the complex dynamics of the plant into consideration in the process of determining the CPG matrices, which makes the design computationally ineffi-

cient. Based on the newly-found architecture in this research, several design guidelines are generalized to embed multiple targeted orbits, with analytically determined sensory feedback gains. The weak coupling structure allow us to design CPGs only using target oscillation profile, no plant dynamics are required in calculating the connectivity matrix, making the design process direct and efficient.

The dissertation of Yiqin Liu is approved.

Jason L. Speyer

Lieven Vandenberghe

Veronica J. Santos

Jonathan Kao

Tetsuya Iwasaki, Committee Chair

University of California, Los Angeles

2021

To mom and dad

TABLE OF CONTENTS

LIST OF FIGURES

LIST OF TABLES

ACKNOWLEDGMENTS

I would first thank my advisor, Professor Iwasaki, who has been giving me caring guidance in research and life. His intelligence and mastery keeps motivating me to shoot for the stars. His humble and approachable demeanor sets an example for me to follow as a person.

I would like to thank my committee members Professor Speyer, Professor Santos, Professor Kao and Professor Vandenberghe, for giving me insightful advice on my research.

I would like to thank my family and friends, for the unconditional support, encouragement and companion, as always.

VITA

2012–2016 B.S. (Electrical Engineering), Fudan University.

PUBLICATIONS

Liu, Yiqin, and Tetsuya Iwasaki. "A Linear Perspective on Nonlinear Oscillations in Biological Control System for Locomotion." In *2019 American Control Conference (ACC)*, pp. 1336-1341. IEEE, 2019.

CHAPTER 1

Introduction

Traditional control method, as depicted in Figure 1.1, usually uses a reference signal as a function of time to specify the desired trajectory [2], [12]. Although this output regulation method has been proved effective by many [38], [39], [41], it is too rigid because we can hardly predict the exact movement of a robot . When there are perturbation, the robot may not be able to get back and stick to the step timing of the reference signal. It would be more natural to regenerate the oscillation trajectory with no dependence on the previous one. The system will lose autonomy when forced by a reference signal, which is a fixed function of time.

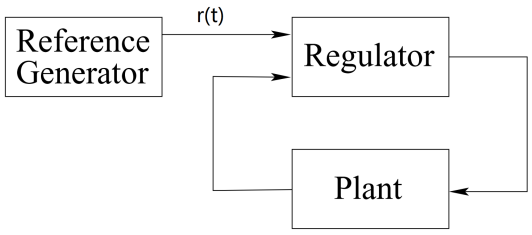

Figure 1.1: Standard control

One way to avoid using a fixed reference signal is based on the idea of hybrid zero dynamics (HZD). In [57], HZD is adopted to realize asymptotically stable walking of a five-link underactuated bipedal robot. Here they used reference signal $r(\theta)$ as a function of one of the state variables θ, by which they achieved autonomy in bipedal walking robots. For example, when the robot receives some disturbance such as tripping over a stone, it could get back to

previous stable walking gait without sticking to the step timing of the previous oscillation trajectory. So avoiding predetermined time reference signal renders the robots to be more natural and flexible in dealing with real world scenarios. However, robots with this control method can only work under one single gait specified by $r(\theta)$. Very often, robots needs to switch between different gaits. For example, when the surface of the ground changes from soil to ice, a robot may need to change the oscillation pattern of legs so that the tangential frictions on the feet are small. In this case the HZD method will not be able to switch among different oscillation patterns, which means the HZD method is unable of exploiting natural dynamics

Exploiting natural dynamics means that adjusting bodies in different gestures and gaits to be appropriate for different tasks. This is natural and necessary for animals and human. For example, when switching from walking to running, human will bend knees not only for the purpose of cushioning but also to reduce effective length of body so as to increase stride frequency. Similarly, if we could exploit natural dynamics in robots, a more efficient locomotion gait will be achieved with less energy input. A beautiful and one of the most prominent examples to exploit robot dynamics is passive dynamic walking, the concept of which was firstly introduced by [13]. It demonstrated that there exists a class of two-legged machines that can perform stable walking in startlingly human-like gaits with no active control or energy input if initiated on a slope, however, they cannot walk on level ground. Later people working in the control systems for robots solved this problem by adding compensation for the lack of gravity. [32],[42].

What is desired is a controller that possesses both functions of autonomy and natural entrainment that makes robots robust and dexterous to disturbance and seamlessly switch among optimal gaits in different situations. The answer lies in nature. Animals are born to have autonomy and natural dynamics properties, and extensive studies have been made on the topics of rhythmic behaviors and animal locomotion[27], [30], [31], [44], [45]. The controller in their neural system is called central pattern generators (CPGs). CPG-based

control can achieve desired input with small amount of control effort by exploiting the natural dynamics [55]. Robots with these kind of controllers will be extremely energy efficient. What's more, CPG-based control can manage a smooth recovery from disturbance by choosing timing flexibly, thus CPG can be an ideal solution to get rid of the dependence on time reference signal.

A CPG is an oscillator constituted by a group of neurons. It generates membrane potentials, commanding muscle contraction to reach rhythmic body movements [9],[29]. The oscillation pattern is adjusted by receiving sensory feedback so that the animal can effectively achieve desired locomotion [3], [11], [23], [34], [58], [59]. CPGs are widely existent in animals. Various CPG architectures of different animals have been discovered, including mollusks [4], lampreys [14], salamanders[26], and leeches [10], [18], [33], [43].

Some detailed mathematical models have been established using systems approach, capturing the neuronal dynamics essential for generating coordinated oscillations, and verified through numerical simulations [5], [6], [8], [35], [52]. For example, in biology, some CPG models [17], [19] utilized the detailed dynamics of neuronal cell membranes based on Hodgkin-Huxley electrical circuit[1]. The model is computationally very heavy. To reduce the computation burden, two-variable neuron models were proposed, such as FitzHugh-Nagumo and the Morris-Lecar [24]. There is a great body of biological findings of significant engineering values. However, no interpretation yet has been made systematically from engineering design, especially control, perspective. At preset, we still do not have a complete picture of how CPG could achieve adptivity and robustness, etc., which motivates this research to uncover the control mechanism behind these properties, bridging the gap between biological phenomenon and theoretical understanding as dynamical systems.

Studies have shown that CPGs are able to detect and tune into the mechanical resonance [21], [25], [46], [50], [51]. Seeing that, people have been using CPG-based controllers to achieve rhythmic locomotion with heuristic designs. For bipedal locomotion, coordinated movements were realized as a global limit cycle generated by entrainment between CPG and

rhythmic movements of a musculo-skeletal system [16]. For quadruped robots, transition from dynamic walking on irregular terrain to running on flat ground has been achieved through CPG neural oscillator network [28]. Later a framework for learning trajectories and reaching frequency adaptation by the method of using CPG as dynamic movement primitives was invented, and implemented on a bipedal robot [40]. All these research have managed to realize desired locomotion, nevertheless, the designs of CPG-based neural controllers are merely some heuristic operations of tuning parameters with some biology intuition. No underlying control mechanisms have been explored. No generalized guidelines of controller design has been established; thus, no systematic methodology can be adopted to extend the results to other relevant applications. For robots to achieve automatic gait transition, multiple limit cycles shall be embedded in the controllers. Limit cycles are well-studied and there are established methods to analyze and predict their existence [7], [15], [20], [37], [48]. However, there have not been many general theories for the design of feedback controllers to achieve multiple stable limit cycles embedding with prescribed oscillation profiles. This research addresses this open problem, making it possible to generalize CPG-based controller design embedded with multiple desired limit cycles, with analytically determined sensory feedback.

This research proposed an integrated model amenable for theoretical study, also capable of reproducing adaptive behavior of actual leech undulation in both water and air. Using this model, the internal architecture of CPG was explored, which has never been studied before. The conservative oscillator and weak coupling structure were discovered. In current state of knowledge, the mechanism that how CPGs achieve and maintain orbital stability under perturbations, and how CPGs adjust trajectories under environmental perturbations are unknown to us. This conservative oscillator and weak coupling architecture can well-explain the CPG control mechanism of stabilization and trajectory re-planning. For applications to the community, today's design of CPG controller in robotic system relies heavily on manual tuning of the the sensory feedback or mere open-loop control, lack of established

theoretical support. The synthesis also needs to take the complex dynamics of the plant into consideration, which makes the design computationally inefficient. Based on the newly-found architecture in this research, several design guidelines are generalized to embed multiple targeted orbits, with analytically determined sensory feedback gains. What's more, the weak coupling structure allow us to design CPGs only using target oscillation profile, no plant dynamics are required in calculating the connectivity matrix, making the design process direct and efficient.

The dissertation is organized as follows. In Chapter 2, to obtain a suitable model for theoretical analysis, we first simplified a fully nonlinear integrated model by approximating the nonlinearities in hydrodynamics and in delay terms. The model is validated by simulations to reproduce adaptive oscillatory behaviors observed in leeches under nominal (water) and perturbed (air) conditions.

With a model amenable for analytical study, in Chapter 3, we first established multi-variable harmonic balance (MHB) as the analytical tool for periodic motion analysis. Then an oscillation profile estimation algorithm is proposed based on MHB method, which gives decent estimation of frequency, amplitude and phase. We applied the estimation algorithm to nominal (water) and perturbed (air) cases and confirm the accuracy of the algorithm. With tools and the algorithm ready at hand, we analyzed the CPG as an input-output operator, with input being the relative joint angle ϕ and output being the torque u. Three control mechanism of CPG are proposed from leech original CPG perspective. The first one is amplitude-dependent gain of the static nonlinearity, meaning that the controller detects the outer environment variations by the amplitude change in the membrane potential v, and then adjusts to different gaits accordingly. The second mechanism is the minimum singular vector aligned with mode shape, showing how an animal locomotion exploits natural oscillation. The analysis shows that the amplitudes and phases of the minimum singular vector of controller transfer function are very close to ϕ from simulation. The third control mechanism uncovered is high gain feedback during transient, suggesting the CPG acts like a

notch filter, exporting a lot more effort during transients to stabilize the gait. In the coupled oscillator analysis, we demonstrated the connection strength of the mechanical linkage and its spatial-varying effect on the closed-loop system.

To further explore the internal architecture of CPG, in Chapter 4 we decomposed the CPG from Chapter 3 into a conservative oscillator and two feed-forward components, using LMI techniques. The conservative oscillator takes no input in the steady states, and generate membrane potential v with 360^o phase lag, which is the desired phase lag for relative joint angle ϕ for leeches. Unlike traditional control using exogenous reference generator sending out reference signal as a function of time, conservative CPG acts as an internal reference generator, and the reference is a function of system states, providing the foundation for adaptivity property. Besides the internal model structure, this decomposition also revealed the weak coupling structure, essential for stability. When the coupling is nonzero but small, the stability property is maintained due to continuity of the eigenvalues, and the CPG (reference generator) receives sensory feedback from the plant through the weak coupling so that the target oscillation pattern can be modified under perturbations. When the coupling connection is zero, the CPG acts as the exogenous reference generator which drives the plant stabilized by feedback loop. The reference tracking would be achieved by stability of the feedback system consisting of the plant and muscle stiffness component. The proof for the necessary and sufficient condition for the stability of the quasi-linear eigenstructure system is given in this chapter.

By uncovering the control mechanism of CPG from decomposition, insights are gained for designing controllers to achieve orbital stability for robotic systems, summarized in Chapter 5. We use prototype mechanical rectifier (PMR) as an example to demonstrate how one can utilize the diffusive coupling structure to design a CPG controller in a closed-loop setting. We first calculate the optimal gait for the PMR given desired rotating disc speed. For the controller synthesis, the weak coupling eigenstructure discovered in Chapter 4 made the design process a lot more straight forward than current existing methods. After specifying desired

oscillation profile $(\omega, \hat{\phi})$ of the plant, we can synthesize the conservative CPG assuming weak feedback input. This synthesis can avoid the constraints on the dynamics of either complex or simple but with low fidelity model, making the process direct. Here we show single and multiple stable limit cycles can be embedded in the CPG with only one connectivity matrix. The simulation confirms the orbital stability and adaptivity of the closed-loop CPG-PMR system. We saw automatic transition from one desired orbit to another under environmental variations, which shows the synthesized CPG demonstrated the adaptive property as in the biological CPGs.

Finally, in Chapter 6, we summarize the contributions of this research and future avenues for which this research can be expanded.

CHAPTER 2

Integrated model development

To obtain a suitable model for theoretical analysis, we first simplified a fully nonlinear integrated model by approximating the nonlinearities in hydrodynamics and in delay terms. The adaptivity and robustness properties of neuronal central pattern generator (CPG) are of great value in autonomous gait generation, stabilization, and transitions for robotic locomotion systems. Yet the feedback control mechanisms and dynamics of CPGs have not been understood well. Here, we develop a simple integrated model for leech swimming as an exemplar for analytical study of biological control principles. The model is validated by simulations to reproduce adaptive oscillatory behaviors observed in leeches under nominal (water) and perturbed (air) conditions. An algorithm using the multivariable harmonic balance (MHB) method to estimate the oscillation profile will be proposed. Based on the MHB analysis, we study the adaptive and robust behaviors achieved by the nonlinear CPG oscillator from a linear system perspective. Three properties of the biological CPG controller are revealed: amplitude-dependent transfer function of the nonlinear dynamics for embedding multi-stable limit cycles, mode shape of the target gait as the minimum singular vector of the transfer matrix, and high gain stabilization of the orbit by a spatial filter effect.

2.1 Integrated model development

For autonomous robotic systems, methods are needed for designing a controller that is robust against perturbations and capable of multi-mode operations in accordance with the environment variation. The state-of-the-art control systems are fast in speed and accurate

in precision; nevertheless, when applied to robotics, it is often considered stiff, stubborn, or even dangerous for interacting with humans.

The central pattern generator (CPG) that exists in neural control systems has been found to have the ability to be adaptive to outer environment change, and to conform oscillatory movements to natural dynamics through sensory feedback [9]. This type of neuronal CPG circuits command muscle contractions to achieve rhythmic body movements during locomotion of a wide variety of animals [29]. Various CPG architectures of different animals have been discovered, including mollusks [4], lampreys [14], and leeches [18], [33]. Some detailed mathematical models have been established using systems approach, capturing the neuronal dynamics essential for generating coordinated oscillations, and verified through numerical simulations [35], [52]. Thus, there is a full body of biological findings of significant engineering values. However, no interpretation yet has been made systematically from engineering design, especially control, perspective. At present, we still do not have a complete picture of how a CPG could achieve stable limit cycles with adaptivity and robustness.

Engineers have been using CPG-based controllers to achieve rhythmic movements for robotic locomotion with some success. For bipedal locomotion, coordinated movements were realized as a stable limit cycle generated by entrainment between CPG and rhythmic movements of a musculo-skeletal system model [16]. For quadruped robots, gait transition from dynamic walking on irregular terrain to running on flat ground, or from undulatory swimming to walking, has been achieved through neural oscillator networks [28], [49]. Some frameworks for learning trajectories and/or achieving frequency adaptation were proposed, using the CPG as dynamic motion primitives, and implemented on bipedal robots [40], [47]. All these research efforts have produced desired locomotions. Nevertheless, many of CPG-based control designs depend on some heuristic tuning of parameters. The designs are bio-inspired, but deeper understanding and exploitation of biological control mechanisms would make them more systematic and effective.

In this chapter, we will develop a simple integrated model for animal locomotion using

undulatory leech swimming as an exemplar. A previously developed model [63] assembles component dynamics into a feedback control system, encompassing the CPG [53], muscle contraction [62] through motoneuron activation [60], body-fluid interactions [61], and sensory feedback by stretch receptors. The present work simplifies the model to allow for analytical study of the control mechanisms underlying the undulatory locomotion. The simple model is validated against the original model, and is shown to be capable of reproducing the nominal swimming behavior in water as well as bi-stability of two distinct limit cycle oscillations under a perturbed environment in air.

We then apply the multi-variable harmonic balance (MHB) method [54], [56] for theoretical analysis of the model, and show that a descent estimation of oscillation profile is possible within a quasi-linear framework. Based on the MHB analysis, three control mechanism will be provided to explain an adaptive gait transition and convergence to stable limit cycles, from a systems and control perspective.

This chapter lays a foundation for uncovering the control principles behind robust and adaptive oscillations, bridging the gap between biological observations and system-theoretic concepts for dynamical feedback systems.

2.1.1 Overview

This section presents an integrated model for undulatory leech swimming. The model previously developed in [63] (Fig. 2.1) consists of several components: CPG, motoneuron activation of muscle contraction (labeled as MN), body-fluid interactions, and passive muscle dynamics (Muscle). The CPG is modeled as a chain of segmental oscillators, which gives out the membrane potentials v that oscillate with a phase coordination among the segments. Motoneuron activation translates v into neural impulse frequencies, which innervate the muscle to generate active bending moments u_A on the dorsal and ventral sides of the leech. The difference of u_A and the passive bending moments u_P, resulting from muscle stiffness and damping, gives rise to the total torques u, which, together with the hydrodynamic forces

from the environment, shapes body undulations by determining the curvature (or joint angles in the spatially discrete model) ϕ. The sensory feedback of the total torques to the CPG modifies the oscillatory activities adaptively to the outer environment.

In general, the locomotion results from dynamic interactions of the neuronal control circuits (left half of Fig.2.1) and the flexible body in fluid environment (right half). The following two sections provide mathematical descriptions of these halves obtained by simplifying the model in [63]. The definitions and values of all the model parameters are as given in the Supporting Information section of [63] except for those so described in the appendix.

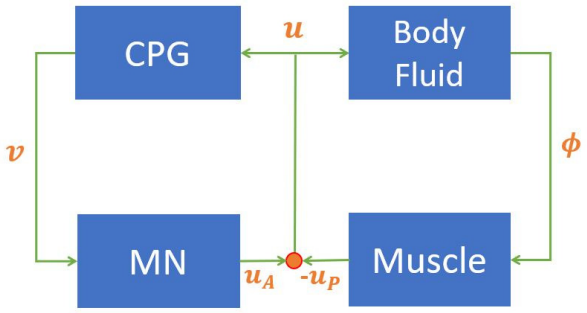

Figure 2.1: Integrated model for leech swimming

2.1.2 Flexible Body in Fluid Environment

Equations of motion for the general multi-body locomotion system can be derived using the Euler-Lagrange equation. Since the leech body as well as the nerve cord are segmented, the mechanics of the leech body is modeled as a chain of n rigid links with $n = 18$, four of which are shown in Fig. 2.2. The equations of motion for this system have been developed [36] in terms of the link angles $\theta \in \mathbb{R}^{18}$ and the velocity $(\dot{x}, \dot{y})$ of the mass center. The model adopted in [63] is based on this result in combination with a fluid force model developed specifically for leech swimming in [61].

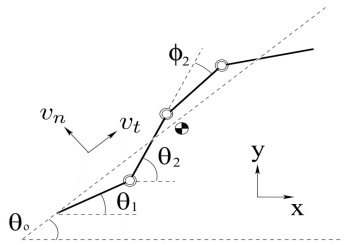

Figure 2.2: Multi-link model for slender leech body

We simplify this fully nonlinear model by assuming that the body shape remains slender during locomotion, i.e., the joint angles $\phi_i := \theta_i - \theta_{i+1}$ are small. The body frame is introduced by defining the orientation angle $\theta_o \in \mathbb{R}$ as the average of all θ_i. The velocity of the mass center $(\dot{x}, \dot{y})$ is expressed as (v_t, v_n) with the tangential and normal components in the body frame. We also assume that the normal velocity v_n is small. Our model is then obtained by applying the theoretical framework in [64] for developing and approximating a model for a general class of locomotion systems. The process is tedious but straightforward, and hence we present the simplified model without detailed derivations.

The equation of motion for leech body-fluid interaction system in body frame can be expressed as

$$\begin{aligned} &\mathcal{J}\ddot{\phi} + \mathcal{D}\dot{\phi} + v_t\mathcal{L}\phi = u, \\ &\mathfrak{j}\ddot{\zeta} + d\dot{\zeta} + v_t\lambda^\top\phi = 0, \\ &m\dot{v} + \mathcal{C}(\phi,\dot{\phi},\dot{\zeta})v + \mathcal{B}(\dot{\phi}^\top\mathcal{L}\phi + \dot{\zeta}\lambda^\top\phi) = 0, \end{aligned} \tag{2.1}$$

$$\begin{aligned} &\mathcal{J}\ddot{\phi} + \mathcal{D}\dot{\phi} + v_t\mathcal{L}\phi = u, \\ &\mathfrak{j}\ddot{\zeta} + d\dot{\zeta} + v_t\lambda^\top\phi = 0, \\ &m\dot{z} + \mathcal{C}(\phi,\dot{\phi},\dot{\zeta})z + \mathcal{B}(\dot{\phi}^\top\mathcal{L}\phi + \dot{\zeta}\lambda^\top\phi) = 0, \end{aligned} \tag{2.2}$$

where $\phi \in \mathbb{R}^{17}$ are the joint angles, $\zeta := \theta_o + q^\top\phi \in \mathbb{R}$ is the orientation variable, $v := (v_t, v_n) \in \mathbb{R}^2$ is the locomotion velocity, $u \in \mathbb{R}^{17}$ are the joint torque inputs (i.e. total muscle bending moments). The nominal values of all the parameters remain the same as listed in the Table S1 in [63], except for those described below.

The coefficients in (2.2) are given by

$$\begin{aligned}
&\mathfrak{j} := J_{22}, && d := D_{22}, && \lambda := \Lambda_{21}^\top,\\
&\mathcal{J} := J_{11} - qJ_{21}, && \mathcal{D} := (c_N/m_o)\mathcal{J}, && \mathcal{L} := \Lambda_{11} - q\Lambda_{21},
\end{aligned}$$

$$\mathcal{C} := \begin{bmatrix} nc_T + c_o\|T\phi\|^2 & -m(\dot\zeta - q^\top\dot\phi) \\ m(\dot\zeta - q^\top\dot\phi) & nc_N \end{bmatrix}, \quad \mathcal{B} := \begin{bmatrix} 1 \\ 0 \end{bmatrix},$$

with the following definitions:

$$\begin{bmatrix} J_{11} & J_{12} \\ J_{21} & J_{22} \end{bmatrix} := \begin{bmatrix} T^\top \\ e^\top \end{bmatrix} J \begin{bmatrix} T & e \end{bmatrix}, \qquad \begin{aligned} T &:= B^\top(BB^\top)^{-1},\\ q &:= J_{12}J_{22}^{-1}, \end{aligned}$$

$$\begin{aligned}
&J := (m_o\ell_o^2)(I/3 + F^\top F), \quad D := (c_N/m_o)J,\\
&\Lambda := c_o\ell_o F^\top, \quad F := TA, \quad c_o := c_N - c_T,\\
&\ell_o := \ell/(2n), \quad m_o := m/n, \quad e := \begin{bmatrix} 1 & \cdots & 1 \end{bmatrix}^\top,\\
&A := \begin{bmatrix} I & o \end{bmatrix} + \begin{bmatrix} o & I \end{bmatrix}, \quad B := \begin{bmatrix} I & o \end{bmatrix} - \begin{bmatrix} o & I \end{bmatrix},
\end{aligned}$$

where o is the $n-1$ dimensional zero vector, and Λ_{ij} and D_{ij} with $i,j = 1,2$ are defined for Λ and D by the same congruence transformation as in J_{ij}.

Newly added parameters for the integrated model are

$$\begin{aligned}
&c_T := 5.4c_t\ell_o\sqrt{\rho\mu d|v_N|}, && c_t := 0.44,\\
&c_N := c_p\rho d\ell_o|v_N|, && v_N := 0.03 \text{ m/s},\\
&\wp := -\delta a_o r\mu_m\alpha\alpha_o, && a_o = 5.7,\\
&k_m := \mu_m d_o(1+\alpha f_b)nr^2/\ell, && d_o := 106.8,\\
&c_m := 2nr^2c/\ell.
\end{aligned}$$

and g_k and t_{d_k} are defined by

$$e^{-j\omega k\tau_d} = \frac{g_k}{1 + j\omega t_{d_k}}, \quad \omega = 2\pi/0.391,$$

for $k = 1, \ldots, 5$. In the above, c_t was modified from 0.6, while the same values for a_o and d_o were implicitly used in [63]. The sensory feedback gains $(\varsigma_1, \ldots, \varsigma_{17})$ in the new model are equal to 20/19 times the values in [63].

The output signal is defined to be the passive muscle bending moment $u_P \in \mathbb{R}^{17}$ given by

$$u_P = c_m\dot{\phi} + k_m\phi, \tag{2.3}$$

where c_m is the muscle damping coefficient, and k_m is the bending stiffness. The input u is given as the total effect of the active and passive moments $u = u_A - u_P$, where the active moments u_A are determined by the neural control system described in the next section.

During the simplification process to arrive at the above model, the nonlinear model of the hydrodynamic forces in [63] has been approximated by a linear model. In particular, the hydrodynamic forces in the tangential and normal directions on each link are originally modeled as

$$\begin{aligned} \hbar_{t_i} &= c_{T_i} v_{t_i}, \quad & c_{T_i} &:= 2.7 c_t (\ell/n)\sqrt{\rho\mu d|v_{n_i}|}, \\ \hbar_{n_i} &= c_{N_i} v_{n_i}, \quad & c_{N_i} &:= 0.5 c_p \rho d(\ell/n)|v_{n_i}|, \end{aligned}$$

where v_{t_i} and v_{n_i} are the tangential and normal components of the velocity of the i^{th} link, which depend on the generalized coordinates. In our new model, we set $|v_{n_i}| = 0.03$ m/s, an approximate value from nominal swimming, so that c_{T_i} and c_{N_i} are constant and uniform over the body, i.e. the same value for all i, denoted by c_T and c_N. The tangential fluid drag coefficient c_t is then tuned so that the nominal water swimming simulation will have the steady state speed close to the observed speed in [63]. As a result, the value is revised from $c_t = 0.6$ to 0.44 here.

2.1.3 Neuronal Control Circuits

The CPG and MN dynamics are described in [63] as

$$\begin{aligned} v_i = F(s)\varphi(v_i) - h_i u_i + \epsilon \sum_{k=1}^{z} d_k(s) D\varphi(v_{i-k}) \\ +\epsilon \sum_{k=1}^{z} d_k(s) A\varphi(v_{i+k}), \end{aligned} \tag{2.4}$$

$$u_{A_i} = N(s) v_i \tag{2.5}$$

for $i = 1, \ldots, \aleph$, where $v_i = 0$ when $i < 1$ or $i > \aleph$, and

$$F(s) := \frac{\mu_\gamma}{1+\tau_\gamma s}\begin{bmatrix} 0 & -1 & 0 \\ 0 & 0 & -1 \\ -1 & 0 & 0 \end{bmatrix}, \quad h_i := \begin{bmatrix} 0 \\ 0 \\ \varsigma_i \end{bmatrix},$$

$$D := \begin{bmatrix} 2 & 0 & 0 \\ 0 & 0 & 0 \\ 0 & 0 & 0 \end{bmatrix}, \qquad A := \begin{bmatrix} 0 & -1 & 0 \\ 0 & 0 & -1 \\ 0 & 0 & 0 \end{bmatrix},$$

$$\varphi(x) := \sigma \tanh(x/\sigma), \quad \mu_\gamma := (1-\gamma)\mu, \quad \tau_\gamma := (1-\gamma)\tau,$$

$$N(s) := \frac{d_M(s)}{1+\tau_c s} \cdot (1 - \frac{\beta_o}{1+\tau_o s}) \begin{bmatrix} \wp & 0 & 0 \end{bmatrix}.$$

The details of this model are given in [63]. Here we provide a brief explanation of this model and present our simplifying modifications.

The CPG is a chain of $\aleph$ segmental oscillators ($\aleph = 17$), each of which comprises three neurons with the membrane potentials $v_i(t) \in \mathbb{R}^3$ for segment i. The neurons within each segment are connected in a recurrent cyclic inhibition loop, described by $F(s)$. The low pass filter in $F(s)$ describes the synaptic dynamics, where the parameter γ is the excitatory (constant) input from the gating neurons to modify the coupling strength μ and time constant τ. The hyperbolic tangent function $\varphi(x)$ describes the threshold effect of the synapse, and acts on its vector-valued argument elementwise. The segmental oscillator receives the local bending moment $u_i(t) \in \mathbb{R}$ as the sensory feedback signal. The third and fourth terms in (2.4) represent the intersegmental neuronal connectivity that projects up to z segments away ($z = 5$) with communication delay $d_k(s)$. The active bending moment $u_{A_i}(t) \in \mathbb{R}$ is generated from $v_i(t)$ through the motoneuron activation dynamics $N(s)$, which contains the adaptation effect with time constant τ_o and muscle activation delay $d_M(s)$ and time lag τ_c.

To avoid the infinite dimensionality problem in the state space analysis, here we replace the pure time-delay terms in [63] by rational transfer functions:

$$d_M(s) = e^{-\tau_a s} \cong \frac{1-\tau_a s}{1+\tau_a s}, \quad d_k(s) = e^{-k\tau_d s} \cong \frac{g_k}{1+t_{d_k} s}.$$

A Padé-like approximation is used for the muscle activation delay $d_M(s)$, which is an all-pass filter with gain 1 and phase close to that of $e^{-\tau_a s}$ at the swim frequency. The neural communication delay $d_k(s)$ is replaced by a first-order low-pass filter since the Padé approximation will cause problematic algebraic loops in (2.4). The parameters g_k and t_{d_k} are chosen so that the approximation becomes exact at an observed nominal water swimming frequency ($\omega = 2\pi/0.391$ rad/s).

With these modifications, the phase lag of the joint angles ϕ is found to be 355° from head to tail when the closed-loop system is simulated under the nominal water condition. To make the phase lag match more closely the value in [63], which is 360°, the sensory feedback gains ς_i are scaled up by a factor 20/19. Thus, the values we use here are slightly larger than those in [63] but this additional modification is not essential for the result reported here.

2.2 Model validation

2.2.1 Overview

The simple model is validated against the original model, and is shown to be capable of reproducing the nominal swimming behavior in water as well as bistability of two distinct limit cycle oscillations under a perturbed environment in air.

Closed-loop simulations are performed for three cases to validate the simplified integrated model against the original model in [63]:

Case 1. Nominal swimming in water.

Case 2. Undulation in air with the initial condition on the nominal swimming orbit in water.

Case 3. Undulation in air with the initial condition away from the nominal swimming orbit in water.

For the "air swimming" conditions (Cases 2 and 3), the fluid drag coefficients (c_T, c_N) are simply set to zero.

Table 2.1 gives a summary of the simulation results, where the first row of each case is the result of the original model in [63], and the second row in bold is the result of the simplified model. The amplitude and phase lag of ϕ are calculated by the first term of the Fourier series; the average over the body for the former and the difference between head and tail for the latter. Although the drag coefficient c_t in the new model is tuned to match the swim speed only, we see that the new model is able to accurately reproduce nominal swimming in terms of other parameters as well. For the other two cases of air swimming, similar behaviors are maintained after the simplification of the model.

Table 2.1: Comparison of original and simplified models

Case	Period [ms]	ϕ Amplitude	ϕ Phase lag	Speed [m/s]
1	391	10.00°	360°	0.1257
	393	**10.02°**	**360°**	**0.1258**
2	398	10.52°	331°	-
	395	**10.62°**	**336°**	**-**
3	490	16.75°	−38°	-
	488	**16.37°**	**−11°**	**-**

1: nominal water; 2: air, traveling wave; 3: air, standing wave

The gait of oscillatory body motion under these three different conditions can be visualized in terms of the joint angles ϕ and the body snapshots as in Fig. 2.3. The first two sets of snapshots are very similar in shape, exhibiting body waves traveling down from head (left) to tail (right), except that the body in water is moving toward left due to the hydrodynamic force. The snapshots for the third case show that the leech is undulating in "C" shape with standing waves, corresponding to the roughly synchronized oscillations of relative joint

angles ϕ shown above the snapshots.

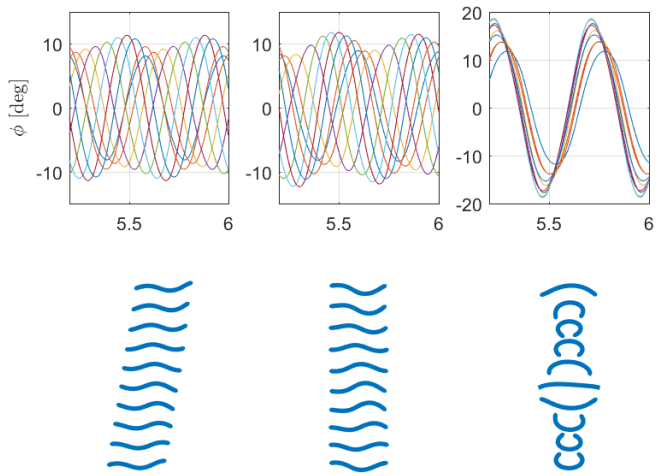

Figure 2.3: Relative joint angles $\phi(t)$ (top) and corresponding body snapshots (bottom). Case 1 (left): Nominal swimming in water, Case 2 (middle): Traveling waves in air, Case 3 (right): Standing waves in air.

The two undulation modes resulted from different initial conditions in the same air environment suggests that the CPG achieves bistability of two limit cycles and has the properties of robustness and adaptivity; Case 2 shows that the CPG can maintain in air an undulatory gait similar to that for nominal swimming in water, while Case 3 shows that the gait transition is possible when the environment changes. Thus, the simplified model demonstrates capabilities of the leech CPG to defend against perturbation and robustly maintain the nominal gait, and also to adapt the gait to outer environment changes and modify the oscillation profile. These properties were observed in leech experiments and reproduced in the original model [63], and here we show that they are preserved in our simplified model. The result will be examined more quantitatively in the following subsections.

2.2.2 Nominal Water Swimming Case

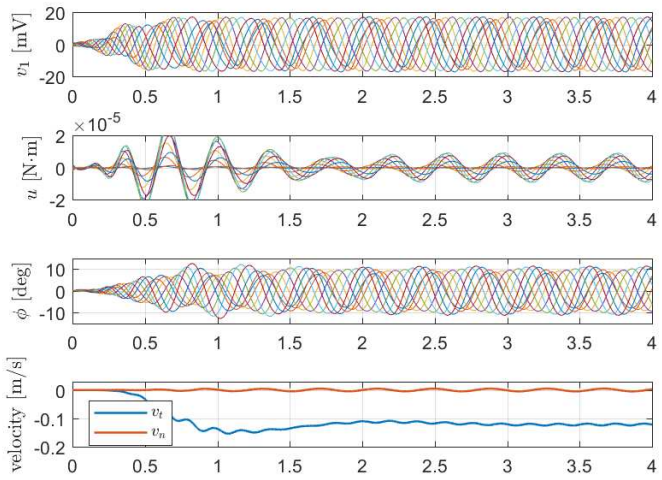

Figure 2.4: Nominal swimming in water. Membrane potentials v_1, total torques u, relative joint angles ϕ and velocity (v_t, v_n)

The time courses of some variables in the closed-loop simulation are shown in Fig. 2.4. Here, $v_1 \in \mathbb{R}^{17}$ are the membrane potentials of the first neurons of the 17 segments ($v_{1_i} = v_{i_1}$). We see the convergence of the trajectory to a periodic orbit within several cycles of undulation. In the third plot of Fig. 2.4, ϕ are almost evenly distributed over time, meaning the phases of the joint angles ϕ_i decreases linearly from head to tail with the total lag close to 360°. This phase property indicates that the leech is undulating with the wavelength roughly equal to the body length, consistently with the observed result in experiment.

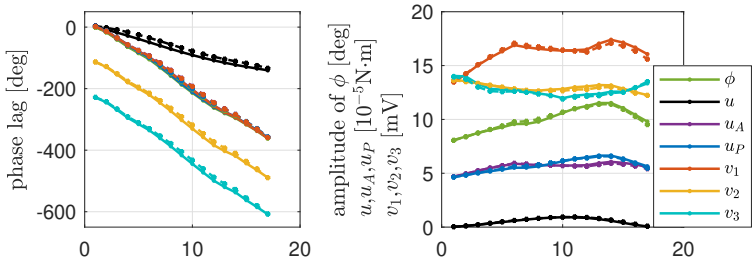

Figure 2.5: Phase and amplitude (Case 1: nominal water)

A detailed comparison of the oscillation profiles between the results of the original model

in [63] and our simplified model is given in Fig. 2.5, in dashed and solid lines respectively, plotting the phasors[1] of some variables. From the overlap of the dashed and solid curves, we confirm the accurate reproduction of nominal swimming behavior by our new model. In the phase plot, the phase lag of u_A, u_P, v_1 and ϕ are almost identical, overlapping on top of each other; in the amplitude plot on the right, we see that each of the pairs (ϕ, u_P) and (v_1, u_A) share the same shape. The reason behind the matching of the shapes for each pair is seen in (2.3) and (2.5); each entry in phasor vectors $\hat{\phi}$ and $\hat{v}_1$ is magnified by the same scalar gain $K(j\omega)$ and $N(j\omega)$ to produce $\hat{u}_P$ and $\hat{u}_A$, respectively, where

$$K(s) := c_m s + k_m$$

is the transfer function of the passive muscle dynamics, and ω is the swim frequency. The phase curves of each pair appear to overlap because the phase angles of $K(j\omega)$ and $N(j\omega)$ are small; roughly 3° and -8°. On the other hand, the overlap of the phase curves for ϕ and v_1 may be closely related to the CPG control mechanism. For example, this may suggest that the CPG acts as an internal model of the body-fluid dynamics so that v_1 "estimates" ϕ from input u.

2.2.3 Air Swimming Cases

For Case 2, the leech is placed in water at the beginning, simulated as in Fig. 2.4, then is pulled up into air at time instant $t = 4$ s, and simulated with $c_T = c_N = 0$ until a steady state is reached. The result displayed in Fig. 2.6 shows that the trajectory converges to another stable limit cycle in the air environment, which shares a similar but not identical oscillation profile to the one in the nominal water swimming condition. This indicates that the CPG controller demonstrates good robustness under perturbation.

[1]The phasor $\hat{x} \in \mathbb{C}^n$ of a T-periodic signal $x(t) \in \mathbb{R}^n$ is defined by $\hat{x}_i := a_i e^{jb_i}$ where $a_i, b_i \in \mathbb{R}$ are the amplitude and phase of the sinusoidal approximation $x_i(t) \cong a_i \sin(\omega t + b_i) + c_i$ using the Fourier series, where $\omega := 2\pi/T$. All the signals in this chapter oscillate with nearly zero bias ($c_i \cong 0$). The amplitude a_i and phase b_i are plotted in Fig. 2.5 and other figures with the time axis shifted to normalize the phase for $\phi_1(t)$ to zero. We will use the "hat" notation $\hat{x}$ to denote the phasor of $x(t)$.

For Case 3, we mimicked the leech being placed in air for the same set of parameter values as Case 2, but with the initial condition chosen away from the limit cycle orbit of the nominal water swimming. It is observed that the trajectory converges to a stable limit cycle whose oscillation profile (Fig. 2.7) is very different than the nominal water swimming gait; undulation frequency becomes 23.4% larger (from 397ms to 490ms), and the phase lag of ϕ drops from 360° to less than 40°, meaning that all of the 18 links are flapping up and down almost synchronously.

The simulated behaviors of the simplified model (solid curves) are reasonably close to those of the original model (dashed curves) as seen in Figs. 2.6 and 2.7, and the new model is thus validated under the perturbed conditions.

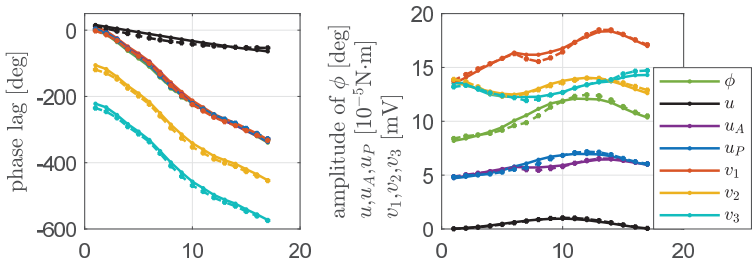

Figure 2.6: Phase and amplitude (Case 2: air, traveling wave)

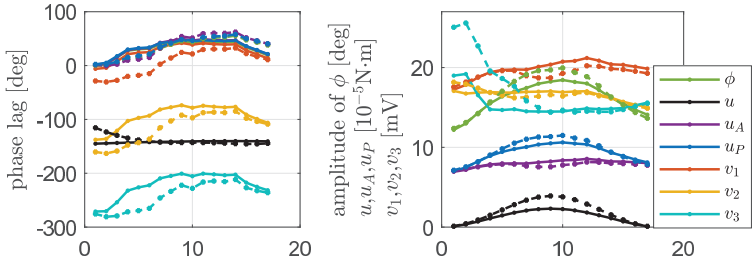

Figure 2.7: Phase and amplitude (Case 3: air, standing wave)

2.3 Summary

The leech swimming CPG has demonstrated good adaptive and robust properties. Motivated by the desire for designing controllers capable of autonomous transitions or robust stability

of limit cycles for robotic systems, we first simplified a fully nonlinear integrated model which captures observed leech behaviors well. The resulting model is more amenable to analytical study, and can reproduce almost identical behaviors as the original model under nominal water and perturbed air conditions. To analyze the closed-loop system, we proposed a numerical algorithm to solve the MHB equation and estimate the oscillation profile. The MHB analysis allowed for study of CPG control mechanisms from the quasi-linear perspective using the controller transfer function $C(s)$. We have found that (i) the neuronal threshold nonlinearity acts as amplitude-dependent gains to adjust $C(s)$ and achieve robustness and adaptivity, and (ii) the CPG control acts as a spatial notch filter to block the desired mode shape by aligning it with the minimum singular vector of $C(s)$, with high-gain feedback under perturbation for fast recovery. These analysis provides insights for designing CPG-inspired controllers.

CHAPTER 3

Analysis of coupled CPG-Body-Fluid system

3.1 Oscillation profile analysis

To analyze the closed-loop system, we proposed a numerical algorithm to solve the MHB equation and estimate the oscillation profile. Applying the MHB method to the leech swimming model for the three cases, we get estimated oscillation profiles $(\omega, \hat{x})$ and their accuracy is evaluated in comparison with the simulated results. The comparison shows that a descent estimation of oscillation profile is achieved within a quasi-linear framework.

3.1.1 MHB method

With a validated model, now we could perform analytical study which cannot be done with the model in [63]. The multivariable harmonic balance (MHB) method will be adopted for estimating the profile of oscillation (i.e. frequency, amplitude, phase) with sinusoidal approximations. While simulations can determine the oscillation profile directly as was done in the previous section, the value of the MHB method is to provide a means to analyze the CPG control mechanism in the linear framework once the accuracy of the MHB estimation is confirmed.

First, we approximate the locomotion speed v_t by a constant $v_o = 0.1258$ m/s, which is the average value obtained by simulation (see Table 2.1). Then with (2.3) and the first equation in (2.2), the flexible body side of the system in Fig. 2.1 is linear, and the closed-loop system

with the neural control (2.4) and (2.5) can be described as

$$\dot{x} = \mathsf{A}x + \mathsf{B}\varphi(v), \quad v = \mathsf{C}x \tag{3.1}$$

for some appropriately defined matrices $(\mathsf{A}, \mathsf{B}, \mathsf{C})$, where v is the vector obtained by stacking $v_1, \ldots, v_{17}$ in a column, and x contains ϕ, $\dot{\phi}$, and the states for $F(s)$, $d_k(s)$, and $N(s)$.

Next we approximate the nonlinearity φ by the gain

$$\kappa(a) = \frac{2}{\pi a} \int_0^\pi \varphi(a \sin\theta) \sin\theta d\theta, \tag{3.2}$$

which is the describing function [22]. In particular, when the input $w(t) \in \mathbb{R}$ is a sinusoidal signal with amplitude a, the output $\varphi(w)$ is approximated by its first harmonic $\kappa(a)w$. Assuming that $v(t) \in \mathbb{R}^{51}$ are close to sinusoids of amplitudes $\alpha \in \mathbb{R}^{51}$, the closed-loop system (3.1) is quasi-linearized as

$$\begin{aligned} &\dot{x} = (\mathsf{A} + \mathsf{B}\boldsymbol{\kappa}(\alpha)\mathsf{C})x, \\ &\boldsymbol{\kappa}(\alpha) := \mathrm{diag}(\kappa(\alpha_1), ..., \kappa(\alpha_{51})). \end{aligned} \tag{3.3}$$

A harmonic solution $x(t) = \Re[\hat{x}e^{j\omega t}]$ satisfies this equation if and only if

$$j\omega\hat{x} = (\mathsf{A} + \mathsf{B}\boldsymbol{\kappa}(\alpha)\mathsf{C})\hat{x} \tag{3.4}$$

holds, which is the MHB equation. We can obtain an estimated frequency and the phasor of state variables $(\omega, \hat{x})$ by solving the MHB equation subject to the constraint $|\mathsf{C}\hat{x}| = \alpha$.

We propose the following algorithm for solving the constrained MHB equation. The solution is not unique in general, and the algorithm searches for the solution $(\omega, \hat{x})$ that gives the phasor $\hat{\phi} := \mathsf{D}\hat{x}$ close to $\hat{\phi}_o$, where matrix D is defined to select ϕ from x by $\phi = \mathsf{D}x$, and $\hat{\phi}_o$ is the complex vector $\hat{\phi}_o := \mathsf{D}\hat{x}_o$ defined in terms of an initial guess $\hat{x}_o$ of the phasor $\hat{x}$. Later in the analyses, $\hat{x}_o$ is chosen to be the phasor of $x(t)$ from the simulation of the fully nonlinear closed-loop system for Case 1, 2, or 3 as described in Section 2.2.

Algorithm:

0. Let ε_1 and ε_2 be small positive numbers, ε_o be a real number such that $0 < \varepsilon_o < 1$; initialize (l_b, u_b) so that $0 < l_b < u_b$; initialize $\mathcal{K}_0 := \mathcal{K}(|\mathsf{C}\hat{x}_o|)$. Let $\hat{x}_o$ be a complex vector such that the first entry of $\hat{\phi}_o := \mathsf{D}x_o$ is a positive real number.

1. Let $\mathfrak{a} = (u_b + l_b)/2$ and $k = 1$.

2. Solve the minimization problem:

$$\begin{aligned} \min_{(\lambda,\hat{x})} \quad & \|\mathsf{D}\hat{x} - \hat{\phi}_o\| \\ \text{s.t.} \quad & \lambda\hat{x} = (\mathsf{A} + \mathsf{B}\mathcal{K}_{k-1}\mathsf{C})\hat{x}, \\ & \|\hat{x}\| = \mathfrak{a}, \quad \hat{\phi} := \mathsf{D}\hat{x}, \quad \Im(\hat{\phi}_1) = 0. \end{aligned}$$

   Let $(\lambda_k, \hat{x}_k)$ be the optimizer and update

$$\mathcal{K}_k = \mathcal{K}_{k-1} + \varepsilon_o\Delta_k, \quad \Delta_k := \mathcal{K}(|\mathsf{C}\hat{x}_k|) - \mathcal{K}_{k-1}.$$

3. If $\|\Delta_k\| \geq \varepsilon_1$, increment k and go to Step 2.
   If $\|\Delta_k\| < \varepsilon_1$, then update the upper or lower bound:

$$\begin{cases} u_b = \mathfrak{a} & \text{if} \quad \Re(\lambda_k) < 0, \\ l_b = \mathfrak{a} & \text{if} \quad \Re(\lambda_k) \geq 0, \end{cases}$$

   and go to Step 4.

4. If $u_b - l_b \geq \varepsilon_2$, go to Step 1 and iterate. Otherwise, stop; The eigenvalue λ_k is (approximately) on the imaginary axis, and let ω be the imaginary part of λ. Then $(\omega, \hat{x}_k)$ is the solution satisfying (3.4) and $|\mathsf{C}\hat{x}| = \alpha$.

The idea behind the algorithm is as follows. We start with (l_b, u_b), an initial guess for the upper and lower bounds on the norm of the solution $\hat{x}$. With a fixed magnitude $\mathfrak{a}$ at the middle point of the interval (l_b, u_b), the inner loop (Steps 2-3) searches for $(\lambda, \hat{x})$ such that they are the eigenvalue/eigenvector pair of matrix $\mathsf{A} + \mathsf{B}\mathcal{K}(|\mathsf{C}\hat{x}|)\mathsf{C}$ with magnitude $\|\hat{x}\| = \mathfrak{a}$ that gives $\mathsf{D}\hat{x}$ closest to $\hat{\phi}_o$. With $\varepsilon_o = 1$, the inner loop is a fixed-point iteration on $\mathcal{K}_k$,

which we often found to be divergent (or continuously fluctuating). Choosing a smaller value for ε_o, the error $\|\Delta_k\|$ can be made to decrease and converge to zero. If ε_o is chosen too small, $\|\Delta_k\|$ will be decreasing but convergence is slow. Hence ε_o should be chosen properly to adjust the rate of convergence.

The outer loop (Steps 1-4) iterates on the amplitude $\mathfrak{a}$ through a bisection search to move λ onto the imaginary axis. On exit from the inner loop, $\Re(\lambda_k)$ is seen as a function of $\mathfrak{a}$, and the implicit assumption is that $\mathfrak{a}$ and $\Re(\lambda_k)$ are negatively correlated, which was found to be true for all three cases of our analyses. However, in other scenarios positive correlation is equally possible, and in such case, the update rule for u_b and l_b in Step 3 should be swapped. With the outer loop iteratively narrowing down the range (l_b, u_b) by bisection, we eventually solve the MHB equation with the numerical accuracy set by ε_1 and ε_2.

3.1.2 Results for undulations in water and air

Applying the MHB method to the leech swimming model for the three cases, we get estimated oscillation profiles $(\omega, \hat{x})$ and their accuracy is evaluated in comparison with the simulated results in Section 2.2.

In Figs. 3.1–3.3, the solid lines are phase lag and amplitude of phasors of signals estimated by the MHB method, and the dashed lines are those from simulations of our integrated model. For all cases, the MHB method gives reasonable estimations of the oscillation profile. The phase estimates, in particular, are especially accurate. The amplitude estimates are about 8% off, but the shapes of the curves (i.e. distribution over the body) are fairly accurate. The error may be attributed to the fact that the amplitudes of v are more than 10 mV while the nonlinearity $\varphi(v)$ saturates at $\sigma = 20/3$, resulting in significant distortion from sinusoids.

Figure 3.4 shows the eigenvalues of the quasi-linear system (3.3) in the vicinity of the oscillation mode $j\omega$ found by the algorithm (marked red). It has been shown [56] that orbital stability of the limit cycle corresponding to the estimated oscillation $(\omega, \hat{x})$ can be

expected from the marginal stability of the quasi-linear system, i.e., all the eigenvalues of $\mathsf{A} + \mathsf{B}\mathcal{K}(|\mathsf{C}\hat{x}|)\mathsf{C})$ being in the open left half plane except for a pair on the imaginary axis. The eigenvalue distribution in Fig. 3.4a indicates the marginal stability, and is consistent with the expectation.

The eigenvalue distributions in Fig. 3.4b and 3.4c are similar to each other. This is reasonable since both cases share the same system matrices $(\mathsf{A}, \mathsf{B}, \mathsf{C})$ for the air swimming condition. The only difference in the quasi-linear system is the amplitude of $\hat{v} := \mathsf{C}\hat{x}$. We see that the standing wave is expected to be stable due to the marginal stability, while the traveling wave is not due to the eigenvalue in the right half plane, giving a counter example to the expectation as this oscillation is stable when simulated. The eigenvector corresponding to the eigenvalue to the right of the red circle in Fig. 3.4b has a similar mode shape to $\hat{\phi}$ for the standing wave; likewise, the eigenvector corresponding to the eigenvalue to the immediate left of the red circle in Fig. 3.4c has a similar mode shape to $\hat{\phi}$ for the traveling wave.

3.2 CPG analysis as input-output operator

Given that the MHB method is able to make reasonable predictions of $\hat{x}$, now we can analyze the CPG control mechanisms using the transfer functions between ϕ and u based on the MHB result.

The closed-loop system with the fixed constant speed $v_t(t) \equiv v_o$, which was assembled into the state space form in (3.1), is given by

$$\begin{aligned} &\mathcal{J}\ddot{\phi} + \mathcal{D}\dot{\phi} + v_o\mathcal{L}\phi = u, \\ &v = M(s)\varphi(v) + Hu, \\ &u = N(s)v - K(s)\phi, \end{aligned} \tag{3.5}$$

where $M(s)$ and H are properly defined to describe (2.4). In terms of transfer functions, the

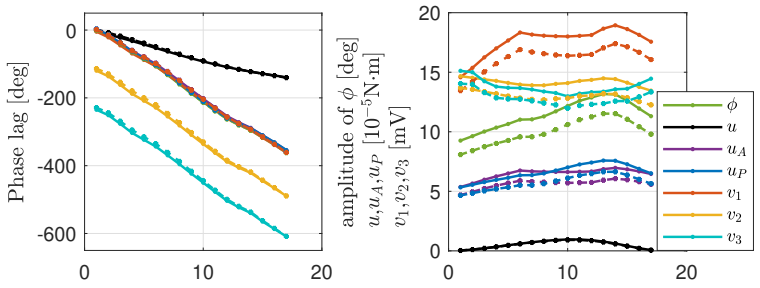

Figure 3.1: Oscillation profile for Case 1 (nominal water).

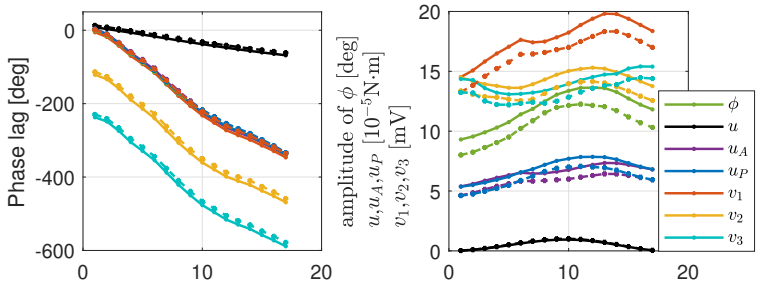

Figure 3.2: Oscillation profile for Case 2 (air, traveling wave).

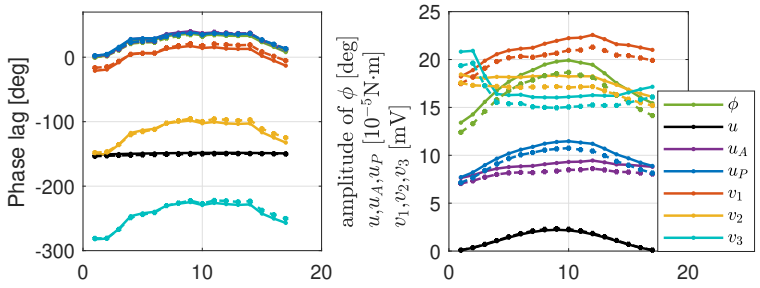

Figure 3.3: Oscillation profile for Case 3 (air, standing wave).

system is described as

$$
\begin{aligned}
&Q(s)\phi = u, \quad u = C(s)\phi, \\
&Q(s) := \mathcal{J}s^2 + \mathcal{D}s + v_o\mathcal{L}, \\
&C(s) := (N(s)\big(I - M(s)\kappa(\alpha)\big)^{-1}H - I)^{-1}K(s),
\end{aligned}
$$

where the CPG controller is quasi-linearized using the describing function $\varphi(v) \cong \kappa(\alpha)v$. The feedback system can be visualized through the block diagram in Fig. 2.1, where $Q(s)^{-1}$ represents the "Body Fluid" module, and $C(s)$ represents the rest of modules combined.

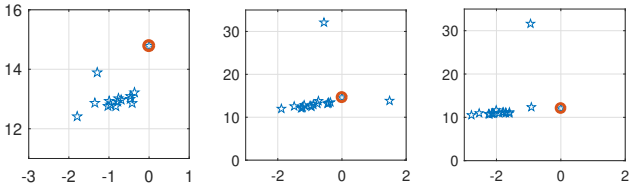

(a) Water swimming (b) Air traveling (c) Air standing

Figure 3.4: The eigenvalue (red) corresponding to the eigenvector whose phase lag is the most similar to $\hat{\phi}$

A naive guess for the role of CPG controller is acting like a PD controller during steady state.

Define

$$A_{cl} := \begin{bmatrix} 0 & I \\ -\mathcal{J}^{-1}(v_o\mathcal{L} - R_o) & -\mathcal{J}^{-1}(\mathcal{D} - I_o) \end{bmatrix}$$

where

$$R_o := \Re[C(j\omega)], \quad I_o = \Im[C(j\omega)/\omega].$$

Fig. 3.5 is the eigenvalue distribution of A_{cl} for the water swimming case. It does not satisfy the condition that all the eigenvalues of closed-loop A_{cl} matrix are in OPLH, thus it is clear that a PD controller could not stabilize the system during steady states. Some more advanced control mechanisms are functioning behind.

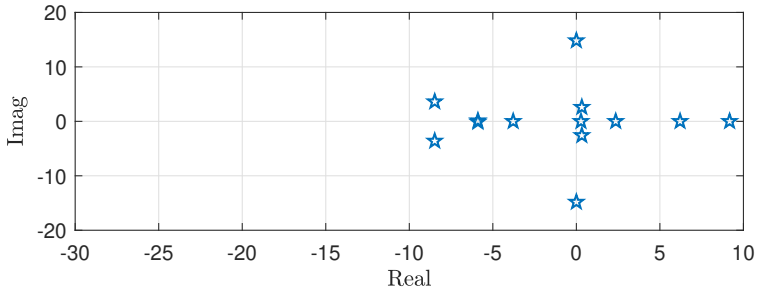

Figure 3.5: $C(s)$ acts more than a PD controller in steady state

3.2.1 Amplitude-dependent gain of the static nonlinearity

For all three conditions that were simulated, the CPG controller remained the same. Yet, two different plants (in water and air) exhibited similar traveling wave gaits (Cases 1 and 2), and an identical plant (in air) exhibited two limit cycles of traveling and standing waves (Cases 2 and 3). From the quasi-linear perspective, these robust and adaptive behaviors are accomplished by the change of α in the describing function, which are the amplitudes of the first harmonics of v. The approximate "gain" $\mathcal{K}(\alpha)$ of the static nonlinearity $\varphi(v)$ is adjusted by the amplitude, which results in modification of the controller transfer function $C(s)$ via the amplitude-dependent mechanism. The controller detects the outer environment variations by the amplitude change in v, and then adjusts to different gaits accordingly.

3.2.2 Minimum singular vector aligned with mode shape

An important question often posed in biology is whether an animal locomotion exploits natural oscillation. If the body-fluid dynamics were conservative (with negligible "damping" effect), the first equation in (3.5) with $u = 0$ would have a periodic solution ϕ. If the CPG controller adopts this solution as an undulatory gait, then $\hat{u} = C(j\omega)\hat{\phi} = 0$ should hold in the steady state, and the phasor $\hat{\phi}$ would be in the null space of the controller $C(j\omega)$. In reality, the damping of the system could not be neglected, and some control effort u is required to cancel the damping effect. This motivates us to compare the simulated gait $\hat{\phi}$ with the singular vector of $C(j\omega)$ associated with the minimum singular value.

Figures 3.6–3.8 show the amplitudes and phases of the minimum singular vector $\eta \in \mathbb{C}^{17}$ of $C(j\omega)$ in comparison with the simulated phasor $\hat{\phi}$ for Cases 1–3. The singular vector is not unique due to the freedom of scalar multiple $p \in \mathbb{C}$, and is set as $\eta = p\eta_o$ where η_o is a given singular vector and p is fixed so that $\|\hat{\phi} - p\eta_o\|$ is minimized.[1] The phase lag of the

[1]Since the first entry of η_o has an unreasonably high amplitude, it is treated as an outlier and excluded

minimum singular vector is independent of p and is very similar to the phase lag of $\hat{\phi}$, which essentially determines the undulatory gait of the rhythmic locomotion. The snapshots of animation created by the time-domain signals recovered from minimum singular vectors are also shown in the figures. We see the oscillatory gaits are very close to those snapshots from simulation in Fig. 2.3.

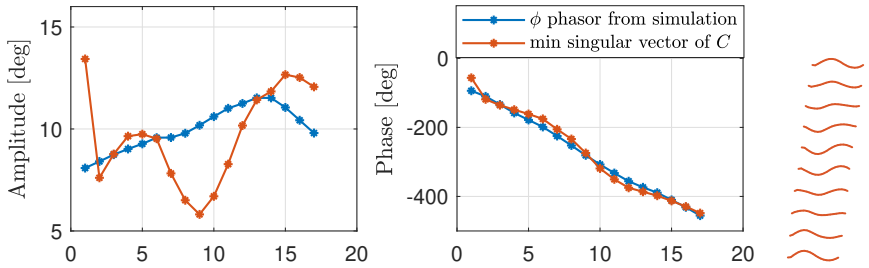

Figure 3.6: Min singular vector for Case 1 (nominal water)

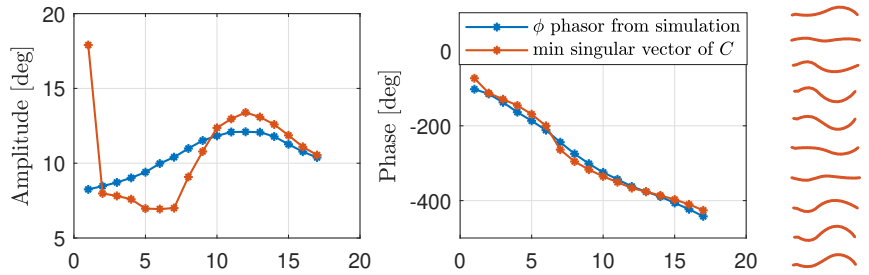

Figure 3.7: Min singular vector for Case 2 (air, traveling wave)

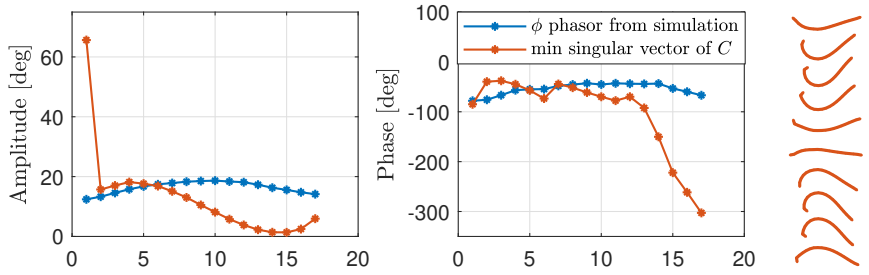

Figure 3.8: Min singular vector for Case 3 (air, standing wave)

from the calculation.

3.2.3 High gain feedback during transient

The singular vector analysis suggests that the CPG control may exploit the natural dynamics. If so, the role of the controller would be to cancel the damping effect adversary to locomotion. To examine this expectation, let us look at the surf plots of the magnitudes of $\omega\mathcal{D}$, $Q(j\omega)$ and $C(j\omega)$ in Fig. 3.9. If all the controller does is to cancel the damping effect as expected, then the magnitude of $C(j\omega)$ should be comparable to that of $Q(j\omega)$ and/or $\omega\mathcal{D}$. However, the peak magnitude of $C(j\omega)$ is more than 10 times larger than those of $\omega\mathcal{D}$ and $Q(j\omega)$. This suggests that the controller uses high-gain feedback to stabilize the gait during transient.

This can be seen from the time-domain signal of control effort. In the second plot in Fig. 2.4, from $t = 0.4$ s to 1.5 s the amplitude of $u(t)$ is about 3 three times larger than the amplitude in steady state, indicating that the controller is doing more than just canceling the damping effect. From the plots of the muscle bending moments for the nominal swimming case (Fig. 3.10), we see that the amplitudes of $u_A(t)$ and $u_P(t)$ are comparable to each other and are much larger than the amplitude of $u(t)$. Thus, during the steady swimming, the passive moment u_P generated by muscle contraction on one (e.g. dorsal) side of the body is mostly cancelled by the active moment u_A on the other (e.g. ventral) side to produce a small total moment $u := u_A - u_P$. If the body motion ϕ is perturbed, u_P deviates away from u_A and a large corrective input u can be generated.

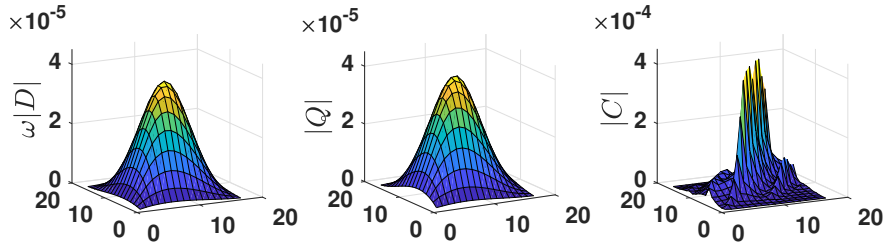

Figure 3.9: Magnitude of $\omega\mathcal{D}(j\omega)$, $Q(j\omega)$ and $C(j\omega)$

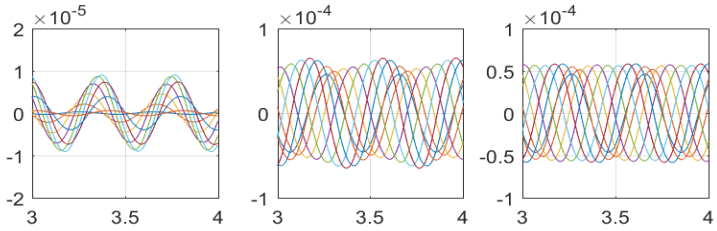

Figure 3.10: $u(t)$, $u_P(t)$, $u_A(t)$ in nominal swimming case

3.3 Closed-loop analysis as coupled oscillators

3.3.1 Effects of intersegmental coupling via neural and mechanical linkages

The closed-loop system of the leech swimming system, after quasi-linearization using the describing function at amplitude α, is given by

$$v = f(s)\Big(S + \epsilon\Delta(s)\Big)\boldsymbol{\kappa}(\alpha)v, \quad \Delta(s) := L(s) + B(s), \quad v(t) \in \mathbb{R}^{51}$$

$$L(s) := \begin{bmatrix} 0 & A_1(s) & A_2(s) & \cdots & A_5(s) & \cdots & 0 \\ D_1(s) & 0 & A_1(s) & \ddots & \ddots & \ddots & \vdots \\ D_2(s) & D_1(s) & 0 & \ddots & \ddots & \ddots & A_5(s) \\ \vdots & \ddots & \ddots & \ddots & \ddots & \ddots & \vdots \\ D_5(s) & \ddots & \ddots & \ddots & \ddots & \ddots & A_2(s) \\ \vdots & \ddots & \ddots & \ddots & \ddots & \ddots & A_1(s) \\ 0 & \cdots & D_5(s) & \cdots & D_2(s) & D_1(s) & 0 \end{bmatrix}, \; f_k(s) := \frac{g_k}{f(s)(1 + t_{d_k})s},$$

$$A_k(s) := f_k(s)\begin{bmatrix} 0 & -1 & 0 \\ 0 & 0 & -1 \\ 0 & 0 & 0 \end{bmatrix}, \quad D_k(s) := f_k(s)\begin{bmatrix} 2 & 0 & 0 \\ 0 & 0 & 0 \\ 0 & 0 & 0 \end{bmatrix}, \quad S_o = \begin{bmatrix} 0 & -1 & 0 \\ 0 & 0 & -1 \\ -1 & 0 & 0 \end{bmatrix},$$

$$t_{d_k} := \frac{1}{\omega_o}\tan(k\omega_o\tau_d), \quad g_k := \sqrt{1 + \omega_o^2 t_{d_k}^2}, \quad f(s) := \frac{\mu_\gamma}{1 + \tau_\gamma s}, \quad S := \mathrm{diag}(S_o, \ldots, S_o),$$

$$B := \frac{1}{\epsilon f(s)} B_{sg} P(s)\big(P(s) + K(s)\big)^{-1} N(s)\boldsymbol{\kappa}(\alpha)^{-1} = [B_{ij}(s)], \quad \alpha := \mathrm{col}(\alpha_1, \ldots, \alpha_{17}),$$

$$B_{sg} = \mathrm{diag}(\varsigma_1 b, \ldots, \varsigma_{17} b), \qquad b := \begin{bmatrix} 0 & 0 & 1 \end{bmatrix}^\top,$$
$$N(s) = \mathrm{diag}(n(s)c^\top, \ldots, n(s)c^\top), \quad c := \begin{bmatrix} 1 & 0 & 0 \end{bmatrix}^\top,$$

$$B_{ij}(s) := \begin{bmatrix} 0 & 0 & 0 \\ 0 & 0 & 0 \\ \chi_{ij}(s) & 0 & 0 \end{bmatrix}, \quad \chi_{ij}(s) := \frac{\varsigma_i n(s)}{\epsilon f(s) \cdot c^\top \boldsymbol{\kappa}(\alpha_i) c} \big[P(s)\big(P(s) + K(s)\big)^{-1}\big]_{ij}$$

where $f(s)S$ is block diagonal, representing the neural segmental oscillators, ϵ is the inter-segmental coupling strength, $\epsilon L(s)$ represents the intersegmental neuronal connections, and $\epsilon B(s)$ is the coupling of segments through the mechanical linkage. The segmental oscillator dynamics are given by $S_o \in \mathbb{R}^{3\times 3}$ and then S has S_o on the block diagonal, repeated $m = 17$ times. Partition $L(s)$ into $m \times m$ blocks, each of which is of dimension 3×3, and denote the (i, j) block by $L_{ij}(s)$. Use the same notation for $B(s)$ and define $B_{ij}(s)$ accordingly. Here we use $\omega_o = \frac{2\pi}{0.391\mathrm{s}} = 16.06$ rad/s, where 0.391 is the nominal swimming period in PNAS paper. Also, $\mu_\gamma = 3.6$ and $\tau_\gamma = 120$ ms.

Let $\ell, r \in \mathbb{C}^3$ be the left and right eigenvectors of S_o:

$$S_o r = \lambda_o r, \quad \ell^* S_o = \lambda_o \ell^*, \quad \ell^* r = 1,$$

where λ_o is the maximal eigenvalue. Then the solution of the MHB equation for each segment

$$\hat{v}_o = f(j\omega_o) S_o \boldsymbol{\kappa}(|\hat{v}_o|)\hat{v}_o, \quad \hat{v}_o \in \mathbb{C}^3$$

is given by

$$\hat{v}_o = \alpha_o r, \quad r = \ell = \frac{\sqrt{3}}{3} \begin{bmatrix} 1 \\ e^{-j(2/3)\pi} \\ e^{j(2/3)\pi} \end{bmatrix}, \quad f(j\omega_o)\boldsymbol{\kappa}(\alpha_o) = \frac{1}{\lambda_o}.$$

The solution of the MHB equation for the whole system

$$\hat{v} = f(j\omega_o)\Big(S + \epsilon\Delta(j\omega_o)\Big)\boldsymbol{\kappa}(|v|)\hat{v}, \quad \Delta(j\omega_o) := L(j\omega_o) + B(j\omega_o), \quad \hat{v} \in \mathbb{C}^{51},$$

may then be approximated by

$$(\lambda_o + \epsilon\mu)\hat{v} = \Big(S + \epsilon\Delta(j\omega_o)\Big)\hat{v}, \quad v = h \otimes \hat{v}_o, \quad h \in \mathbb{C}^{17}$$

because $\epsilon > 0$ is small, where $\epsilon\mu$ is the perturbation of the eigenvalue, and h is a vector to be determined so that $|h_i| \cong 1$, assuming uniform amplitudes. Noting that $\lambda_o \hat{v} = S\hat{v}$, we have

$$\mu\hat{v} = \Delta(j\omega_o)\hat{v}.$$

Then

$$\begin{aligned}
& \Lambda := \mathrm{diag}(\ell, \ldots, \ell), \quad \mathfrak{R} := \mathrm{diag}(r, \ldots, r), \\
\Rightarrow \quad & \mu\mathfrak{L}^*\hat{v} = \Lambda^*\Delta(j\omega_o)\hat{v}, \quad \hat{v} = \alpha_o\mathfrak{R}h \\
\Rightarrow \quad & \mu h = (\Lambda + \Xi)h, \quad \Lambda := \Lambda^* L(j\omega_o)\mathfrak{R}, \quad \Xi := \Lambda^* B(j\omega_o)\mathfrak{R}.
\end{aligned}$$

Thus, the intersegmental phases $\angle h$ can be estimated by the eigenvector h of $\Lambda+\Xi$ associated with the maximal eigenvalue μ. Slightly modified from the Chen 2008 paper,

$$\begin{aligned}
\Lambda_{ij} &= r_A e^{j\eta_{A_k}}, \quad r_A = (2/3)/|f(j\omega_o)|, \quad \eta_A = \pi/3, \quad (i < j) \\
\Lambda_{ij} &= r_D e^{j\eta_{D_k}}, \quad r_D = (2/3)/|f(j\omega_o)|, \quad \eta_D = 0, \qquad (i > j)
\end{aligned}$$

$$\begin{aligned}
\eta_{A_k} &:= \eta_A - \tan^{-1}(\omega_o t_{d_k}) - \angle f(j\omega_o), \\
\eta_{D_k} &:= \eta_D - \tan^{-1}(\omega_o t_{d_k}) - \angle f(j\omega_o),
\end{aligned}$$

where $\omega_o\tau_d \cong 13.8^o$ and $k := |i - j|$. Define

$$\Omega := \Lambda + \Xi = \Lambda^*\Delta\mathfrak{R},$$

$$r_{ij} := |\ell^* B_{ij}(j\omega_o)r| = |-\frac{1 + j\sqrt{3}}{6}\chi_{ij}(j\omega_o)| = \frac{1}{3}|\chi_{ij}(j\omega_o)|,$$

$$\eta_{ij} := \angle(\ell^* B_{ij}(j\omega_o)r) = \angle[-\frac{1 + j\sqrt{3}}{6}\chi_{ij}(j\omega_o)] = \angle[\chi_{ij}(j\omega_o)] - \frac{2}{3}\pi.$$

For each element $\Omega_{ij} := \Lambda_{ij} + \Xi_{ij}$ of Ω, we have

$$\Omega_{ij} = \begin{cases} r_A e^{j\eta_{A_k}} + r_{ij}e^{j\eta_{ij}} & (i < j) \\ r_{ij}e^{j\eta_{ij}} & (i = j) \\ r_D e^{j\eta_{D_k}} + r_{ij}e^{j\eta_{ij}} & (i > j) \end{cases} \tag{3.6}$$

To understand whether intersegmental neural dynamics or mechanical dynamics plays a dominant role, and how mechanical connection modifies the intersegmental phase lag from 180^o in the isolated CPG case to 360^o in the closed-loop CPG-plant case, we can plot the amplitude and phase of each element in Ω, with $\Omega := \Lambda$, $\Omega := \Xi$ and $\Omega := \Lambda + \Xi$ respectively.

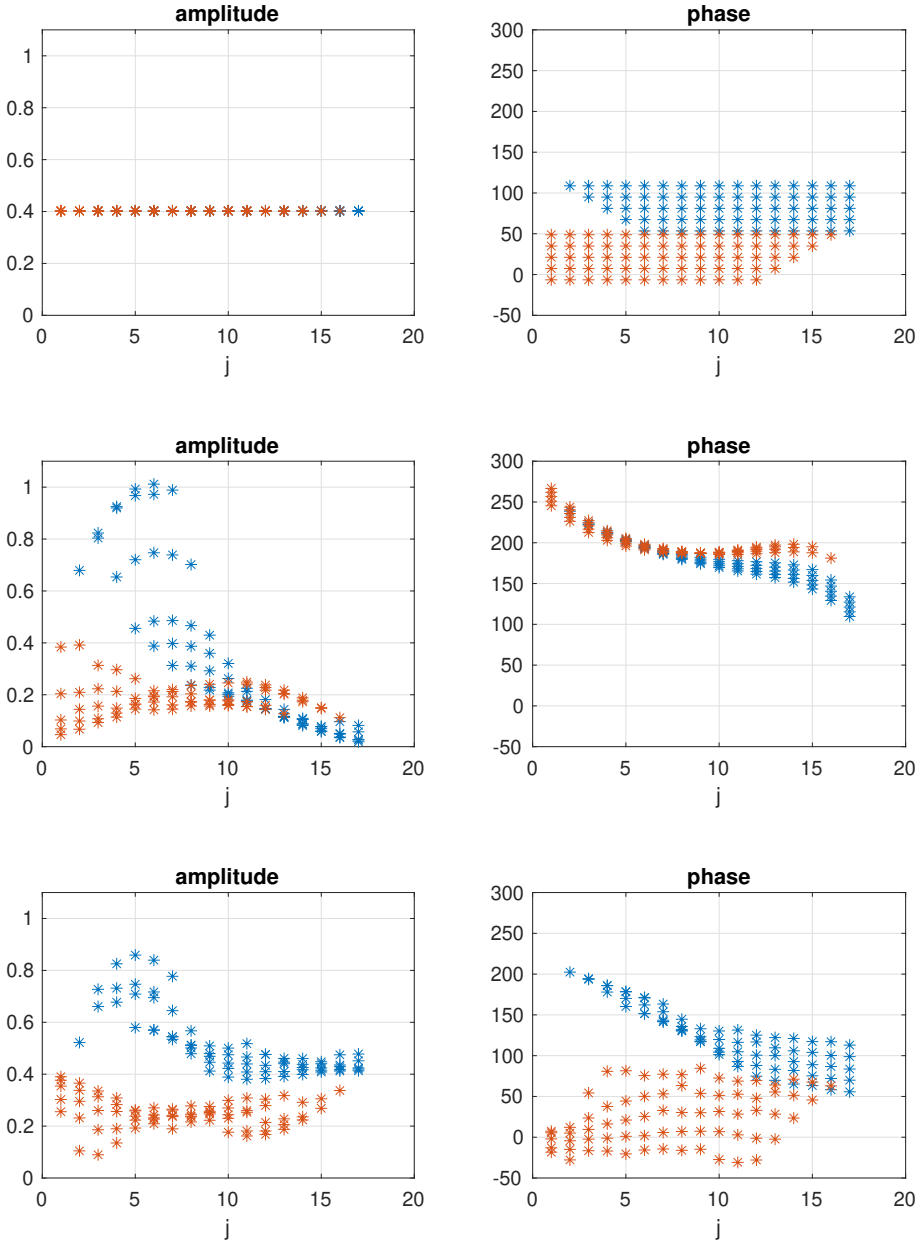

Figure 3.11: Amplitude and phase of Ω_{ij} with neural only(upper), mechanical only (middle), and both neural and mechanical linkage (lower), for $i < j$ (blue), $i > j$ (red)

In Fig. 3.11, the y-axis is the amplitude or phase in degree; x-axis represents the column index (j) Ω_{ij}. Blue denotes for ascending dynamics, red for descending dynamics. For amplitude, comparing top-left plot with bottom-left plot, and middle-left plot with bottom-left plot, the mechanical dynamics Ξ is the dominant force in amplitude modification, especially in the anterior part. This domination of mechanical dynamics over intersegmental neural dynamics in leech anterior part also shows in the phase plot, where when $j = 1$, the phase is increased to over 200^o in the bottom-right plot, comparing to the flat around 100^o in the top-right figure.

3.3.2 Analysis of intersegmental phase lag

To estimate the average phase lag per segment, let us consider the limiting case where the oscillator chain is infinitely long ($m = \infty$). In this case, a generic row i of the MHB equation $(\mu I - \Omega)h = 0$ takes the following form:

$$\sum_{k=1}^{5} \left[(\Omega_{i,i+k} h_{i+k} + \Omega_{i,i-k} h_{i-k} \right] = (\mu - \Omega_{ii}) h_i \tag{3.7}$$

Due to the uniformity of the intersegmental connections over the chain (that makes Δ a Toeplitz matrix), the eigenvector h has the structure such that h_{i+1}/h_i is constant over i. Consequently, the intersegmental phase lag is uniform over the chain, and we may let

$$h_i = re^{-j(i\eta_o)} \tag{3.8}$$

Substituting Eqn. (3.8) into Eqn. (3.7) and solving for the maximal eigenvalue μ, we have

$$\begin{aligned} \mu e^{-j(i\eta_o)} = & \sum_{k=1}^{5} \Big[r_A e^{j(\eta_{A_k} - (i+k)\eta_o)} + r_{i,i+k} e^{j(\eta_{i,i+k} - (i+k)\eta_o)} \\ & + r_D e^{j(\eta_{D_k} - (i-k)\eta_o)} + r_{i,i-k} e^{j(\eta_{i,i-k} - (i-k)\eta_o)} \Big] + r_{ii} e^{j(\eta_{ii} - i\eta_o)} \end{aligned}$$

$$\therefore \mu = \sum_{k=1}^{5} \left[r_A e^{j(\eta_{A_k} - k\eta_o)} + r_{i,i+k} e^{j(\eta_{i,i+k} - k\eta_o)} + r_D e^{j(\eta_{D_k} + k\eta_o)} + r_{i,i-k} e^{j(\eta_{i,i-k} + k\eta_o)} \right] + r_{ii} e^{j\eta_{ii}} \tag{3.9}$$

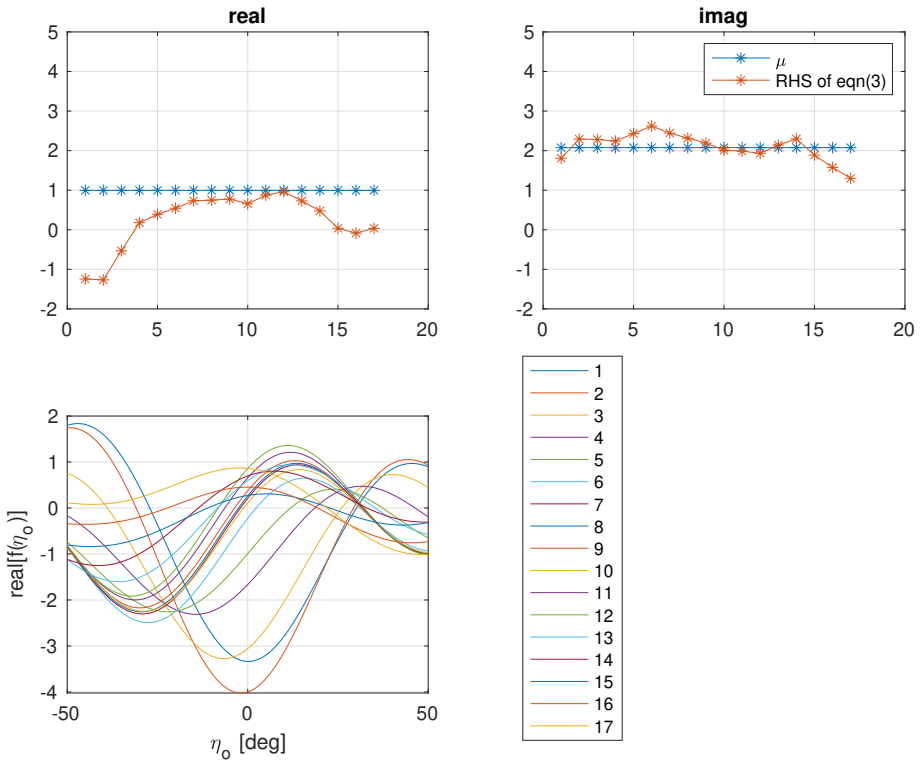

Figure 3.12: The maximal eigenvalue μ of Ω (blue lines, top row). The right hand side of (3.9) for each of $i = 1, \ldots, 17$ with the edge effect (red curves, top row). The real part of the right hand side of (3.9) for each i (bottom row)

This is a parametrization of the set of infinitely many eigenvalues of the infinite matrix Ω in terms of $\eta_o \in \mathbb{R}$. The profile of a stable oscillation can be estimated from the maximal eigenvalue, and hence, we are interested in finding η_o such that $f(\eta_o) := \Re[\mu]$ takes its maximum value. Taking the derivative of μ w.r.t η_o, dropping the imaginary part and setting it to zero, we have

$$\Re\left(\frac{\partial\mu}{\partial\eta_o}\right) = \sum_{k=1}^{5} k\Big[r_A\sin(\eta_{A_k}-k\eta_o) + r_{i,i+k}\sin(\eta_{i,i+k}-k\eta_o)$$
$$- r_D\sin(\eta_{D_k}+k\eta_o) - r_{i,i-k}\sin(\eta_{i,i-k}+k\eta_o)\Big]$$
$$\cong \sum_{k=1}^{5} k\Big[r_A\eta_{A_k} + r_{i,i+k}\eta_{i,i+k} - r_D\eta_{D_k} - r_{i,i-k}\eta_{i,i-k}\Big]$$
$$- \Big[\sum_{k=1}^{5} k^2(r_A + r_D + r_{i,i+k} + r_{i,i-k})\Big]\eta_o$$

$$\therefore \eta_o = \sum_{k=1}^{5} k\Big[r_A\eta_{A_k} + r_{i,i+k}\eta_{i,i+k} - r_D\eta_{D_k} - r_{i,i-k}\eta_{i,i-k}\Big] \Big/ \sum_{k=1}^{5} k^2(r_A + r_D + r_{i,i+k} + r_{i,i-k}) \tag{3.10}$$

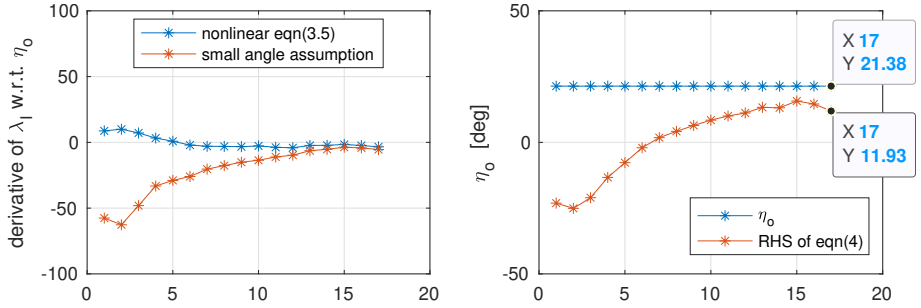

Figure 3.13: The exact and approximation of $\Re\left(\frac{\partial\mu}{\partial\eta_o}\right)$; η_o and right hand side of eqn(3.10)

We see there is a deviation in the result from small angle approximation (red) to the actual value of η_o (blue) in the above figures. This gap comes from the inaccuracy of the approximation of $\sin(\eta_{A_k} - k\eta_o)$ by $\eta_{A_k} - k\eta_o$. Therefore the following change was made to reduce the inaccuracy from this approximation.

For each element Ω_{ij} of Ω, use the polar coordinates

$$\Omega_{ij} = \rho_{ij}e^{j\phi_{ij}}.$$

This is due to the reason that the approximation

$$\Omega_{ij} = r_A e^{j\eta_{A_k}} + r_{ij}e^{j\eta_{ij}} = \rho_{ij}e^{j\phi_{ij}} \quad \Rightarrow \quad r_A\eta_{A_k} + r_{ij}\eta_{ij} \cong \rho_{ij}\phi_{ij}$$

which exists between the two formulations would be accurate if η_{A_k} and η_{ij} are small.

Substituting eqn (3.8) into eqn (3.7) and solving for μ, we have

$$\mu = \sum_{k=1}^{5} \left[\Omega_{i,i+k} e^{-jk\eta_o} + \Omega_{i,i-k} e^{jk\eta_o} + \Omega_{ii}\right] \tag{3.11}$$

Taking the derivative with respect to η_o,

$$\begin{aligned} \Re\left(\frac{\partial \mu}{\partial \eta_o}\right) &= \sum_{k=1}^{5} k\left[\rho_{i,i+k}\sin(\phi_{i,i+k} - k\eta_o) - \rho_{i,i-k}\sin(\phi_{i,i-k} + k\eta_o)\right] \\ &\cong \sum_{k=1}^{5} k\left[\rho_{i,i+k}(\phi_{i,i+k} - k\eta_o) - \rho_{i,i-k}(\phi_{i,i-k} + k\eta_o)\right] \end{aligned}$$

Setting the derivative to zero and solving for η_o,

$$\eta_o = \sum_{k=1}^{5} k(\rho_{i,i+k}\phi_{i,i+k} - \rho_{i,i-k}\phi_{i,i-k}) \Big/ \sum_{k=1}^{5} k^2(\rho_{i,i+k} + \rho_{i,i-k}). \tag{3.12}$$

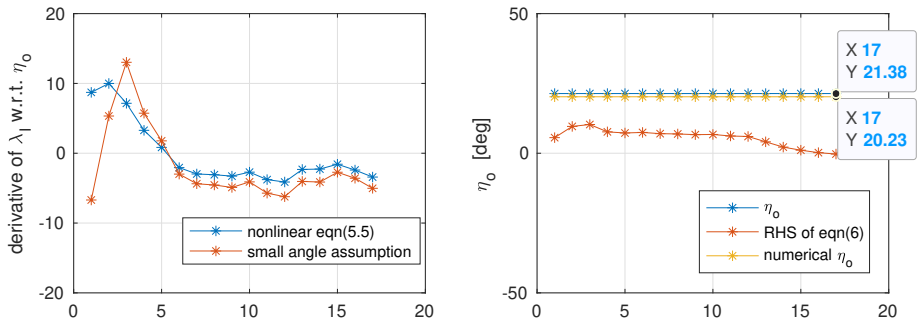

Figure 3.14: The exact and approximation of $\Re\left(\frac{\partial \mu}{\partial \eta_o}\right)$; η_o, right hand side of eqn(3.12), $\sum_i^{17} \Re\left(\frac{\partial \mu}{\partial \eta_o}\right)$

Comparing with the red curve in the right plot in Fig. 3.13, the approximation of the average phase lag per segment (red curve) in the right figure in Fig. 3.14 is a lot closer to the actual η_o (blue curve).

General formulation

The formula developed above is a special case of the following where the interactions are between nearest 6 neighbors. The eigenvalue/eigenvector equation is

$$\Omega h = \mu h, \quad h_\ell = r_\ell e^{-j\ell\eta_o} \quad \Leftrightarrow \quad \sum_\ell \Omega_{i\ell} r_\ell e^{-j\ell\eta_o} = \mu r_i e^{-ji\eta_o}.$$

Denoting $\Omega_{i\ell} := \rho_{i\ell} e^{j\phi_{i\ell}}$ and solving for μ, we have

$$\mu = \sum_\ell \Omega_{i\ell}(r_\ell/r_i) e^{-j\ell\eta_o} e^{ji\eta_o} = \sum_\ell \rho_{i\ell}(r_\ell/r_i) e^{j(\phi_{i\ell}+(i-\ell)\eta_o)}.$$

Taking the derivative with respect to η_o,

$$\begin{aligned} \Re\left(\frac{\partial \mu}{\partial \eta_o}\right) &= \sum_\ell (\ell - i)\rho_{i\ell}(r_\ell/r_i)\sin(\phi_{i\ell} + (i-\ell)\eta_o) \\ &\cong \sum_\ell (\ell - i)\rho_{i\ell}(r_\ell/r_i)(\phi_{i\ell} + (i-\ell)\eta_o). \end{aligned}$$

Setting the derivative to zero and solving for η_o,

$$\eta_o \cong \sum_\ell (\ell - i)\rho_{i\ell} r_\ell \phi_{i\ell} \Big/ \sum_\ell (\ell - i)^2 \rho_{i\ell} r_\ell.$$

Maybe a sensitivity analysis gives some insight. Setting the derivative to zero and takeing the partial derivatives with respect to ρ_{ij} and ϕ_{ij},

$$(j-i)\sin(\phi_{ij} + (i-j)\eta_o) + (j-i)\rho_{ij}(i-j)\cos(\phi_{ij} + (i-j)\eta_o)\frac{\partial \eta_o}{\partial \rho_{ij}} = 0,$$

$$(j-i)\rho_{ij}\cos(\phi_{ij} + (i-j)\eta_o)\Big(1 + (i-j)\frac{\partial \eta_o}{\partial \phi_{ij}}\Big) = 0,$$

$$\Rightarrow \quad \frac{\partial \eta_o}{\partial \rho_{ij}} = \frac{\tan(\phi_{ij} + (i-j)\eta_o)}{(j-i)\rho_{ij}}, \quad \frac{\partial \eta_o}{\partial \phi_{ij}} = \frac{1}{j-i}.$$

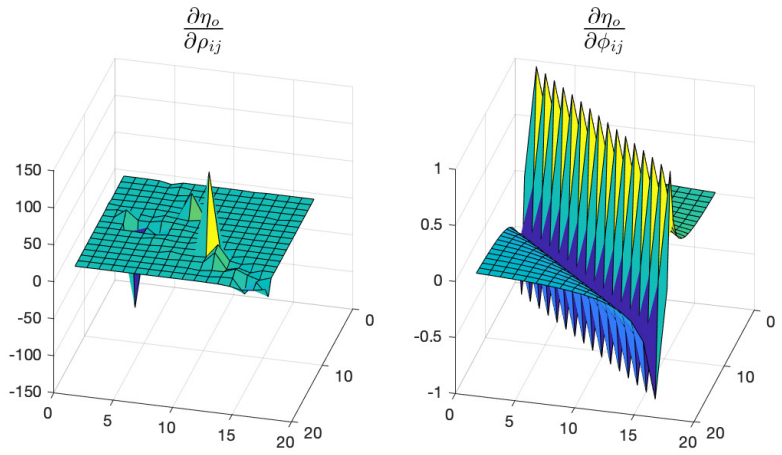

Figure 3.15: Surf plot of $\frac{\partial \eta_o}{\partial \rho_{ij}}$ and $\frac{\partial \eta_o}{\partial \phi_{ij}}$

Similarly, if we use the following to represent each element in Ω, we could solve for $\frac{\partial \eta_o}{\partial r_{ij}}$ and $\frac{\partial \eta_o}{\partial \eta_{ij}}$.

$$\Omega_{i\ell} = \begin{cases} r_A e^{j\eta_{A_k}} + r_{i\ell} e^{j\eta_{i\ell}} & (i < \ell) \\ r_{i\ell} e^{j\eta_{i\ell}} & (i = \ell) \\ r_D e^{j\eta_{D_k}} + r_{i\ell} e^{j\eta_{i\ell}} & (i > \ell) \end{cases}$$

Using the same eigenvalue/eigenvector equation,

$$\mu = \sum_\ell \Omega_{i\ell}(r_\ell / r_i) e^{-j\ell\eta_o} e^{ji\eta_o} = \begin{cases} \sum_\ell (r_\ell / r_i)(r_A e^{j\eta_{A_k}} + r_{i\ell} e^{j\eta_{i\ell}}) e^{j(i-\ell)\eta_o} & (i < \ell) \\ \sum_\ell r_{i\ell}(r_\ell / r_i) e^{j\eta_{i\ell}} & (i = \ell) \\ \sum_\ell (r_\ell / r_i)(r_D e^{j\eta_{D_k}} + r_{i\ell} e^{j\eta_{i\ell}}) e^{j(i-\ell)\eta_o} & (i > \ell) \end{cases}$$

$$\Re\left(\frac{\partial \mu}{\partial \eta_o}\right) = \begin{cases} \sum_\ell (\ell - i)(r_\ell / r_i)\Big(r_A \sin(\eta_{A_k} + (i-\ell)\eta_o) + r_{i\ell} \sin(\eta_{i\ell} + (i-\ell)\eta_o)\Big) & (i < \ell) \\ \sum_\ell (\ell - i)(r_\ell / r_i)\Big(r_D \sin(\eta_{D_k} + (i-\ell)\eta_o) + r_{i\ell} \sin(\eta_{i\ell} + (i-\ell)\eta_o)\Big) & (i > \ell) \end{cases}$$

and taking the partial derivatives with respect to r_{ij} and η_{ij} and using $k = |i - j|$,

$$\frac{\partial \eta_o}{\partial r_{ij}} = \begin{cases} \frac{\sin\left(\eta_{ij} - k\eta_o\right)}{k\left[r_A \cos(\eta_{A_k} - k\eta_o) + r_{ij}\cos(\eta_{ij} - k\eta_o)\right]} & (i < j) \\ \frac{\sin\left(\eta_{ij} + k\eta_o\right)}{-k\left[r_D \cos(\eta_{D_k} + k\eta_o) + r_{ij}\cos(\eta_{ij} + k\eta_o)\right]} & (i > j) \end{cases}$$

$$\frac{\partial \eta_o}{\partial \eta_{ij}} = \begin{cases} \dfrac{r_{ij}\cos\left(\eta_{ij} - k\eta_o\right)}{k\left[r_A\cos(\eta_{A_k} - k\eta_o) + r_{ij}\cos(\eta_{ij} - k\eta_o)\right]} & (i < j) \\ \dfrac{r_{ij}\cos\left(\eta_{ij} + k\eta_o\right)}{-k\left[r_D\cos(\eta_{D_k} + k\eta_o) + r_{ij}\cos(\eta_{ij} + k\eta_o)\right]} & (i > j) \end{cases}$$

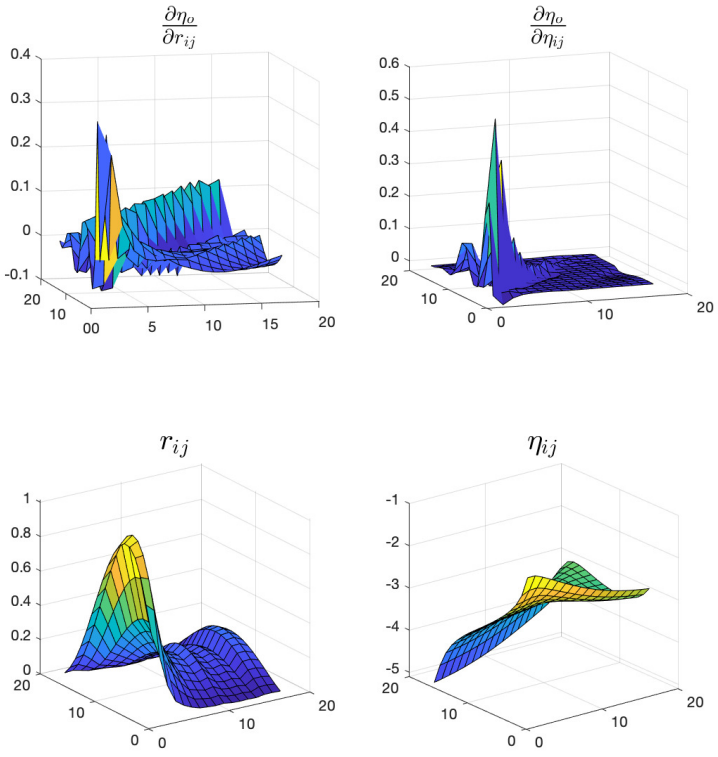

General formulation using polar coordinate

In the CPG model

$$v = f(s)M\varphi(v), \tag{3.13}$$

the MHB equation, assuming uniform amplitude, is given by

$$\lambda\hat{v} = M\hat{v}, \quad \lambda := \frac{1}{f(j\omega)\kappa(\alpha)} = \frac{1 + j\omega\tau}{\kappa(\alpha)}.$$

The "standard" analysis stated that the maximal eigenvalue of M is the one that gives a good estimate of the oscillation profile. The maximal eigenvalue is defined to be the one with the greatest (most positive) real part. Looking at the formula for λ above, this is equivalent

to the smallest $\kappa(\alpha)$, of the largest amplitude α. So, another way to write the MHB equation is

$$\sigma\hat{v} = f(j\omega)M\hat{v}, \quad \sigma := \frac{1}{\kappa(\alpha)},$$

where σ is the maximal eigenvalue of $f(j\omega)M$. This rewriting is not very useful for the analysis of (3.13), but is useful for the analysis of the weakly coupled segmental oscillators, or

$$v = f(s)\Big(S + \epsilon\Delta(s)\Big)\boldsymbol{\kappa}(\alpha)v, \quad \Delta(s) := L(s) + B(s), \quad v(t) \in \mathbb{R}^{51}$$

Let us rewrite this as

$$v = \Big(f(s)S + \epsilon\nabla(s)\Big)\boldsymbol{\kappa}(\alpha)v, \quad \nabla(s) := f(s)\Delta(s),$$

The MHB equation is

$$\lambda\hat{v} = \Big(f(j\omega)S + \epsilon\nabla(j\omega)\Big)\hat{v}, \quad \lambda := \frac{1}{\kappa(\alpha)}.$$

We follow the previous analysis. Let $\ell, r \in \mathbb{C}^3$ be the left and right eigenvectors of S_o:

$$S_o r = \lambda_o r, \quad \ell^* S_o = \lambda_o \ell^*, \quad \ell^* r = 1,$$

where λ_o is the maximal eigenvalue. Then the MHB equation for each segment is

$$\sigma_o\hat{v}_o = f(j\omega_o)S_o\hat{v}_o, \quad \sigma_o = \frac{1}{\kappa(\alpha_o)} = \lambda_o f(j\omega_o), \quad \hat{v}_o = \alpha_o r$$

where λ_o specifies ω_o, α_o, and σ_o. The MHB equation for the whole system may be approximately given by

$$(\sigma_o + \epsilon\gamma)\hat{v} = \Big(f(j\omega_o)S + \epsilon\nabla(j\omega_o)\Big)\hat{v}, \quad \hat{v} = h \otimes \hat{v}_o, \quad h \in \mathbb{C}^{17}$$

because $\epsilon > 0$ is small, where $\epsilon\mu$ is the perturbation of the eigenvalue, and h is a vector to be determined so that $|h_i| \cong 1$, assuming uniform amplitudes. Noting that $\sigma_o\hat{v} = f(j\omega_o)S\hat{v}$, we have

$$\gamma\hat{v} = \nabla(j\omega_o)\hat{v},$$

Using the left and right eigenvectors,

$$\gamma h = \Lambda \nabla(j\omega_o) \Re h.$$

Assume linear phase lag

$$h_m = e^{-jm\eta_o},$$

the MHB condition becomes

$$\gamma = \sum_n \rho_{mn} e^{j(\theta_{mn}+(m-n)\eta_o)}, \quad \rho_{mn} e^{j\theta_{mn}} := \ell^* \nabla_{mn}(j\omega_o) r,$$

where $\nabla_{mn}(j\omega_o)$ is the (m,n) block of $\nabla(j\omega_o)$. Consider the case where there is no mechanical linkage (i.e. $B(s) = 0$). Note that, when $k := n - m > 0$,

$$\theta_{mn} = \eta_A - \tan^{-1}(\omega_o t_{d_k}) = \pi/3 - k\omega_o \tau_d =: \eta_{A_k}, \quad (k := n - m > 0),$$

$$\theta_{mn} = \eta_D - \tan^{-1}(\omega_o t_{d_k}) = -k\omega_o \tau_d =: \eta_{D_k}, \quad (k := m - n > 0).$$

$$r_A = r_D := 2/3$$

This approach is exactly the same as before except that the effect of $f(j\omega_o)$ is now included in γ. This formulation is actually the same as the Chen 2008 paper, and may give a more accurate estimate of the phase lag even after the approximation $\sin(x) \cong x$.

Also, this formulation may be useful to give an estimate of the effect of each connection on the intersegmental phase lag. The real part of the eigenvalue is

$$\Re[\gamma] = \sum_n \rho_{mn} \cos(\theta_{mn} + (m-n)\eta_o).$$

If the (m,n) block were the only intersegmental connection, then the real part of γ is maximized when

$$\theta_{mn} + (m-n)\eta_o = 0 \quad \Rightarrow \quad \eta_o = \theta_{mn}/(n-m) = \begin{cases} \pi/(3k) - \omega_o \tau_d, & k := n - m > 0, \\ \omega_o \tau_d, & k := m - n > 0. \end{cases}$$

A rough value of the delay effect is

$$\omega_o = 6\pi, \quad \tau_d = 0.015, \quad \omega_o\tau_d \cong 16^o.$$

Hence a descending connection ($m > n$) contribute to making the intersegmental phase lag $\eta_o = 16^o$. An ascending connection ($n > m$) gives $\eta_o = 60^o/k - 16^o$, which adds up to $\eta_o = 11.4^o$ on average for the 5 segment span $m = n-5, n-4, \ldots, n-1$. These numbers seem reasonable.

If the (m, n) block were the only intersegmental connection,

$$\theta_{mn} = \angle[X_{mn}(j\omega_o)] - \frac{2}{3}\pi := \angle\Big[\frac{\varsigma_i n(j\omega_o)}{\epsilon c^\top \mathcal{K}(\alpha_i)c}\big[P(j\omega_o)\big(P(j\omega_o) + K(j\omega_o)\big)^{-1}\big]_{mn}\Big] - \frac{2}{3}\pi =: \eta_{mn}$$

$$\rho_{mn} = |-\frac{1+j\sqrt{3}}{6}X_{mn}(j\omega_o)| = \frac{1}{3}|X_{mn}(j\omega_o)| =: r_{mn}$$

therefore, overall we have

$$\Omega_{mn} = \begin{cases} r_A e^{j\eta_{A_k}} + r_{mn}e^{j\eta_{mn}} & (m < n) \\ r_{mn}e^{j\eta_{mn}} & (m = n) \\ r_D e^{j\eta_{D_k}} + r_{mn}e^{j\eta_{mn}} & (m > n) \end{cases}$$

$$\gamma = \sum_{k=1}^{17}\big[\Omega_{m,i+k}e^{-jk\eta_o} + \Omega_{m,m-k}e^{jk\eta_o} + \Omega_{mm}\big] \tag{3.14}$$

Taking the derivative with respect to η_o,

$$\Re\left(\frac{\partial\gamma}{\partial\eta_o}\right) = \sum_{k=1}^{17} k\big[\rho_{m,m+k}\sin(\theta_{m,m+k} - k\eta_o) - \rho_{m,m-k}\sin(\theta_{m,m-k} + k\eta_o)\big] \tag{3.15}$$

$$\cong \sum_{k=1}^{17} k\big[\rho_{m,m+k}(\theta_{m,m+k} - k\eta_o) - \rho_{m,m-k}(\theta_{m,m-k} + k\eta_o)\big] \tag{3.16}$$

Setting the derivative to zero and solving for η_o,

$$\eta_o = \sum_{k=1}^{17} k(\rho_{m,m+k}\theta_{m,m+k} - \rho_{m,m-k}\theta_{m,m-k})\Big/\sum_{k=1}^{17} k^2(\rho_{m,m+k} + \rho_{m,m-k}). \tag{3.17}$$

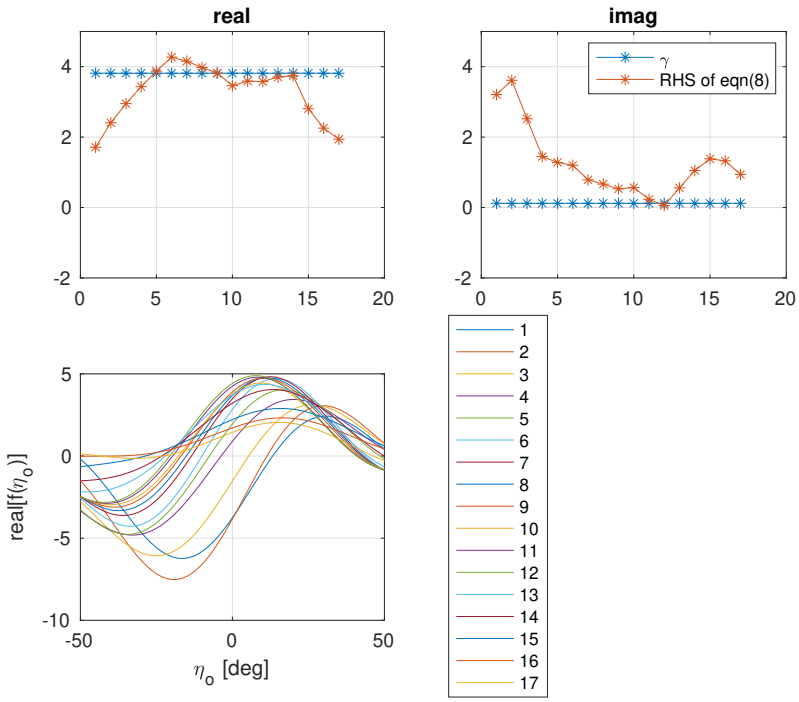

Figure 3.16: The maximal eigenvalue μ of Ω (blue lines). The right hand side of (3.14) for each of $i = 1, \ldots, 17$ with the edge effect (red curves).

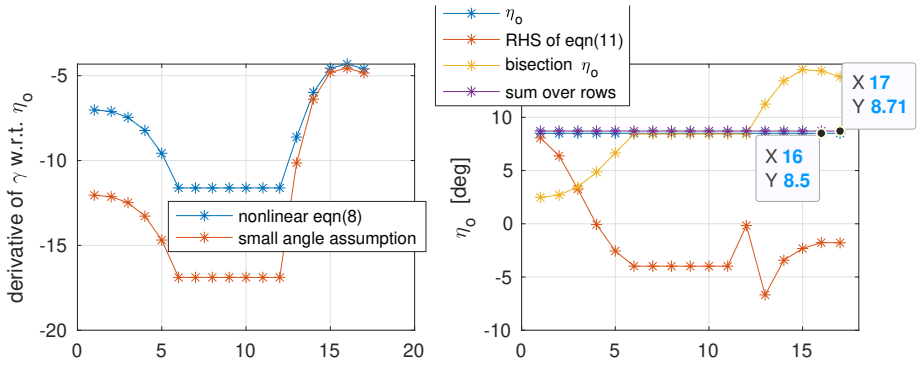

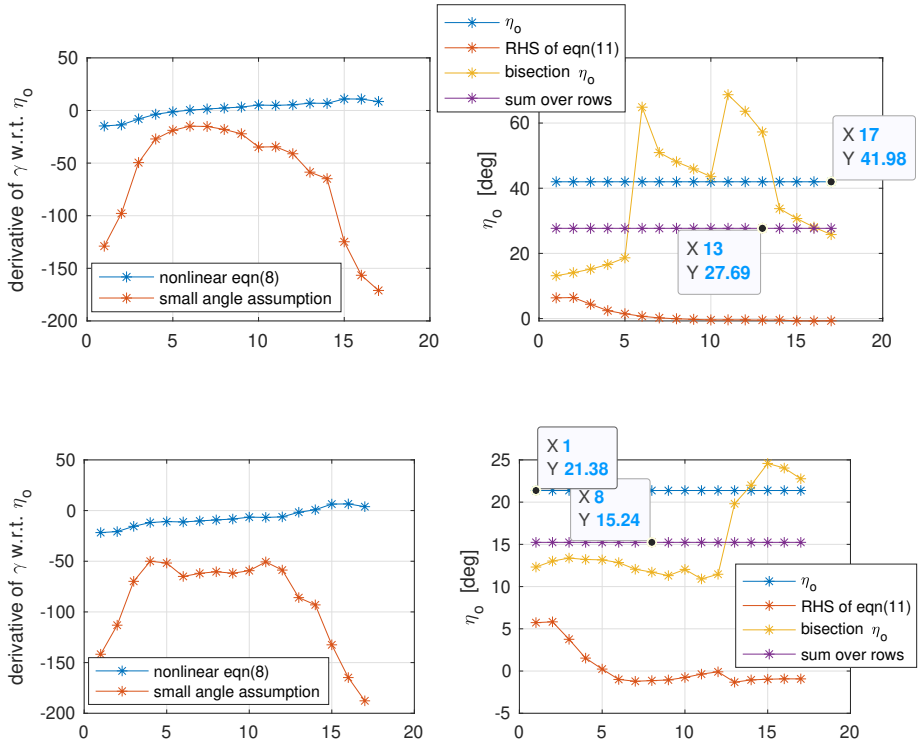

Figure 3.17: The exact and approximation of $\Re\left(\frac{\partial\gamma}{\partial\eta_o}\right)$; η_o from simulation (blue), right hand side of eqn(3.12) (red), numerical result of η_o using bisecion (yellow), $\sum_m^{17}\Re\left(\frac{\partial\gamma}{\partial\eta_o}\right)$ (purple)

Comparing with the red curve in the right plot in Fig. 3.13, the approximation of the average phase lag per segment (purple curve) in the bottom-right figure in Fig. 3.17 is a lot closer to the actual η_o (blue curve).

$$\frac{\partial\eta_o}{\partial\rho_{mn}} = \frac{\tan(\theta_{mn}+(m-n)\eta_o)}{(n-m)\rho_{mn}}, \quad \frac{\partial\eta_o}{\partial\theta_{mn}} = \frac{1}{n-m}.$$

$$\frac{\partial\eta_o}{\partial r_{mn}} = \begin{cases} \dfrac{\sin\left(\eta_{mn}-k\eta_o\right)}{k\left[r_A\cos(\eta_{A_k}-k\eta_o)+r_{mn}\cos(\eta_{mn}-k\eta_o)\right]} & (m<n) \\ \dfrac{\sin\left(\eta_{mn}+k\eta_o\right)}{-k\left[r_D\cos(\eta_{D_k}+k\eta_o)+r_{mn}\cos(\eta_{mn}+k\eta_o)\right]} & (m>n) \end{cases}$$

$$\frac{\partial \eta_o}{\partial \eta_{mn}} = \begin{cases} \dfrac{r_{mn}\cos\left(\eta_{mn}-k\eta_o\right)}{k\left[r_A\cos(\eta_{A_k}-k\eta_o)+r_{mn}\cos(\eta_{mn}-k\eta_o)\right]} & (m<n) \\ \dfrac{r_{mn}\cos\left(\eta_{mn}+k\eta_o\right)}{-k\left[r_D\cos(\eta_{D_k}+k\eta_o)+r_{mn}\cos(\eta_{mn}+k\eta_o)\right]} & (m>n) \end{cases}$$

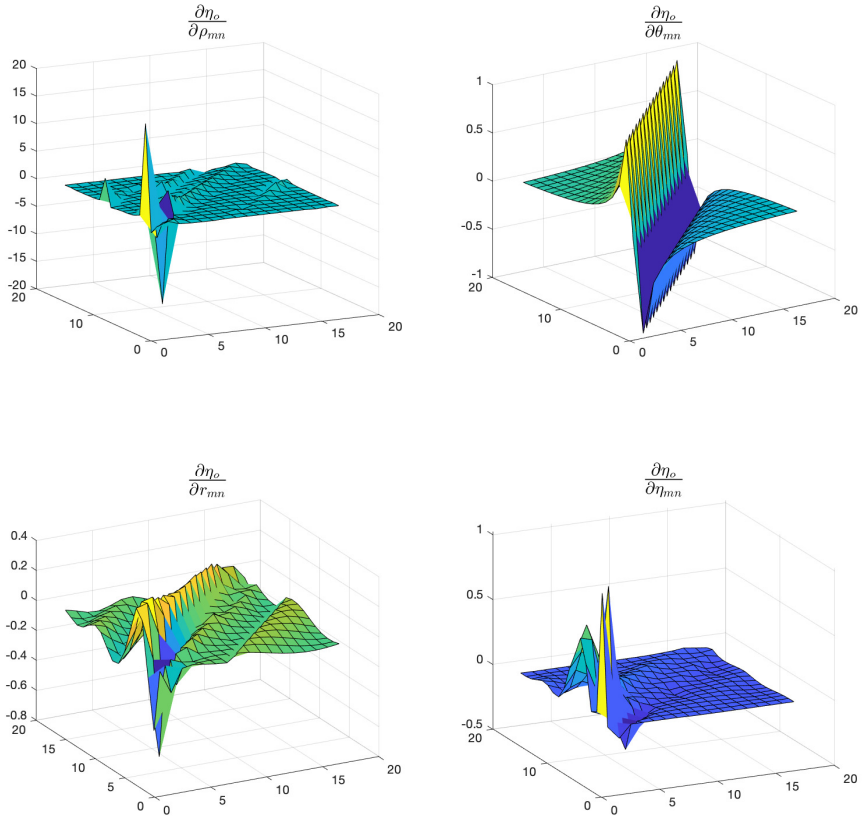

CHAPTER 4

Control mechanisms underlying leech swimming

In this chapter, we will discuss about the control mechanism for leech swimming. Using the MHB method in the previous chapter, three control mechanism are proposed in the first section. To better understand the internal reference generator and weak coupling stabilization, we will decompose the CPG and discuss using eigenstructure theory. Finally, generalized CPG design guidelines are given on CPG controller design for robotic systems to achieve target oscillation with stability.

4.1 Internal architecture of CPG

We proposed two control architectures shown in Fig. 4.1a and Fig. 4.1b. The idea behind the first one is that part of the CPG consists of a conservative oscillator ("CPG" in Fig. 4.1a) and a damping compensator ("$D(s)$" box between $\hat{\phi}$ and $\hat{u}$). For the mechanical plant side, we separate the body-fluid module into "ideal body-fluid" part, which is a conservative plant, and the dissipative part. The$K(s)$ on the plant side denotes the stiffness dynamics of the plant. For the second one in Fig. 4.1b, we think there is a symmetry structure between controller and plant through weak coupling in the closed-loop system (signal $w \cong 0$ in the steady states). Part of the CPG functions as a reference generator or internal model, generating signal $\hat{u}$ similar to the torque u fed into the plant. Why would we want to do the decomposition? What's the difference between the original and the decomposed CPG? The difference is that the decomposed is an exact internal model. Without any input, the decomposed CPG can generate v with 360^o phase lag, same as the ϕ from the plant, while

the original CPG generates v with 180^o phase lag without input.

In this section, we would want to find out the dynamics inside CPG that acts like this reference generator, by using LMI technique, then verify this decomposition by simulation in three conditions.

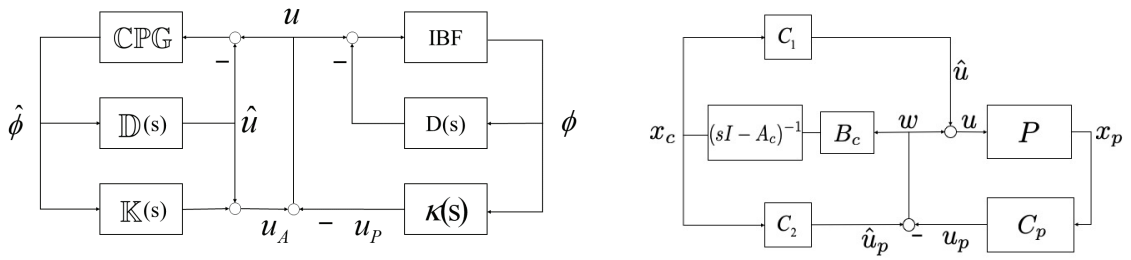

(a) Damping compensation architecture (b) Eigenstructure architecture

Figure 4.1: Proposed architectures

The CPG has been modeled as

$$v = M(s)\varphi(v) + Bu.$$

We decompose the CPG into the two components

$$v = \Big(M(s) + BD(s)\Big)\varphi(v) + B(u - \tilde{u}), \quad \tilde{u} := D(s)\varphi(v), \tag{4.1}$$

as shown in Fig. 4.1a (the use of $\hat{u}$ is avoided to reserve the hat notation for phasors). The task is to determine $D(s)$ so that

- $\tilde{u} = D(s)\varphi(v)$ generates the muscle bending moment $\tilde{u} = u$ from the membrane potentials, as observed during intact swimming
- the internal CPG model $v = \Big(M(s) + BD(s)\Big)\varphi(v)$ has the observed membrane potential oscillations as a stable limit cycle.

We assume that the bending moment of the i^{th} segment, w_i, is generated by the membrane potentials of the i^{th} segmental oscillator with the intrasegmental synaptic dynamics:

$$D(s) = f(s)\chi, \quad \chi := \text{diag}(\chi_1, \ldots, \chi_{17}) \in \mathbb{R}^{17\times 51}, \quad \chi_i \in \mathbb{R}^{1\times 3}, \quad f(s) := \frac{\mu_\gamma}{1+\tau_\gamma s}. \tag{4.2}$$

Using phasor and describing function to approximate periodic signal v and the nonlinear function $\varphi(v)$,

$$\varphi(v) \cong \boldsymbol{\kappa}(\alpha_i)v, \quad v_i \cong \alpha_i \sin(\omega t + \beta_i), \quad \hat{v}_i = \alpha_i e^{j\beta_i}$$

the first constraint on $D(s)$ is expressed as

$$f(j\omega)\chi\boldsymbol{\kappa}(\alpha)\hat{v} = \hat{u} \tag{4.3}$$

where $(\hat{u}, \hat{v})$ are the phasors of the harmonic approximations of (u, v) during intact swimming, obtained by closed-loop simulation of the integrated model, $\alpha := |\hat{v}| \in \mathbb{R}^{17}$ are the amplitudes of v, and $\boldsymbol{\kappa}(\alpha) \in \mathbb{R}^{17\times 17}$ is the diagonal matrix of the describing functions. Similarly, the internal CPG model is constrained by the MHB condition:

$$\hat{v} = (M(j\omega) + f(j\omega)B\chi)\boldsymbol{\kappa}(\alpha)\hat{v} \tag{4.4}$$

For orbital stability of the oscillation $v(t) \cong \Re[\hat{v}e^{j\omega t}]$, we require the characteristic equation

$$\det[I - (M(j\omega) + BD(j\omega))\boldsymbol{\kappa}(\alpha)] = 0$$

to have all the roots s except $\pm j\omega$ satisfy $\Re[s] < 0$. This condition is equivalent to the marginal stability condition on quasi-liner system:

$$\hat{v} = (M(j\omega) + BD(j\omega))\boldsymbol{\kappa}(\alpha)\hat{v}.$$

4.1.1 Three ways of state-space realizations

To further analyze the stability of the system, we shall represent the CPG in state-space realization. By observing the internal, conservative CPG model

$$v = \Big(M(s) + BD(s)\Big)\varphi(v) \tag{4.5}$$

there are multiple ways to represent Eqn.(4.5) in state-space. We will list all three ways here.

4.1.1.1 Realizations from transfer functions

The first method is to partition the internal CPG model described by transfer function in Eqn.(4.5):

$$\begin{aligned} v &= \Big(M(s) + Bf(s)\chi\Big)\varphi(v) \\ &= \underbrace{\begin{bmatrix} M(s) & Bf(s) \end{bmatrix}}_{ss(\mathbb{A},\mathbb{B},\mathbb{C},0)} \begin{bmatrix} \varphi(v) \\ \chi\varphi(v) \end{bmatrix} \end{aligned}$$

After partitioning $\mathbb{B}$ into $\begin{bmatrix} \mathbb{B}_1 & \mathbb{B}_2 \end{bmatrix}$ according to the dimension of $\varphi(v)$ and $\chi\varphi(v)$, and approximating $\varphi(v)$ by $\boldsymbol{\kappa}(\alpha)v$, the system could be described as

$$\begin{cases} \dot{x} = \mathbb{A}\chi + (\mathbb{B}_1 + \mathbb{B}_2\chi)\boldsymbol{\kappa}(\alpha)v \\ v = \mathbb{C}x \end{cases}$$

$$\Rightarrow \dot{x} = \Big[\mathbb{A} + (\mathbb{B}_1 + \mathbb{B}_2\chi)\boldsymbol{\kappa}(\alpha)\mathbb{C}\Big]x.$$

4.1.1.2 Realizations from for-loop

Looking at the original CPG neuronal circuits Eqn.(2.4), we can define different state-space $\mathcal{A}$ and $\mathcal{B}$ matrices w.r.t. intrasegmental or intersegmental dynamics.

For intrasegmental dynamics,

$$x_{ki} = \frac{\mu_\gamma}{1 + \tau_\gamma s}\boldsymbol{\kappa}(\alpha_i)v_i \qquad \text{where } k = 6, i = 1, .., 17, x_{ki} \in \mathbb{R}^3$$

$$\therefore \dot{x}_{ki} = (\frac{-1}{\tau_\gamma} I)x_{ki} + (\frac{\mu_\gamma}{\tau_\gamma} I)\boldsymbol{\kappa}(\alpha_i)v_i$$

For intersegmental dynamics,

$$x_{ki} = \frac{1}{1 + k\tau_d s}\boldsymbol{\kappa}(\alpha_i)v_i \qquad \text{where } k = 1, ..., 5, i = 1, .., 17, x_{ki} \in \mathbb{R}^3$$

$$\therefore \dot{x}_{ki} = (\frac{-1}{k\tau_d} I)x_{ki} + (\frac{1}{k\tau_d} I)\boldsymbol{\kappa}(\alpha_i)v_i$$

Therefore, by arranging the order of the states x, the subscript $k = 6$ represent the intrasegmental dynamics; $k = 1, ..., 5$ denote the intersegmental dynamics in state-space:

$$\mathcal{A}_k = \begin{cases} \frac{-1}{\tau_\gamma} I_{3\times 3} & \text{if } k = 6 \\ \frac{-1}{k\tau_d} I_{3\times 3} & \text{if } k = 1, ..., 5 \end{cases}$$

$$\mathcal{B}_k = \begin{cases} \frac{\mu_\gamma}{\tau_\gamma} I_{3\times 3} & \text{if } k = 6 \\ \frac{1}{k\tau_d} I_{3\times 3} & \text{if } k = 1, ..., 5 \end{cases}$$

Expressing $M(s) + BD(s)$ in state space representation, we will have:

$$\begin{cases} \dot{x}_{ki} = \mathcal{A}_k x_{ki} + \mathcal{B}_k \varphi(v_i) \cong \mathcal{A}_k x_{ki} + \mathcal{B}_k \boldsymbol{\kappa}(\alpha_i)v_i \\ v_i = (M_o + B_i \boldsymbol{\chi}_i)x_{6i} + \sum_{k=1}^{5} C_d x_{k,i-k} + \sum_{k=1}^{5} C_a x_{k,i+k} \end{cases} \tag{4.6}$$

where

$$M_o := \begin{bmatrix} 0 & -1 & 0 \\ 0 & 0 & -1 \\ -1 & 0 & 0 \end{bmatrix} \quad B_i := \begin{bmatrix} 0 \\ 0 \\ h_i \end{bmatrix} \quad C_d := \begin{bmatrix} 2 & 0 & 0 \\ 0 & 0 & 0 \\ 0 & 0 & 0 \end{bmatrix} C_a := \begin{bmatrix} 0 & -1 & 0 \\ 0 & 0 & -1 \\ 0 & 0 & 0 \end{bmatrix}$$

To write equation (4.6) in the form $\dot{x} = \tilde{\mathfrak{A}}x$ (not closed-loop equation containing plant states, only CPG controller):

$$\dot{x} = \tilde{\mathfrak{A}}x = (\mathfrak{A} + \mathfrak{B}\chi\mathfrak{C})x$$

$$\begin{bmatrix} \dot{x}_1 \\ \dot{x}_2 \\ \dot{x}_3 \\ \vdots \\ \dot{x}_6 \\ \vdots \\ \dot{x}_{12} \\ \vdots \\ \dot{x}_{17} \end{bmatrix} = (\underbrace{\begin{bmatrix} \mathcal{A}+\mathcal{M}_1 & \mathfrak{a}_1 e_1^\top & \mathfrak{a}_1 e_2^\top & \cdots & \mathfrak{a}_1 e_5^\top & \cdots & 0 \\ \mathfrak{d}_2 e_1^\top & \mathcal{A}+\mathcal{M}_2 & \mathfrak{a}_2 e_1^\top & \ddots & \ddots & \ddots & \vdots \\ \mathfrak{d}_3 e_2^\top & \mathfrak{d}_3 e_1^\top & \mathcal{A}+\mathcal{M}_3 & \ddots & \ddots & \ddots & 0 \\ \vdots & \vdots & \vdots & \ddots & \ddots & \ddots & \vdots \\ \mathfrak{d}_6 e_5^\top & \mathfrak{d}_6 e_4^\top & \mathfrak{d}_6 e_3^\top & \ddots & \ddots & \ddots & 0 \\ \vdots & \ddots & \ddots & \ddots & \ddots & \ddots & \vdots \\ 0 & \ddots & \ddots & \ddots & \ddots & \ddots & \mathfrak{a}_{12} e_5^\top \\ \vdots & \ddots & \ddots & \ddots & \ddots & \ddots & \vdots \\ 0 & \cdots & \mathfrak{d}_{17} e_5^\top & \cdots & \mathfrak{d}_{17} e_2^\top & \mathfrak{d}_{17} e_1^\top & \mathcal{A}+\mathcal{M}_{17} \end{bmatrix}_{306\times 306}}_{:=\mathfrak{A}} + $$

$$\underbrace{\begin{bmatrix} \underbrace{\begin{bmatrix} \mathcal{B}_1 \\ \vdots \\ \mathcal{B}_6 \end{bmatrix}}_{18\times 1} \kappa(\alpha_1) B_1 & & & & \\ & \begin{bmatrix} \mathcal{B}_1 \\ \vdots \\ \mathcal{B}_6 \end{bmatrix} \kappa(\alpha_2) B_2 & & & \\ & & \ddots & & \\ & & & \begin{bmatrix} \mathcal{B}_1 \\ \vdots \\ \mathcal{B}_6 \end{bmatrix} \kappa(\alpha_{17}) B_{17} \end{bmatrix}_{306\times 17}}_{:=\mathfrak{B}} \chi \underbrace{\begin{bmatrix} \mathrm{diag}(\underbrace{\begin{bmatrix} 0 & I_3 \end{bmatrix}}_{3\times 18}) \end{bmatrix}_{51\times 306}}_{:=\mathfrak{C}})x \tag{4.7}$$

where

$$x_i = \begin{bmatrix} x_{1i} \\ \vdots \\ x_{6i} \end{bmatrix}, \quad e_i = \begin{bmatrix} 0 \\ \vdots \\ 0 \\ I_3 \\ 0 \\ \vdots \\ 0 \end{bmatrix}_{18\times 3} \leftarrow \mathrm{i}^{th}, \quad \mathcal{A} = \begin{bmatrix} \mathcal{A}_1 & & & \\ & \mathcal{A}_2 & & \\ & & \ddots & \\ & & & \mathcal{A}_6 \end{bmatrix}, \quad \mathcal{M}_i = \begin{bmatrix} \mathcal{B}_1 \\ \vdots \\ \mathcal{B}_6 \end{bmatrix} \kappa(\alpha_i) M_o e_6^\top$$

$$\mathfrak{a}_i = \begin{bmatrix} \mathcal{B}_1 \\ \vdots \\ \mathcal{B}_6 \end{bmatrix} \kappa(\alpha_i) C_a, \quad \mathfrak{d}_i = \begin{bmatrix} \mathcal{B}_1 \\ \vdots \\ \mathcal{B}_6 \end{bmatrix} \kappa(\alpha_i) C_d$$

Removing $\pm j\omega$ from the eigenspce of $\tilde{\mathfrak{A}}(\chi)$, we will get a 2 dimension smaller matrix $\tilde{\mathfrak{A}}^-(\chi)$, which should be asymptotically stable satisfying

$$\tilde{\mathfrak{A}}^-(\chi) + (\tilde{\mathfrak{A}}^-(\chi))^\top < 0 \tag{4.8}$$

Equation (4.3), (4.4), and (4.8) should be considered in LMI to solve for χ.

4.1.1.3 Analytically minimal realization

The third method gives an analytically minimal realization. If we define $w := u - \tilde{u}$ and approximate the static nonlinearity $\varphi(v)$ by describing function $\kappa(\alpha)v$, the decomposed CPG model Eqn.(4.1) could be written as

$$v \cong \Big(M(s) + BD(s)\Big)\kappa(\alpha)v + Bw$$

Let $M(s)$ be decomposed into the block diagonal part $f(s)S_o$, and off diagonal (coupling) part of $L(s)$. The membrane potential v can be given by

$$v = L(s)\kappa v + f(s)S_o\kappa v + Bf(s)\chi\kappa v + Bw$$

$$= L(s)\kappa v + S_D f(s)\kappa v + Bw$$

$$S_D := S_o + B\chi$$

Let the state space realization be given as

$$L(s) = (A_l, B_l, C_l), \qquad f(s)I_{51} = (A_f, B_f, C_f), \qquad N(s) = (A_n, B_n, C_n).$$

Then the CPG controller is described as

$$\begin{bmatrix} \dot{x}_l \\ \dot{x}_f \\ \dot{x}_n \\ \hat{u} \\ \hat{u}_p \end{bmatrix} = \underbrace{\left[\begin{array}{ccc|c} A_l + B_l\kappa C_l & B_l\kappa S_D C_f & 0 & B_l\kappa B \\ B_f\kappa C_l & A_f + B_f\kappa S_D C_f & 0 & B_f\kappa B \\ B_n C_l & B_n S_D C_f & A_n & B_n B \\ \hline 0 & \chi C_f & 0 & 0 \\ 0 & -\chi C_f & C_n & 0 \end{array}\right]}_{:=\left[\begin{array}{c|c} A_c & B_c \\ \hline C_c & 0 \end{array}\right]} \begin{bmatrix} x_l \\ x_f \\ x_n \\ w \end{bmatrix} \tag{4.9}$$

The realization in (4.9) is a minimal realization with $A_c \in \mathbb{R}^{257\times257}$. $\begin{bmatrix} C_1 \\ C_2 \end{bmatrix} := C_c$.

4.1.2 Phasor conditions for CPG decomposition

Now we have the CPG model expressed in state-space, LMI conditions could be written out to find proper values for χ.

In closed-loop simulation, membrane potential v and total torque u strictly satisfy

$$v = M(s)\varphi(v) + Bu$$

After approximating $\varphi(v)$ by $\mathcal{K}(\alpha)v$, the left and right side of the equation are not exactly equal. Thus we use MHB analysis to find a proper α so that the new $\hat{v}$ and $\hat{u}$ strictly satisfy

$$\hat{v} = M(j\omega)\mathcal{K}(\alpha)\hat{v} + B\hat{u}$$

LMI condition 1: marginal stability

The first condition is to enforce the marginal stability of the CPG closed-loop system (not containing plant states). The oscillatory trajectory will converge to a stable limit cycle if there is one pair of eigenvalues on the imaginary axis (the oscillation frequency is the imaginary part), and the rest of eigenvalues are all located in the OLHP.

In the following equations, $\mathfrak{A}+\mathfrak{B}\chi\mathfrak{C}$ is the CPG closed-loop A matrix, γ is the LMI variable we want to minimize, representing the maximum real part of eig$(\mathfrak{A}+\mathfrak{B}\chi\mathfrak{C})$. If the result yields a γ close to zero, the closed-loop system is marginally stable.

$$\mathcal{D}(\mathfrak{A}+\mathfrak{B}\chi\mathfrak{C})N + [\mathcal{D}(\mathfrak{A}+\mathfrak{B}\chi\mathfrak{C})N]^\top < \gamma I$$

$$\therefore \mathcal{D}\mathfrak{B}\chi\mathfrak{C}N + (\mathcal{D}\mathfrak{B}\chi\mathfrak{C}N)^\top + (\mathcal{D}\mathfrak{A}N + N^\top\mathfrak{A}^\top\mathcal{D}^\top) < \gamma I$$

where

$$\begin{bmatrix}\mathcal{C}\\ \mathcal{D}\end{bmatrix} = \begin{bmatrix}R & N\end{bmatrix}^{-1}$$

$$N = \mathcal{N}(R^\top), \quad R = [\Re(\hat{x}) \quad \Im(\hat{x})]$$

$$\hat{x}_{ki} = (j\omega I - \mathcal{A}_k)^{-1}\mathcal{B}_k\mathcal{K}(\alpha_i)\hat{v}_i, \quad k = 1,...,6, i = 1,...,17$$

LMI condition 2: MHB equation for the decomposed CPG

According to Equation (4.4),

$$f(j\omega)B\chi\mathcal{K}(\alpha)\hat{v} = \hat{v} - M(j\omega)\mathcal{K}(\alpha)\hat{v}$$

$$\therefore B\chi\mathcal{K}(\alpha)\hat{v} = \underbrace{\frac{1}{f(j\omega)}[I - M(j\omega)\mathcal{K}(\alpha)]}_{\triangle}\hat{v}$$

Since all the matrices in LMI should be real matrices, we will separate the real part and imaginary part of the elements in $\boldsymbol{\kappa}(\alpha)\hat{v}$ and $\triangle$.

$$B\chi \underbrace{[\mathrm{Re}(\boldsymbol{\kappa}(\alpha)\hat{v}) \quad \mathrm{Im}(\boldsymbol{\kappa}(\alpha)\hat{v})]}_{\mathbb{F},51\times 2} = \underbrace{[\mathrm{Re}(\triangle) \quad \mathrm{Im}(\triangle)]}_{\mathbb{G}_1,51\times 2}$$

$$\Rightarrow \begin{bmatrix} \epsilon_1 I & B\chi\mathbb{F} - \mathbb{G}_1 \\ (B\chi\mathbb{F} - \mathbb{G}_1)^\top & \epsilon_1 I \end{bmatrix} > 0$$

LMI condition 3: reference generation of desired torque $\hat{u}$

According to Equation (4.3), the decomposed part of CPG should satisfy the following:

$$f(j\omega)\chi\boldsymbol{\kappa}(\alpha)\hat{v} = \hat{u}$$

$$\therefore \chi\boldsymbol{\kappa}(\alpha)\hat{v} = \frac{1}{f(j\omega)}\hat{u}$$

$$\chi \underbrace{[\mathrm{Re}(\boldsymbol{\kappa}(\alpha)\hat{v}) \quad \mathrm{Im}(\boldsymbol{\kappa}(\alpha)\hat{v})]}_{\mathbb{F},51\times 2} = \underbrace{[\mathrm{Re}(\frac{1}{f(j\omega)}\hat{u}) \quad \mathrm{Im}(\frac{1}{f(j\omega)}\hat{u})]}_{\mathbb{G}_2,17\times 2}$$

$$\Rightarrow \begin{bmatrix} \epsilon_2 I & \chi\mathbb{F} - \mathbb{G}_2 \\ (\chi\mathbb{F} - \mathbb{G}_2)^\top & \epsilon_2 I \end{bmatrix} > 0$$

Enforcing LMI condition 3 by pseudo-inverse

Actually, from condition 3 and original CPG equation:

$$f(j\omega)\chi\boldsymbol{\kappa}(\alpha)\hat{v} = \hat{u}$$

$$\hat{v} = M(j\omega)\boldsymbol{\kappa}(\alpha)\hat{v} + B\hat{u}$$

We could obtain condition 2:

$$\Rightarrow \hat{v} = M(j\omega)\boldsymbol{\kappa}(\alpha)\hat{v} + Bf(j\omega)\chi\boldsymbol{\kappa}(\alpha)\hat{v}$$

Since condition 3 has lower dimension, we choose only to implement LMI condition 1 and 3.

Let's take a closer look at condition 3. The use of LMI might not be necessary:

$$\hat{u} = \chi \underbrace{f(j\omega)\kappa(\alpha)\hat{v}}_{:=W_o}$$

For each entry of $\hat{u}$, it can be expressed by the element of W_o:

$$\hat{u}_i = \begin{bmatrix} x_{i1} & x_{i2} & x_{i3} \end{bmatrix} \begin{bmatrix} \hat{w}_{i1} \\ \hat{w}_{i2} \\ \hat{w}_{i3} \end{bmatrix}$$

Then we separate the real and imaginary part of the above matrices:

$$\underbrace{\begin{bmatrix} \Re(\hat{u}_i) & \Im(\hat{u}_i) \end{bmatrix}}_{:=U \in \mathbb{R}^2} = \begin{bmatrix} x_{i1} & x_{i2} & x_{i3} \end{bmatrix} \underbrace{\begin{bmatrix} \Re \begin{bmatrix} \hat{w}_{i1} \\ \hat{w}_{i2} \\ \hat{w}_{i3} \end{bmatrix} & \Im \begin{bmatrix} \hat{w}_{i1} \\ \hat{w}_{i2} \\ \hat{w}_{i3} \end{bmatrix} \end{bmatrix}}_{:=W \in \mathbb{R}^{3\times 2}} \tag{4.10}$$

$$\therefore U_i = \chi_i W_i$$

$$\Rightarrow \chi_i = U_i W_i^\dagger + Z_i(I - W_i W_i^\dagger)$$

- If we set $x_{i3} \neq 0$, equation (4.10) is under parametrized, we will have one more degree of freedom in Z_i. If we set $Z_i = 0$, then we will obtain solution χ with minimum norm, and this χ is very likely to be different from the χ obtained from LMI calculation.

- If we set $x_{i3} = 0$, which physically means intrasegmental connection within the third neuron in each segment is forbidden, then we will get a unique solution for equation (4.10), and this χ is theoretically identical with the χ obtained from LMI calculation. If we choose to obtain χ in this fashion, we can avoid running LMI calculation, and the marginal stability condition (condition 1) can be checked by plotting the eigenvalue distribution of $\tilde{\mathfrak{A}}$ after plugging χ.

Therefore, there are three decomposition processes we can choose from:

Process a

Process a is enforcing condition 1, 2 and 3 in constraints and minimizing γ, the maximum real part of the eigenvalues of closed-loop A matrix.

$$\begin{aligned}
&\min_{\chi} \quad \gamma \\
&\text{s.t.} \quad \mathcal{D}\mathfrak{B}\chi\mathfrak{C}N + (\mathcal{D}\mathfrak{B}\chi\mathfrak{C}N)^{\top} + (\mathcal{D}\mathfrak{A}N + N^{\top}\mathfrak{A}^{\top}\mathcal{D}^{\top}) < \gamma I \\
&\qquad \begin{bmatrix} \epsilon_1 I & B\chi\mathbb{F} - \mathbb{G}_1 \\ (B\chi\mathbb{F} - \mathbb{G}_1)^{\top} & \epsilon_1 I \end{bmatrix} > 0 \\
&\qquad \begin{bmatrix} \epsilon_2 I & \chi\mathbb{F} - \mathbb{G}_2 \\ (\chi\mathbb{F} - \mathbb{G}_2)^{\top} & \epsilon_2 I \end{bmatrix} > 0.
\end{aligned} \tag{4.11}$$

Process b

This process uses pseudo-inverse to calculate χ, with one more degree of freedom as χ_{i3} is not zero.

$$\chi_i = U_i W_i^{\dagger} + Z_i(I - W_i W_i^{\dagger}), \quad Z_i = 0,\ \chi_{i3} \neq 0 \tag{4.12}$$

Process c

This process also uses pseudo-inverse to calculate χ. With $\chi_{i3} = 0$, we will obtain an unique analytical solution of χ.

$$\chi_i = U_i W i^{\dagger} + Z_i(I - W_i W_i^{\dagger}), \quad Z_i = 0,\ \chi_{i3} = 0 \tag{4.13}$$

4.1.3 Stability analysis by simulation of decomposed CPG

After getting χ both from LMI (process a) and pseudo-inverse method (process b and c), we run simulation of the equation

$$v = \Big(M(s) + BD(s)\Big)\varphi(v), \quad D(s) = f(s)\chi. \tag{4.14}$$

This is the equation of decomposed, conservative CPG. It is expected to see the CPG reproduces phase lag of v close to 360° in nominal water and air traveling, and generates standing waves in air standing case.

4.1.3.1 Nominal water

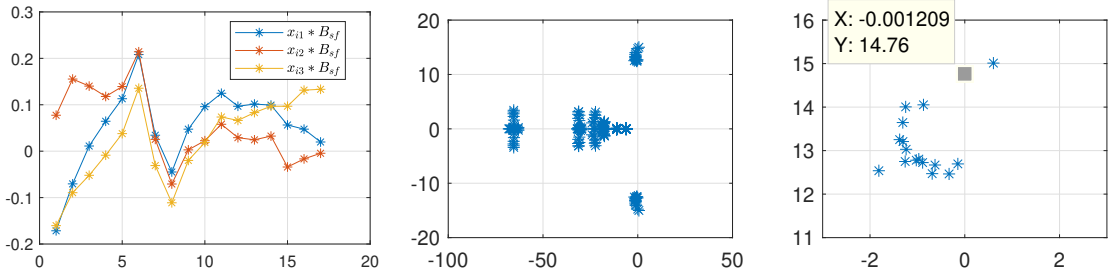

Figure 4.2: Process a; sensory feedback B multiplied by χ and eigenvalues of $\tilde{\mathfrak{A}}$

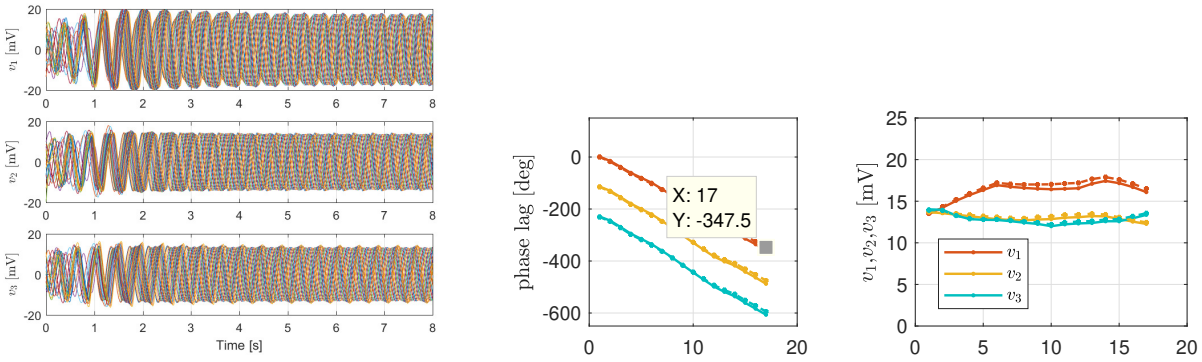

Figure 4.3: Time domain signal of Eqn.(4.14); phase lag and amplitude of membrane potential v: simulation of closed-loop CPG-plant system, 15.96 Hz(solid); Eqn.(4.14), 15.80 Hz (dashed)

The left figure in Fig. 4.2 is the dot product of χB, the amplitude of which is around 0.2. Comparing with the absolute value of the elements of the connectivity matrices in Eqn.(4.6), which are 1 or 2, the value of χ is reasonable in terms of amplitude. The middle figure is the eigenvalue distribution of matrix $\tilde{\mathfrak{A}}$; right is the close-up around imaginary axis. We see

with the approximation of static nonlinearity by describing function in $\tilde{\mathfrak{A}}$, there is a pair of eigenvalue in the ORHP.

The stability of the nonlinear system of Eqn.(4.14) could be checked by simulation. The left figure above is the time-domain signal of membrane potential v, which reaches and maintains stable oscillation around $t = 3$s, after going through some transients at the initial stage. The middle and right figures are the phase lag and amplitude of v at each segment. The solid line is the result of closed-loop CPG-plant system simulation in chapter 2, from which it is expected to see little deviation of simulation of Eqn.(4.14), showed in dashed line. The smallness of the gap between dashed and solid lines signifies that one of the functionality of the decomposed, conservative CPG is the internal reference generation of desired closed-loop membrane potential v.

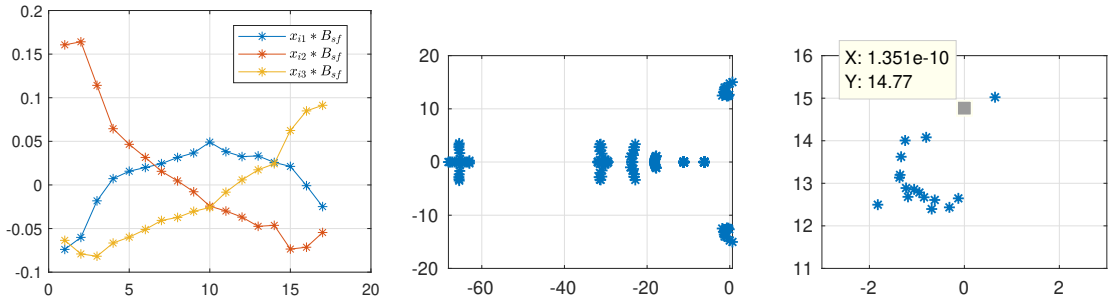

Figure 4.4: Process b; sensory feedback B multiplied by χ and eigenvalues of $\tilde{\mathfrak{A}}$

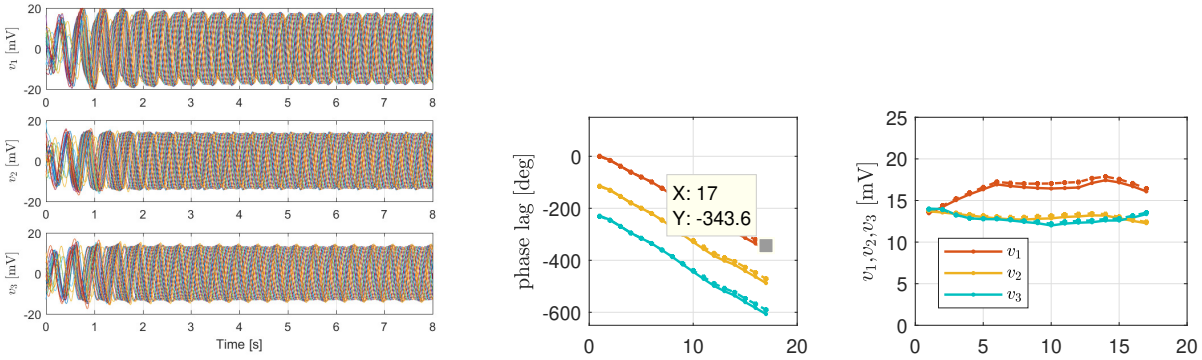

Figure 4.5: Solid: closed-loop, 15.96 Hz; dashed: decomposed CPG, 15.82 Hz

Similar results are also yielded by Process b, in terms of χ amplitude, eigenvalue distribution, and nonlinear simulation stability.

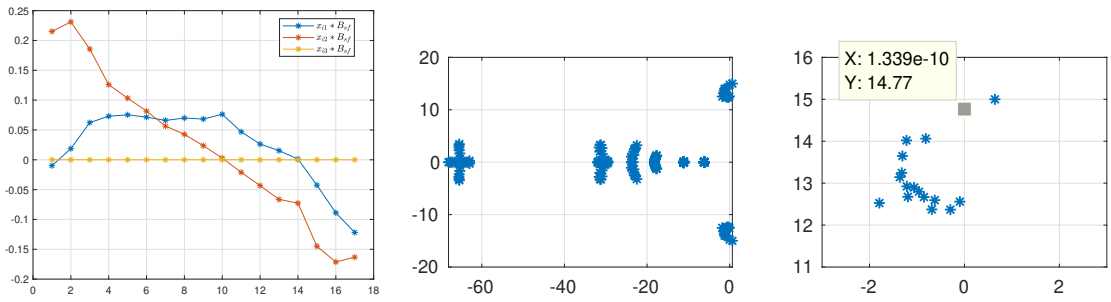

Figure 4.6: Process c; sensory feedback B multiplied by χ and eigenvalues of $\tilde{\mathfrak{A}}$

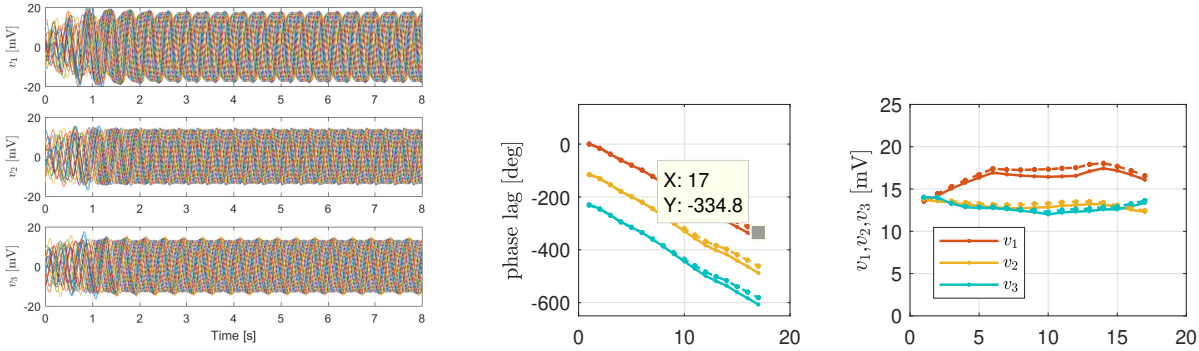

Figure 4.7: Solid: closed-loop, 15.96 Hz; dashed: decomposed CPG, 15.75 Hz

Similar results are also yielded by Process c, in terms of χ amplitude, eigenvalue distribution, and nonlinear simulation stability. One thing to be noticed is that, since $\chi_{i3} = 0$ in Process c, the yellow line is flat at value 0 as expected in Fig. 4.6.

4.1.3.2 Air standing

Similar results are also yielded by Process a, b and c for air standing simulation of Eqn.(4.14), in terms of χ amplitude, eigenvalue distribution, and nonlinear simulation stability. The time-domain signal of v converges to stable standing wave oscillation after $t = 3$s. The gap

between closed-loop CPG-plant system simulation and Eqn.(4.14) simulation is minor, per oscillation profile (frequency, amplitude, phase lag).

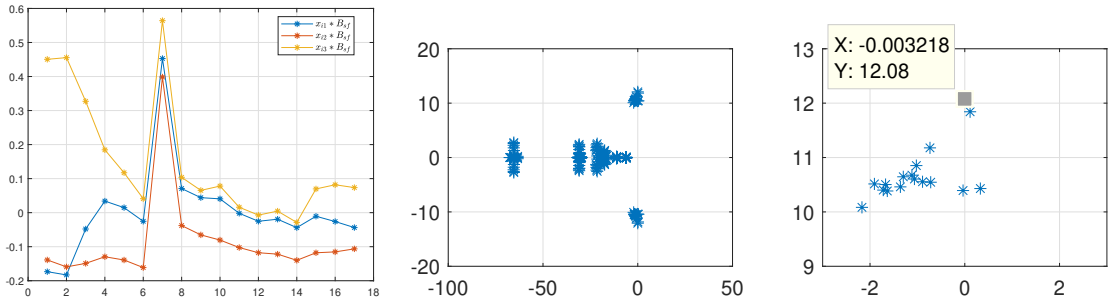

Figure 4.8: Process a; sensory feedback multiplied by χ and eigenvalues of $\tilde{\mathfrak{A}}$

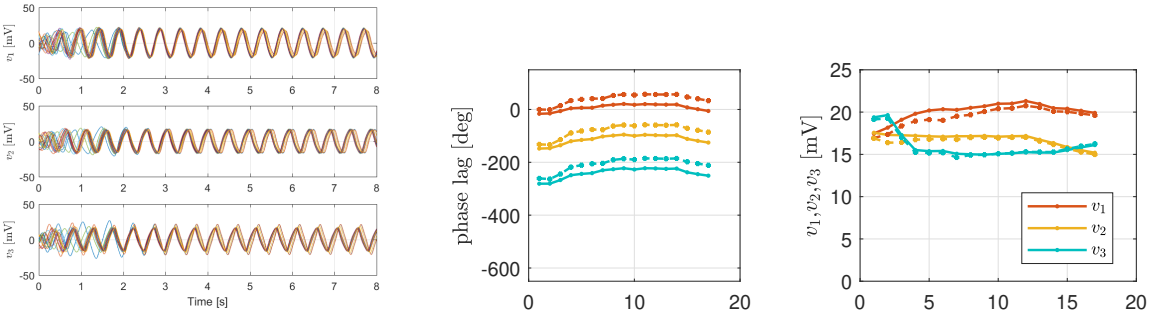

Figure 4.9: Solid: closed-loop, 12.80 Hz; dashed: decomposed CPG, 12.99Hz

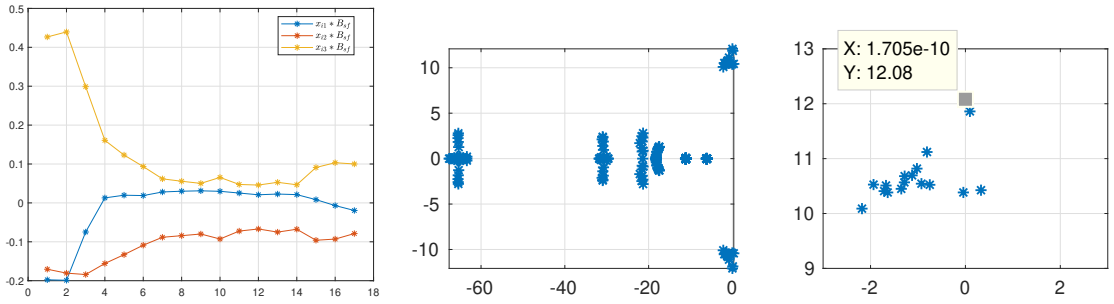

Figure 4.10: Process b; sensory feedback multiplied by χ and eigenvalues of $\tilde{\mathfrak{A}}$

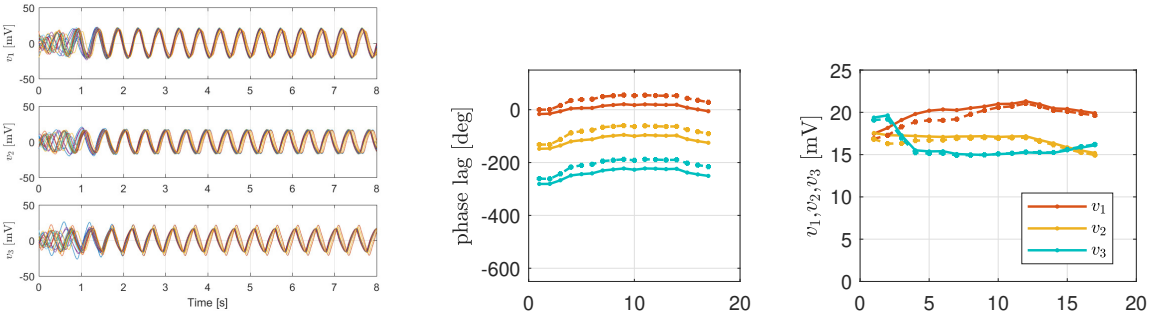

Figure 4.11: Solid: closed-loop, 12.80 Hz; dashed: decomposed CPG, 13.03 Hz

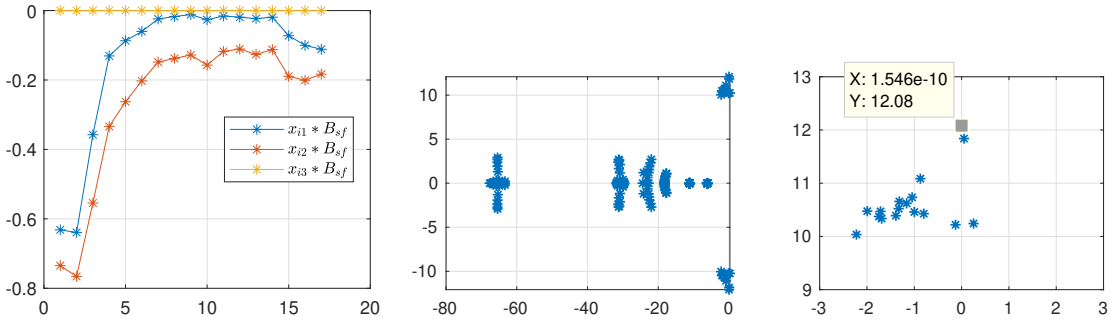

Figure 4.12: Process c; sensory feedback multiplied by χ and eigenvalues of $\tilde{\mathfrak{A}}$

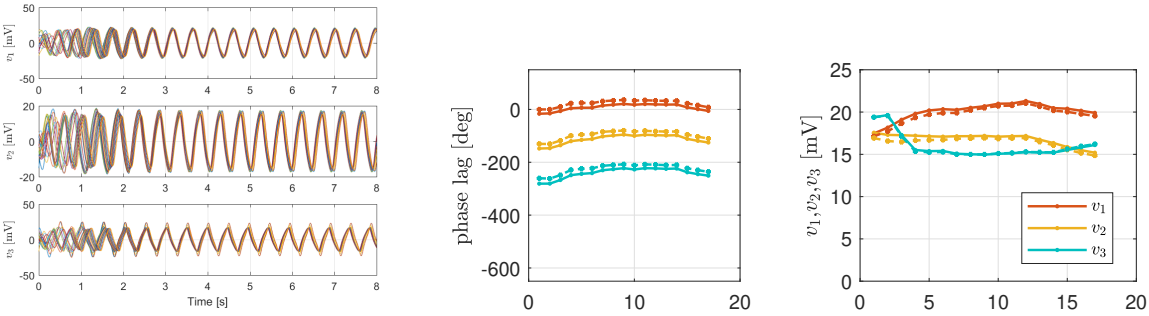

Figure 4.13: Solid: closed-loop, 12.80 Hz; dashed: decomposed CPG, 13.07 Hz

4.1.3.3 Air traveling

Similar results are also yielded by Process a, b and c for air traveling simulation of Eqn.(4.14), in terms of χ amplitude, eigenvalue distribution, and nonlinear simulation stability. The time-domain signal of v converges to stable standing wave oscillation after $t = 2$s. The gap between closed-loop CPG-plant system simulation and Eqn.(4.14) simulation is minor, per oscillation profile (frequency, amplitude, phase lag).

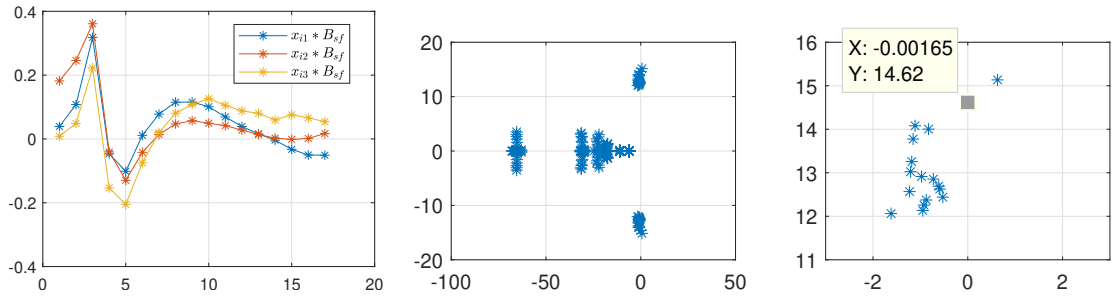

Figure 4.14: Process a; sensory feedback multiplied by χ and eigenvalues of $\tilde{\mathfrak{A}}$

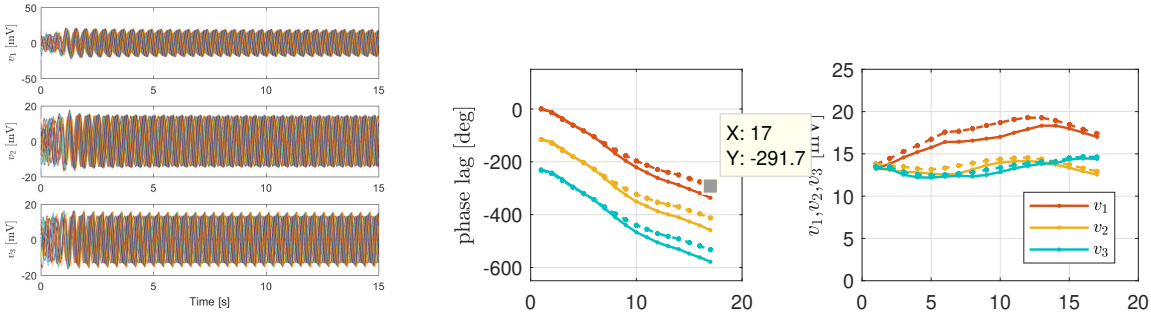

Figure 4.15: Solid: closed-loop, 15.98 Hz; dashed: decomposed CPG, 15.45 Hz

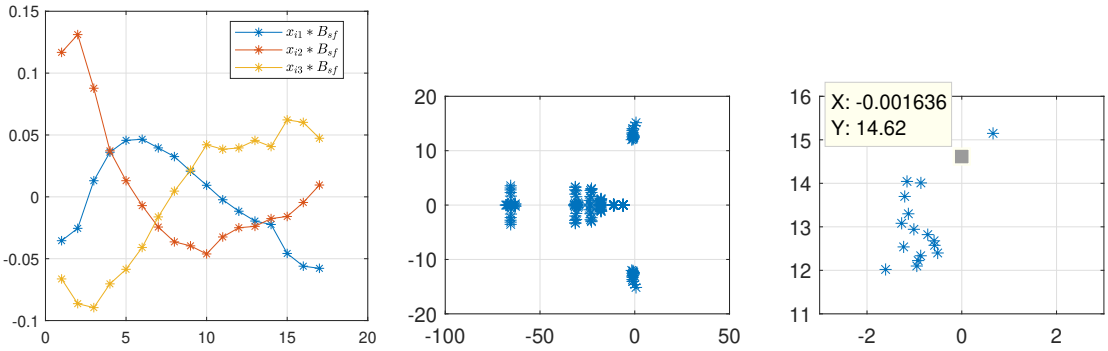

Figure 4.16: Process b; sensory feedback multiplied by χ and eigenvalues of $\tilde{\mathfrak{A}}$

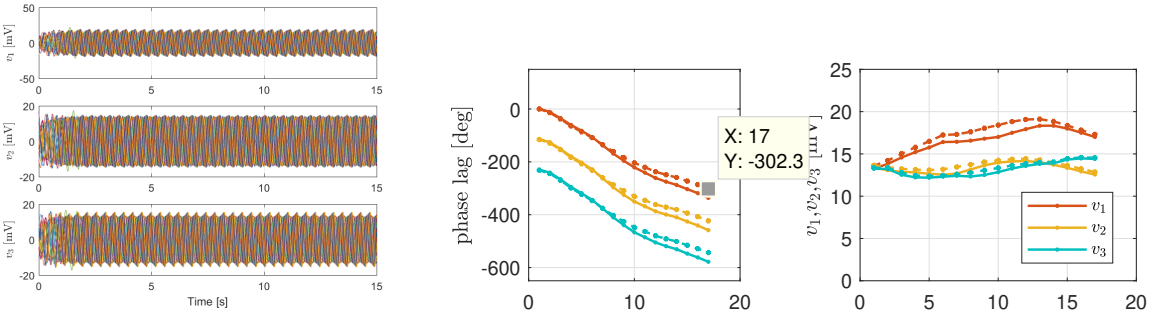

Figure 4.17: Solid: closed-loop, 15.98 Hz; dashed: decomposed CPG, 15.53 Hz

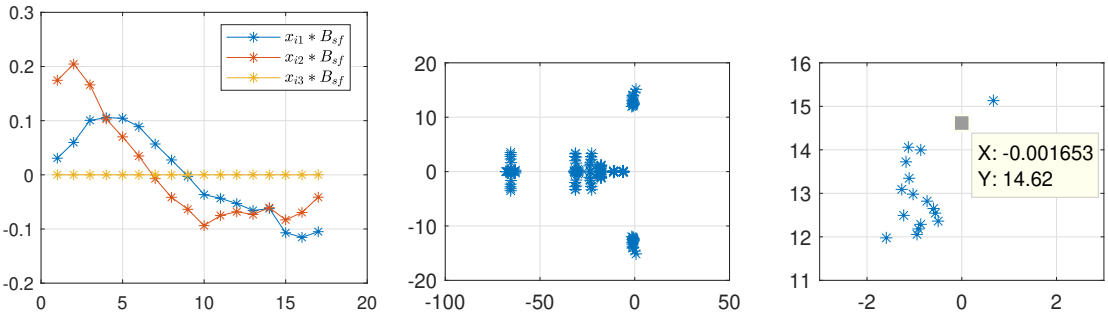

Figure 4.18: Process c; sensory feedback multiplied by χ and eigenvalues of $\tilde{\mathfrak{A}}$

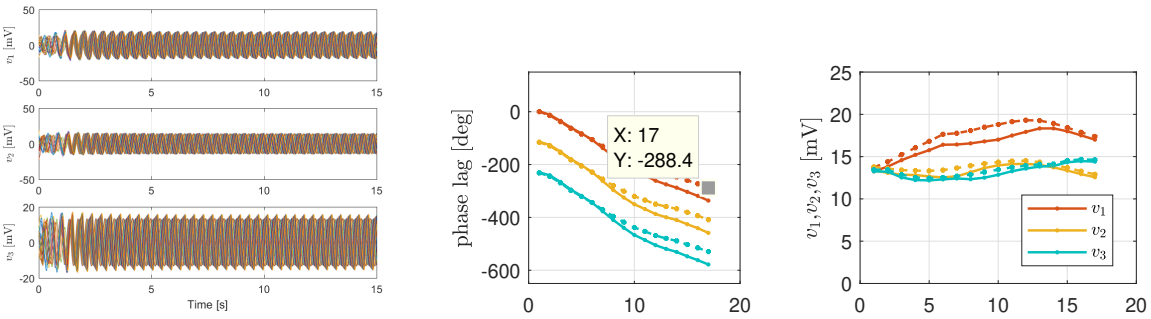

Figure 4.19: Solid: closed-loop, 15.98 Hz; dashed: decomposed CPG, 15.47 Hz

From the results above, we conclude that

- In nominal water, air standing and air swimming these three cases, utilizing Process a, b and c, the gap between closed-loop CPG-plant system simulation and Eqn.(4.14) simulation is minor, per oscillation profile (frequency, amplitude, phase lag).
- The eigenvalue distribution plot of matrix $\tilde{\mathfrak{A}}$ by all three processes will have a pair of eigenvalues in ORHP. This shows that
  - The LMI method (Process a), intended to minimize the maximum real part of eigenvalues of $\tilde{\mathfrak{A}}$, is conservative: only minimizing the upper bound of the maximum real parts.
  - The pseudo-inverse method (Process b and c), minimizing the error norm, also fail to generate a set of χ that pushes that pair of eigenvalues to the OLHP.

  We see no difference in the sets of χ obtained by these three processes. In the consideration of avoiding self-feedback effect (sensory feedback matrix B is a block-diagonal matrix with non-zero element populated at the 3rd element in each block), we choose to adopt Process c for later study.

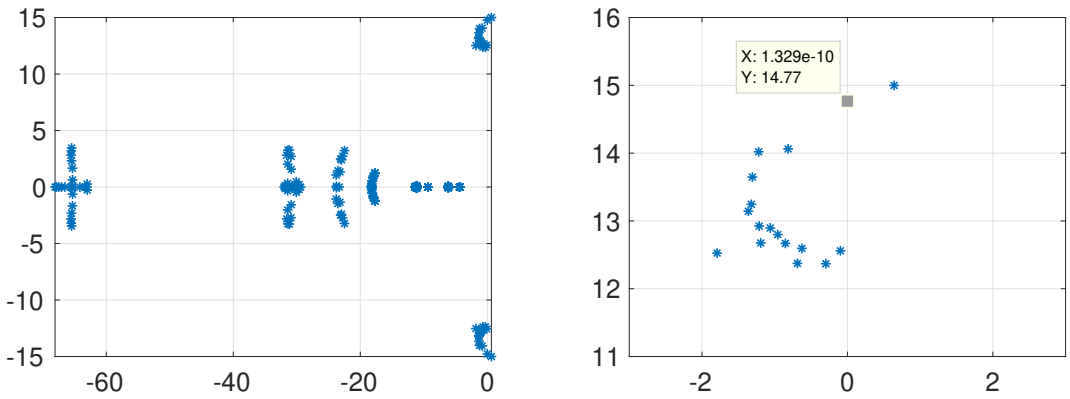

Figure 4.20: Eigenvalue distribution of A_c from realization 3

There is one eigenvalue in the ORHP, consistent with the ideal CPG simulation result above.

4.2 Eigenstructure analysis of the closed-loop system

4.2.1 Quasi-linearization via describing function

After finding out the dynamics responsible for generating the reference signal $\tilde{u}$ for the plant in section 4.1 ($\tilde{u} := D(s)\varphi(v)$), we proposed a control architecture using eigenstructure theory which can well explain that CPG is responsible for both reference generation and closed-loop stabilization.

Using describing function $\mathcal{K}$ to approximate the static nonlinearity, the following are the equations of the quasi-linearized CPG-plant system:

$$
\begin{aligned}
u_P &= k_o\phi + c_m\dot{\phi} := \mathbb{K}x_p \\
u_A &= N(s)v \\
\hat{u} &:= D(s)\kappa v, \qquad D(s) := f(s)\chi = \frac{\mu_\gamma}{1+\tau_\gamma s}\chi \\
\hat{u}_P &:= u_A - \hat{u} = (N(s) - D(s)\kappa)v \\
w &:= \hat{u}_P - u_P = (N(s) - f(s)\chi\kappa)v - \mathbb{K}x_p \\
&= C_2 x_N - C_1 x_f - \mathbb{K}x_p \\
u &= w + \hat{u} \\
v &= (M(s) + BD(s))\kappa v + Bw
\end{aligned}
\tag{4.15}
$$

4.2.2 Eigenstructure and stability of oscillation

The block diagram in Fig. 4.21 visualize Eqn. (4.15).

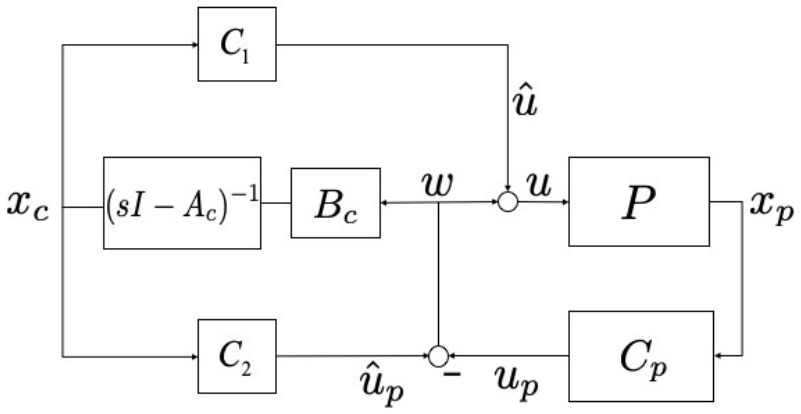

Figure 4.21: Eigenstructure in leech system

In real life, one likely scenario would be that we want the plant to maintain a stable periodic movement. For example, a bipedal robot in walking, or a operational robot helping clean windows. For the closed-loop system to have a desired solution, the controller needs to embed the desired dynamics.

Lemma 1. *Consider the feedback control system*

$$\begin{aligned} &\dot{x}_p = A_p x_p + B_p u, \\ &y = C_p x_p, \end{aligned} \qquad \begin{aligned} &\dot{x}_c = A_c x_c + B_c w, \\ &u = C_1 x_c + w, \\ &w = C_2 x_c - y. \end{aligned} \tag{4.16}$$

Suppose, for each vector η, there exists a solution of the closed-loop system such that

$$x_p(t) = X_p e^{\Lambda t}\eta, \quad w(t) = 0.$$

Then there exists X_c such that

$$\begin{aligned} &A_c X_c = X_c \Lambda, && C_2 X_c = C_p X_p, \\ &A_p X_p + B_p U = X_p \Lambda, && U := C_1 X_c. \end{aligned} \tag{4.17}$$

Moreover, $x_c(t) = X_c e^{\Lambda t}\eta$ holds on the solution.

Proof. The closed-loop system can be described as

$$\dot{x} = Ax, \quad w = Cx,$$

where

$$x := \begin{bmatrix} x_p \\ x_c \end{bmatrix}, \quad A := \begin{bmatrix} A_p - B_p C_p & B_p(C_1 + C_2) \\ -B_c C_p & A_c + B_c C_2 \end{bmatrix}, \quad C := \begin{bmatrix} -C_p & C_2 \end{bmatrix}$$

The supposd properties imply

$$AX = X\Lambda, \quad CX = 0, \quad X := \begin{bmatrix} X_p \\ X_c \end{bmatrix}$$

for some X_c. These equations are equivalent to (4.17). □

In MATLAB verification, $AX = X\Lambda$ holds by $1e-10$ error; $CX = 0$ holds by $1e-17$ error.

The leech swimming system in Fig. 4.21 has an additional property that the body oscillation x_p in the steady state (or the gait) can be generated by a linear combination of the CPG state x_c (e.g. the neuronal membrane potential v can be scaled to generate ϕ). This means that there is a matrix C_o such that $X_p = C_o X_c$. Using this property, the oscillatory mode Λ can be isolated from the closed-loop dynamics as follows.

Lemma 2. *Consider the feedback system (4.16). Suppose, for each vector η, there exists a solution of the closed-loop system such that*

$$x_p(t) = X_p e^{\Lambda t}\eta, \quad x_c(t) = X_c e^{\Lambda t}\eta, \quad w(t) = 0$$

Then X_p and X_c satisfy (4.17). Suppose further that there exists C_o such that $X_p = C_o X_c$, then every solution converges to the above solution for some η if and only if the system

$$\begin{bmatrix} \dot{\zeta} \\ \dot{\theta} \end{bmatrix} = \begin{bmatrix} A_p - \mathfrak{B}\mathring{Q}C_p & Z \\ HQ_2C_p & S \end{bmatrix} \begin{bmatrix} \zeta \\ \theta \end{bmatrix} \tag{4.18}$$

is asymptotically stable, where

$$\mathfrak{B} := [B_p \quad -C_o], \ \mathring{Q} := \begin{bmatrix} Q_1 \\ Q_2 \end{bmatrix} = \begin{bmatrix} I \\ B_c \end{bmatrix}, \ Z := (C_oA_c - A_pX - B_pU)F,$$

F, S, G, H is defined by the spectral decomposition of A_c : $\begin{bmatrix} X_c & F \end{bmatrix} \begin{bmatrix} \Lambda & 0 \\ 0 & S \end{bmatrix} \begin{bmatrix} G \\ H \end{bmatrix} = A_c.$

Proof. Consider the coordinate transformation:

$$\begin{bmatrix} \theta \\ \gamma \end{bmatrix} := \begin{bmatrix} H \\ G \end{bmatrix} x_c, \quad \zeta := C_o x_c - x_p.$$

Then, using the properties in (4.17), the closed-loop system is described as

$$\begin{bmatrix} \dot{\zeta} \\ \dot{\theta} \\ \dot{\gamma} \end{bmatrix} = \underbrace{\begin{bmatrix} A_p - \mathfrak{B}\mathring{Q}C_p & Z & 0 \\ HQ_2C_p & S & 0 \\ GQ_2C_p & 0 & \Lambda \end{bmatrix}}_{A_{cl}} \begin{bmatrix} \zeta \\ \theta \\ \gamma \end{bmatrix}. \tag{4.19}$$

Thus we have the result. □

Let's take a closer look at Eqn.(4.19). A_{cl} is a block matrix, with Λ being a 2×2 matrix representing the oscillatory mode; S being a 255×255 matrix in leech example, containing all the stables modes in CPG. The above lemma tells us $\mathring{Q}$ is responsible for stabilizing

$$\begin{bmatrix} A_p & Z \\ 0 & S \end{bmatrix} + \begin{bmatrix} \mathfrak{B} \\ \begin{bmatrix} 0 & H \end{bmatrix} \end{bmatrix} \mathring{Q} \begin{bmatrix} C_p & 0 \end{bmatrix}$$

in the closed-loop system.

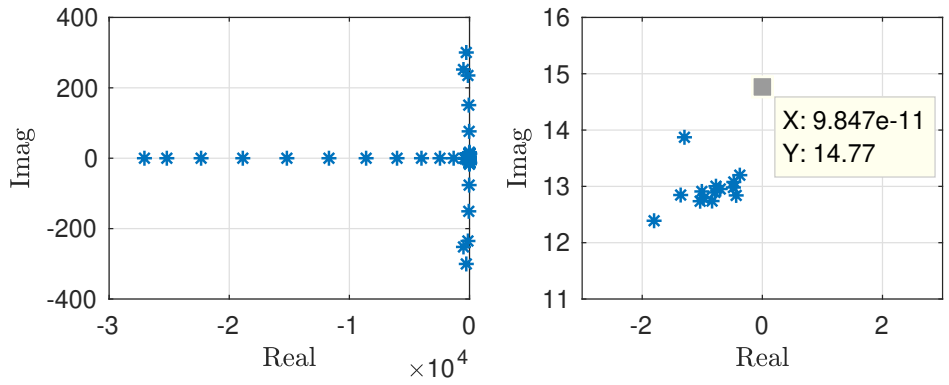

Figure 4.22: Eigenvalue distribution of closed-loop system

The max real part of the closed-loop eigenvalue is of 1e-11 order.

4.3 Control mechanisms from decomposed CPG perspective

By exploiting the control architecture of eigenstructure for leech, we found that the weak coupling through $\mathring{Q}_2$ between neural and mechanical dynamics and the weak feedabck gain in $\hat{u}$ can well explain the stabilization mechanism of CPG under environmental perturbations.

4.3.1 Weak coupling of neural and mechanical dynamics

Define the $(1,1)$ block of (4.19) to be R, and R_o is the approximation of R:

$$R := \begin{bmatrix} A_p - \mathfrak{B}\mathring{Q}C_p & Z \\ HQ_2C_p & S \end{bmatrix} \cong R_o := \begin{bmatrix} A_p - \mathfrak{B}\mathring{Q}C_p & Z \\ 0 & S \end{bmatrix}. \tag{4.20}$$

This approximation is valid if the stabilizing effect of $\mathring{Q}_2$ is sufficiently small. The "smallness" is justified by:

$$\|A_p\| = 1.65e3, \quad \|B_p\mathring{Q}_1C_p\| = 9.02e6, \quad \|C_o\mathring{Q}_2C_p\| = 1.07e3$$

$$\begin{bmatrix} \|A_p - \mathfrak{B}\mathring{Q}C_p\| & \|Z\| \\ \|H\mathring{Q}_2C_p\| & \|S\| \end{bmatrix} = \begin{bmatrix} 9.01e6 & 1.41e5 \\ 6.6e3 & 7.08e1 \end{bmatrix}$$

- $\|C_o\mathring{Q}_2C_p\| \ll \|B_p\mathring{Q}_1C_p\|$: the direct feedback to the plant dynamics is much smaller for $\mathring{Q}_2$ than $\mathring{Q}_1$.
- $\text{eig}(R) \cong \text{eig}(R_o)$

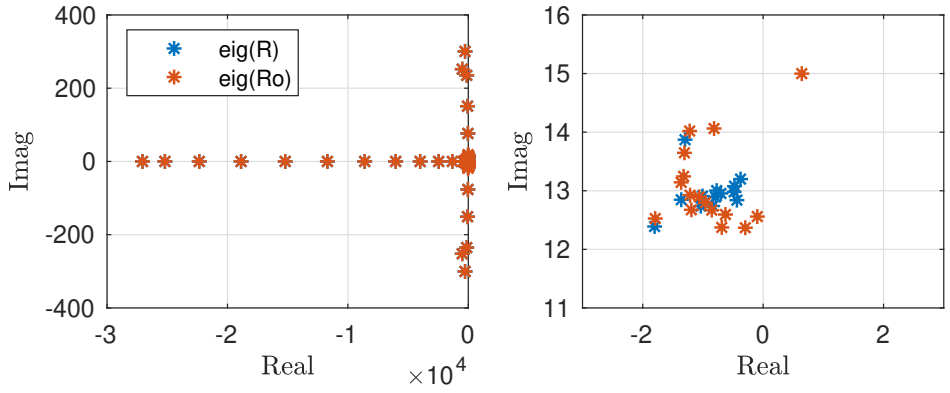

Figure 4.23: Eigenvalue distributions of R and R_o: max(real(eig(R))) = -0.37, max(real(eig(R_o))) = 0.64

- Eigenvalue distributions of A_p, R, S, and $A_p - B_p Q_1 C_p$: the open-loop plant A_p (body-fluid without stiffness) is unstable, but is stabilized by the muscle stiffness $B_p Q_1 C_p$ (the eigenvalues in purple hexagram outside the shown range are all stable). The isolated neural control dynamics S are not strictly stable (the largest real part is 0.64) but are roughly marginally stable. The coupling of the neural and mechanical dynamics through Q_2 does not move the eigenvalues with a significant amount as seen by the distributions of yellow and red markers (they are also close to each other outside the shown range). Hence, weak sensory feedback to the CPG (i.e. small Q_2) maintains the stability property.

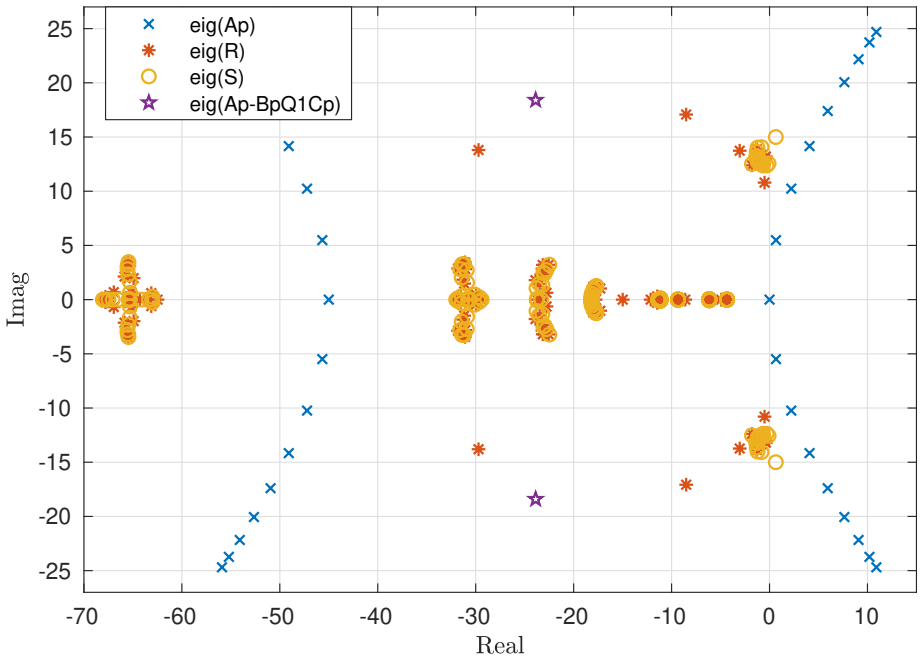

Figure 4.24: Eigenvalue distributions of A_p, R, S, and $A_p - B_p Q_1 C_p$

The control mechanism may be explained as follows. When $\mathring{Q}_2 = 0$, the CPG acts as the exogenous reference generator which drives the plant stabilized by feedback $\mathring{Q}_1$ (with only one eigenvalue having positive real part 0.64, whose effect is not pivotal under the static nonlinearity in simulation). The reference tracking would be achieved by stability of the feedback system consisting of the plant and $\mathring{Q}_1$. When $\mathring{Q}_2$ is nonzero but small, the stability property is maintained due to continuity of the eigenvalues, and the CPG (reference generator) receives sensory feedback from the plant through $\mathring{Q}_2$ so that the target oscillation pattern can be modified under perturbations.

4.3.2 Benefit of sensory feedback

The following two block diagrams demonstrate that when $\mathring{Q}_2 = 0$, the original non-decomposed CPG functions as an exogenous reference generator.

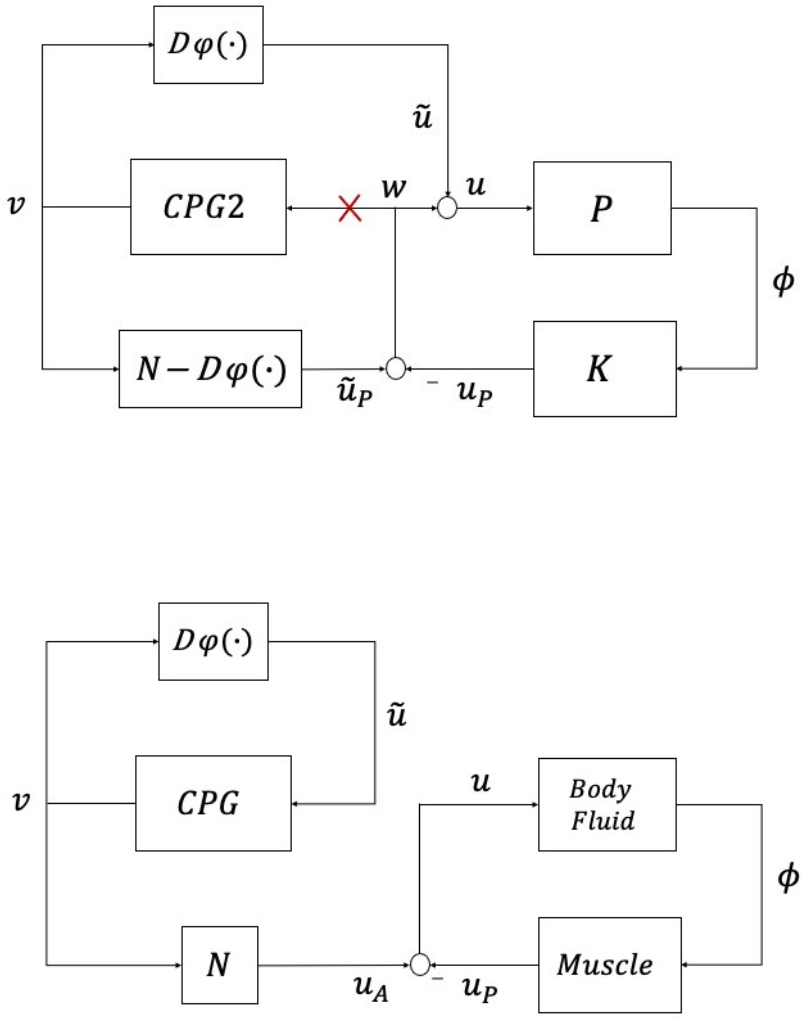

Figure 4.25: What happens to the original CPG when $\mathring{Q}_2 = 0$

Simulation verification: the benefit of $\mathring{Q}_2$ under perturbations

Here to verify that through $\mathring{Q}_2$ the CPG can modify the original reference signal so to drive the plant to another oscillation pattern to better suit the environmental changes, we simulated the closed-loop leech system (Fig. 4.1b) under these conditions:

Case 1. Nominal swimming in water.

Case 2. Change the tangential drag coefficient $c_t' = 3c_t$, while $\mathring{Q}_2 = 0$.

Case 3. Change the tangential drag coefficient $c_t' = 3c_t$, while $\mathring{Q}_2 = B_c$.

We increased the tangential drag coefficient to three times as large as the original value in case 2 and 3 in order to see how leech CPG reacts when drag/thrust ratio is a lot larger than in nominal water case. For case 2 and 3, the initial states are set to be the steady states of case 1 nominal swimming.

Table 4.1: Simulation result summary

Case	Period [ms]	u Amplitude [10^{-5} Nm]	ϕ Phase lag	Speed [m/s]
1	393	0.91	360°	0.1258
2	398	1.88	335°	0.0786
3	384	0.89	397°	0.0490

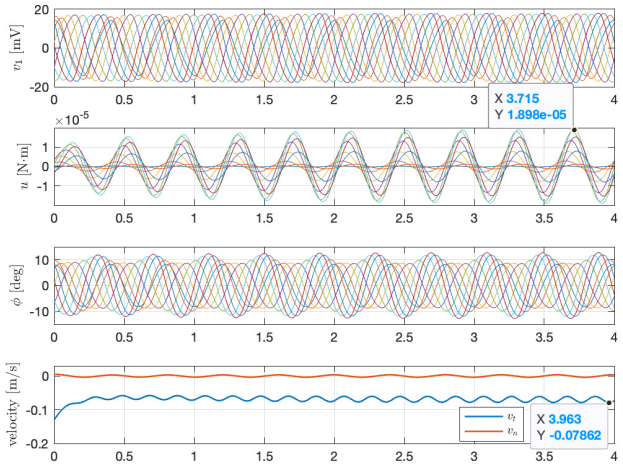

(a) v_1, u, ϕ and center mass velocity

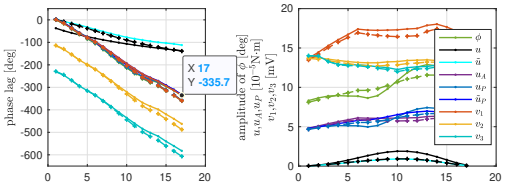

(b) Solid: phase and amplitude of case 2; dashed: case 1

Figure 4.26: Simulation result for case 2 in comparison with case 1

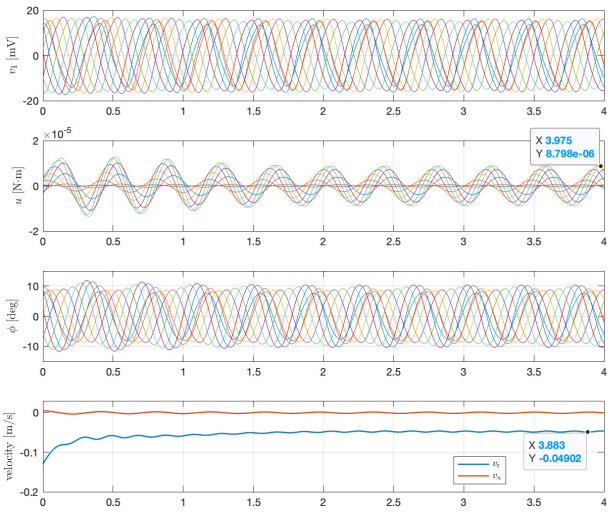

(a) v_1, u, ϕ and center mass velocity

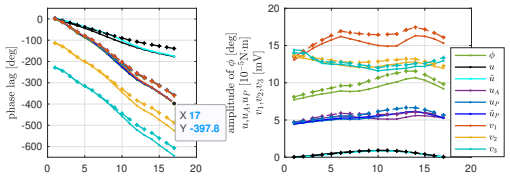

(b) Solid: phase and amplitude of case 3; dashed: case 1

Figure 4.27: Simulation result for case 3 in comparison with case 1

As we can see from Table 4.1 and following plots, in Case 3, through $\mathring{Q}_2$ CPG modified the gaits to keep low input torque by lowering swimming speed and increase wave number during one cycle; whereas in Case 2 where there is no feedback to the CPG when $\mathring{Q}_2$ is set to be zero, the system is trying hard to maintain its original oscillatory gait and speed at a cost of doubled input torque.

4.3.3 Plant stabilization through muscle stiffness

As mentioned earlier, when $\mathring{Q}_2 = 0$, the CPG acts as the exogenous reference generator which drives the plant stabilized by feedback loop, Fig. 4.25. The reference tracking would be achieved by stability of the feedback system consisting of the plant and muscle stiffness component.

To be more specific, showed in Fig. 4.24, the plant itself is unstable, having eigenvalues with positive real parts. When the dynamics of muscle stiffness $K(s) = c_m s + k_m$ added into the

loop, it helps stabilize the system under disturbance.

4.3.3.1 Simulation verification: the stabilization effect of muscle stiffness under disturbance

Here to verify the stabilization effect of muscle stiffness, we simulated Fig. 4.25. The initial conditions are the steady states of nominal swimming, except for u, ϕ and $\dot{\phi}$. For $t < 0.1s$, ϕ and $\dot{\phi}$ are set to be 0, u to be 10 times of nominal values, in order to mimic the situation where the leech is coming to a sudden stop due to large outer disturbance.

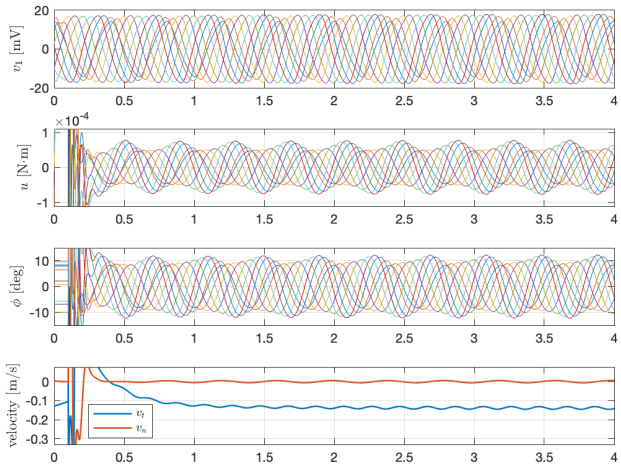

(a) v_1, u, ϕ and center mass velocity

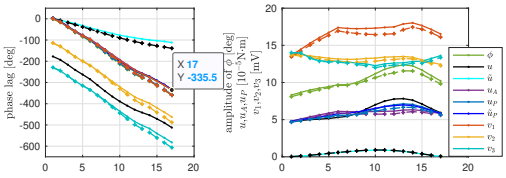

(b) Solid: phase and amplitude for disturbance case; dashed: case 1

Figure 4.28: Simulation result for disturbance when $\mathring{Q}_2 = 0$

As we can see from the figure above, u and ϕ go through huge disturbance at the beginning, and before 0.5s with the stabilizing effect from muscle stiffness in the feedback loop, both signals converge to steady states. In the phase plot on the right, at steady states, the phase lag is 335°, similar as case 2.

4.3.3.2 Stiffness control from another perspective

We can examine the mechanism of "plant stabilization through muscle stiffness" from the small gain theorem perspective. The closed-loop system can be decomposed into two parts of dynamics: $G_1(s)$ and $G_0(s)$, as shown in Fig. 4.29.

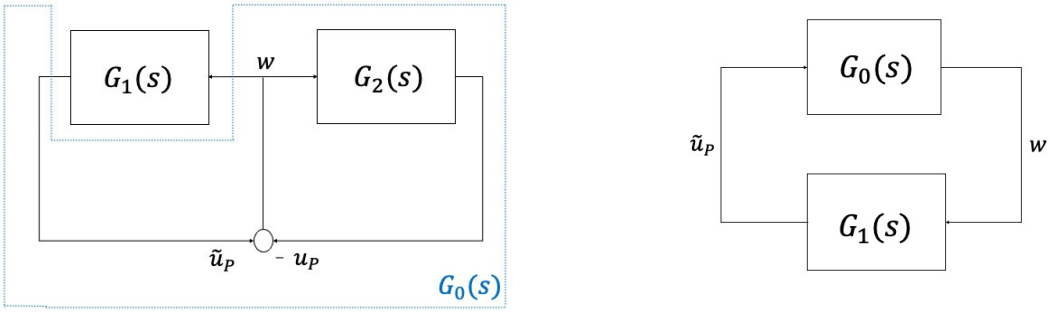

Figure 4.29: w converges to zero if $G_o(s)$ is stable and $G_1(s)$ is stable with small gain

We thought of two ways of decomposition shown in Fig. 4.30: the input to the first $G_o(s)$ is $\hat{u}_p$, to the second is $\hat{u}$, the output for both $G_o(s)$ is w. However, for the first decomposed, $G_o(s)$ is unstable, having infinite H-infinity norm. For the second decomposition, the H-infinity norm is finite, $\|H\|_\infty = 742.9$. $G_1(s)$ drives $G_o(s)$ with weak feedback $\hat{u}$ (in simulation the amplitude of u is 5 times smaller than that of $\hat{u}_p$ in steady state, a weaker feedback than the first decomposition).

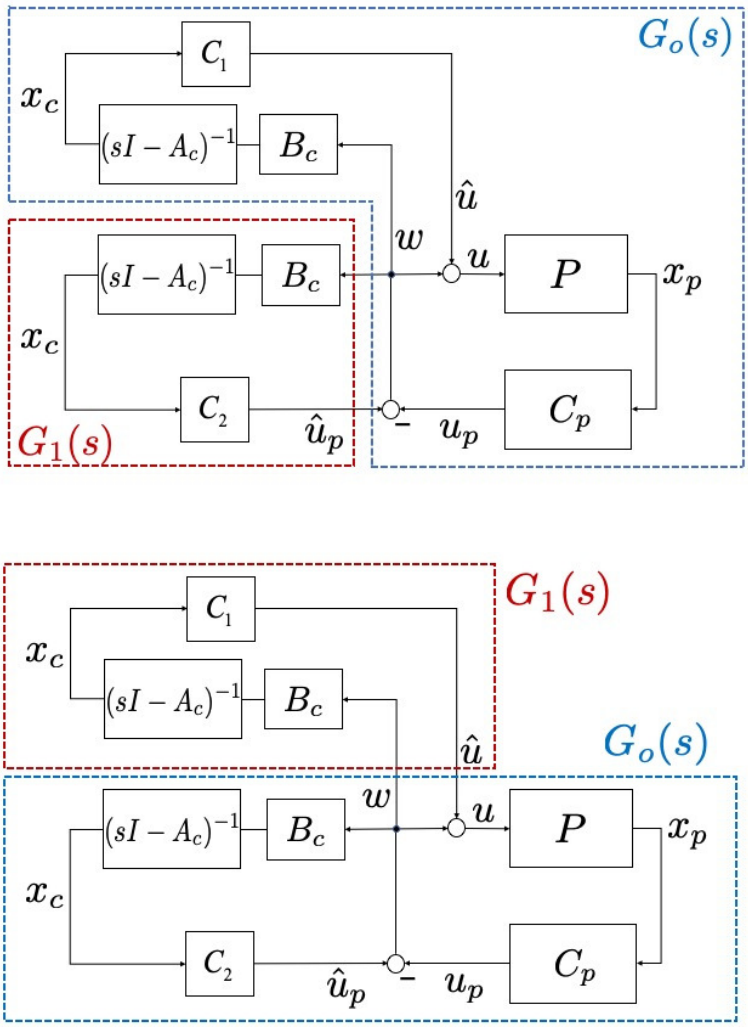

Figure 4.30: w converges to zero if $G_o(s)$ is stable and $G_1(s)$ is stable with small gain

Using (4.16), the state space realization of the second $G_o(s)$ can be described as

$$\begin{bmatrix} \dot{x}_p \\ \dot{x}_c \\ w \end{bmatrix} = \underbrace{\left[\begin{array}{cc|c} A_p - B_pC_p & B_pC_2 & B_p \\ -B_cC_p & A_c + B_cC_2 & 0 \\ \hline -C_p & C_2 & 0 \end{array}\right]}_{:=\left[\begin{array}{c|c} A_{G_o} & B_{G_o} \\ \hline C_{G_o} & 0 \end{array}\right]} \begin{bmatrix} x_p \\ x_c \\ \hat{u} \end{bmatrix} \tag{4.21}$$

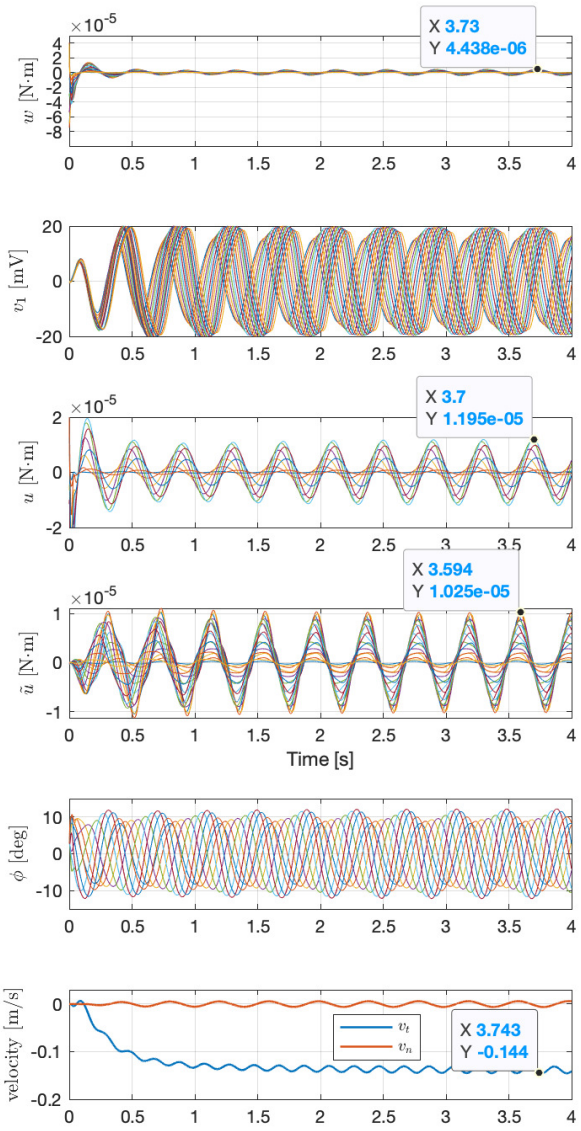

(a) Time domain signals

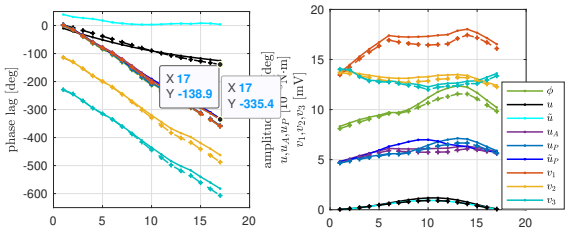

(b) Phase and amplitude, dashed: nominal closed-loop simulation

Figure 4.31: Results of simulation of $G_0(s)$

The stability of G_0 is verified in nonlinear simulation, where the w signal into G_1 is cut off.

G_1 works as a reference generator, whose initial states are set to be the steady states of nominal water swimming. The initial states of G_0 are set to be very close to zero.

From the figure above, the simulation shows that the stability of limit cycle of nominal water swimming in G_0. This is achieved by the muscle stiffness in the feedback loop.

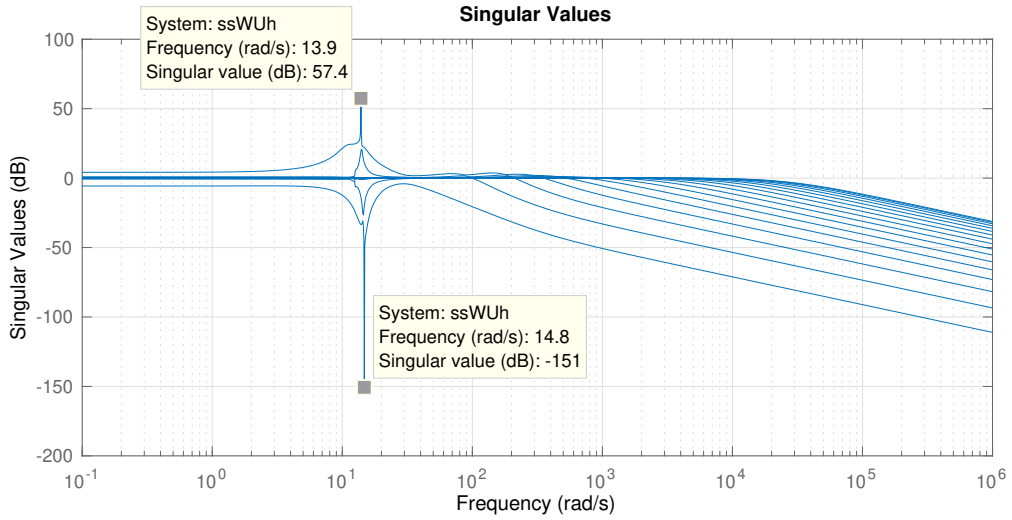

Figure 4.32: Singular values of $G_o(s)$ over frequency

One interesting observation is that the minimal singular value of $G_o(j\omega)$ hits the valley of -150 db at nominal oscillation frequency 14.8 Hz. This observation is consistent with the stability property of the second decomposition. For the second decomposition, the input-output relationship is

$$w = G_o(s)\tilde{u}. \tag{4.22}$$

Having the minimal singular value at -150 db means that $G_o(j\omega_o)$ has a zero eigenvalue at the nominal oscillation frequency ω_o:

$$G_o(j\omega_o)v_o = 0, \quad \tilde{u} = \mathrm{Re}(v_o e^{j\omega_o t}), \tag{4.23}$$

where v_o is the corresponding eigenvector. Combining (4.22) and (4.23), we will have $w = 0$.

According to

$$\min_{\hat{\tilde{u}}} \frac{||G_o(j\omega)\hat{\tilde{u}}||}{||\hat{\tilde{u}}||} = \sigma_{\min} \tag{4.24}$$

we plotted the minimal singular vector of $G_o(j\omega_o)$, which has the similar phase lag of 135 deg as the phasor of $\tilde{u}$. For the max singular value, it is not clear why the peak occurs at 13.9 Hz, very close to the nominal oscillation frequency.

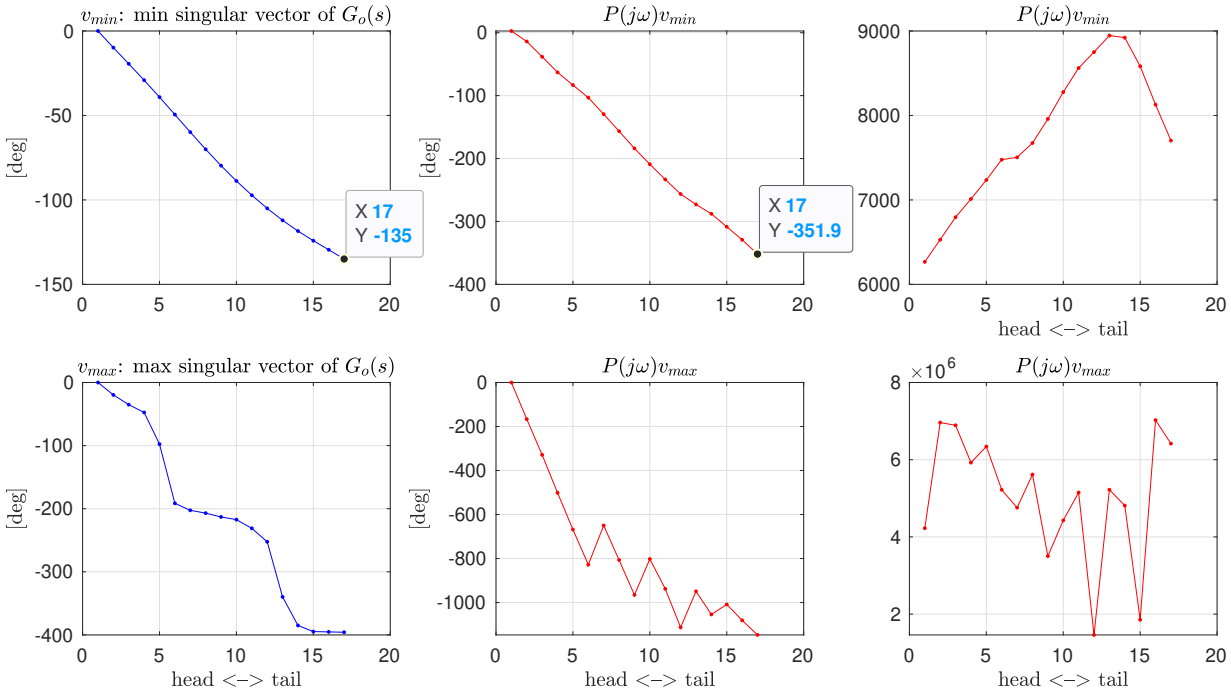

Figure 4.33: Left: minimal and maximal singular values of $G_o(s)$; middle: the phase lag of $P(j\omega)v_{\min}$ and $P(j\omega)v_{\max}$; right: amplitude of $P(j\omega)v_{\min}$ and $P(j\omega)v_{\max}$.

CHAPTER 5

CPG Inspired Control Design

This section use the prototype mechanical rectifier (PMR) as an example to demonstrate how we can utilize the diffusive coupling structure to design a CPG controller in a closed-loop setting.

5.1 Design guidelines

In this section, we suggest guidelines for designing a CPG-based controller for a mechanical system such that a desired oscillation (or a periodic orbit) is embedded in the closed-loop system as a stable limit cycle approximately. The guidelines are developed from the observations made on the leech CPG control model in the previous sections.

Step 1: Specify desired oscillation profile $(\omega_o, \hat{\phi})$ of the plant

Step 2: Find input u to the plant that can generate desired output ϕ in open-loop setting

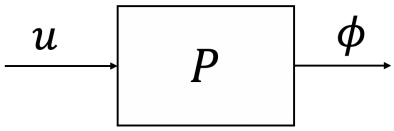

Figure 5.1: $C(s)$ Find proper input u that can generate desired output ϕ

Take the leech for example, the bending moment u and relative joint angels ϕ satisfy the

relation $\big(\mathcal{J}s^2 + \mathcal{D}s + v_t\mathcal{L}\big)\phi = u$, thus the nonlinear plant can be approximated by an LTI system, when we set the tangential velocity of center mass to be the nominal swimming speed v_o:

$$P(s) = \big(\mathcal{J}s^2 + \mathcal{D}s + v_o\mathcal{L}\big)^{-1}.$$

The phasor $\hat{u}$ at nominal swimming frequency can be obtained by:

$$\hat{u} = P(j\omega_o)^{-1}\hat{\phi}.$$

Step 3: Design CPG that can generate $\hat{v}$ with similar phase lag as $\hat{\phi}$ when there is no input

$$v = M_D(s)\varphi(v) + Bw \cong M_D(s)\varphi(v) \tag{5.1}$$

The subscript "D" in $M_D(s)$ denotes for "design". Take the leech case for example, $M_D := M(s) + BD(s)$. The problem now reduces to MHB design of CPG.

Problem 1. *Given $(\omega_o, \alpha, \beta) \in \mathbb{R} \times \mathbb{R}^n \times \mathbb{R}^n$, find $M \in \mathbb{R}^{n\times n}$ such that $v = f(s)M\varphi(v)$ has solution $v_i(t) \cong \alpha_i \sin(\omega_o t + \beta_i)$, where $f(s)$ is the cell membrane dynamics.*

For the choice of $f(s)$, we could use low-pass filter or band-pass filter. The implicit parametrization of M could be solved by LMI:

$$\begin{array}{ll} M\boldsymbol{\kappa}(\alpha)R = R\Omega & M\boldsymbol{\kappa}(\alpha)R = R\Omega \\ & \Rightarrow \\ \Re[\rho(N^\top M\boldsymbol{\kappa}(\alpha)N)] < 1 & (N^\top M\boldsymbol{\kappa}(\alpha)N) + (N^\top M\boldsymbol{\kappa}(\alpha)N)^\top < 2\gamma I \end{array}$$

where $R := \begin{bmatrix} v & \bar{v} \end{bmatrix}\Gamma, \Gamma := \frac{1}{2}\begin{bmatrix} -j & 1 \\ j & 1 \end{bmatrix}, \Omega := \Gamma^{-1}\begin{bmatrix} \lambda & 0 \\ 0 & \bar{\lambda} \end{bmatrix}\Gamma, \lambda := \frac{1}{f(j\omega_o)}, N^\top R = 0, N^\top N = I.$

Step 4: Design C_1 that takes v as input and generates $\tilde{u}$ which has the same oscillation profile as u

$$C_1(j\omega_o)\hat{v} = \hat{\tilde{u}} = \hat{u} \tag{5.2}$$

Step 5: Design C_2 that takes v as input and generates $\tilde{u}_P$ which has the same oscillation profile as the output of K

$$C_2(j\omega_o)\hat{v} = \hat{\tilde{u}}_P = \hat{u}_P \tag{5.3}$$

The design guidelines outlined above will be applied to a simple locomotion system to illustrate the design process and demonstrate its effectiveness later in this chapter.

5.1.1 Single limit cycle embedding

The single limit cycle embedding fits into the scenario where the PMR is expected to rotate under fixed environment, e.g. the friction coefficient at arm/disk contact c_c remains the same all the time.

The CPG design for single limit cycle embedding can directly follow 5.1.

5.1.2 Multiple limit cycles embedding

The multiple limit cycle embedding fits into the scenario where the PMR is expected to rotate under varying environments, e.g. the friction coefficient at arm/disk contact c_c changes.

The equation of the system can be described by:

$$\begin{cases} v = f(s)(M\varphi(v) + B_{sf}w) \\ w = C\varphi(v) - u_P \\ u = w + F\varphi(v) \\ u_P = P(s)u - K_d(s)\phi \end{cases} \tag{5.4}$$

where M is the constant connectivity matrix in CPG; B_{sf} is the sensory feedback matrix; F and C are constant matrices, taking in $\varphi(v)$ and generating $\hat{u}$ and $\hat{u}_P$ respectively.

The problem statement is the following.

Problem 2. *Given multiple sets of* $(\omega, \hat{u}, \hat{\phi})$ *(denoted by subscript* k*), find* M, B, C, F *with constraint* $\hat{w} = 0$*.*

First, let's write out the MHB equations for the quasi-linear system:

$$\begin{cases} \hat{v} = f(j\omega)M\boldsymbol{\kappa}(\alpha)\hat{v} \\ \hat{u}_P = C\boldsymbol{\kappa}(\alpha)\hat{v} \\ \hat{u} = F\boldsymbol{\kappa}(\alpha)\hat{v} \end{cases} \tag{5.5}$$

where $\hat{v} = \alpha\hat{\phi}$. α is determined so that the $||v||_\infty = 1$.

For each set of $(\omega, \hat{u}, \hat{\phi})$, if we separate the real and imaginary part of complex vectors in Eqn. (5.5) into real matrices, we will have

$$\begin{cases} V_k\Omega_k = M\boldsymbol{\kappa}_k V_k \\ U_{P_k} = C\boldsymbol{\kappa}_k V_k \\ U_k = F\boldsymbol{\kappa}_k V_k \end{cases} \tag{5.6}$$

where $\Omega := \Gamma^{-1}\begin{bmatrix} \lambda_o & 0 \\ 0 & \lambda_o^\top \end{bmatrix}\Gamma$, $\Gamma := \frac{1}{2}\begin{bmatrix} -j & 1 \\ j & 1 \end{bmatrix}$, $\lambda_o := j\omega_k\tau_o + 1$, $\tau_o = 0.1$ s, a tuning freedom. Using describing function to approximate $\varphi(v)$ in Eqn. (5.4), we can write out the quasi-linear system from u_P to u:

$$\begin{aligned} v &= f(s)(M + B_{sf}C)\boldsymbol{\kappa}v - f(s)B_{sf}u_P \\ u &= (C + F)\boldsymbol{\kappa}v - u_P \end{aligned} \tag{5.7}$$

Let's look at the equations for the original non-decomposed CPG of PMR:

$$\begin{aligned} v &= f(s)\Big(M_o\varphi(v) + B_{sf}u\Big) \\ u &= (C + F)\varphi(v) - u_P \end{aligned} \tag{5.8}$$

If we replace the static nonlinearity by describing function and replace u by the second line in Eqn. (5.8) and $u_P = C\varphi(v)$ in the steady states, we can obtain

$$v = f(s)\Big((M_o + B_{sf}F)\boldsymbol{\kappa}v\Big).$$

Let's put the above equation and the describing function approximation of the first line in Eqn. (5.4) side by side. When the system reaches steady states ($w = 0$), the equation of decomposed CPG of PMR becomes

$$v = f(s)M\boldsymbol{\kappa}v.$$

The above two equations can help us design CPG embedded multiple limit cycles. The idea is that: for each limit cycle, we will have a unique decomposed conservative CPG_c and corresponding connectivity matrix M_k, also the feed-forward matrix F_k and C_k; while the original non-decomposed CPG connectivity matrix M_o stays the same, so do the motoneuron dynamics and sensory feedback gain B_sf. For each of the decomposed CPG_c matrix M_k, it can be expressed by M_o and F_k. Then we can write out constraints for each of desired v_k, u_{P_k} and u_k:

$$\begin{aligned}
&M_1 - B_{sf}F_1 = M_2 - B_{sf}F_2 = ... = M_k - B_{sf}F_k = ... = M_l - B_{sf}F_l,\\
&C_1 + F_1 = C_2 + F_2 = ... = C_k + F_k = ... = C_l + F_l,\\
&V_k\Omega_k = M_k\boldsymbol{\kappa}_k V_k,\\
&U_{P_k} = C_k\boldsymbol{\kappa}_k V_k,\\
&U_k = F_k\boldsymbol{\kappa}_k V_k,\\
&(N^\top M_k\boldsymbol{\kappa}_k N_k) + (N^\top M_k\boldsymbol{\kappa}_k N_k)^\top < 0,\ k = 1, 2, ..., l
\end{aligned} \tag{5.9}$$

where N is the null space of $V^\top$, satisfying $N^\top[V\ N] = [O\ I]$.

The aim is to solve for M_k, C_k, F_k, B_{sf} using LMI. However, the first line of Eqn. (5.9) is not linear in variable B_{sf} and F_k. Here we restrict $B_{sf} = B_oG$, with B_o fixed and G being

a square variable matrix. Suppose there are m segments in the PMR, and r neurons per segment, therefore matrix $B \in \mathbb{R}^{mr \times m}$. One reasonable choice could be

$$B_o = \begin{bmatrix} b & 0 \\ 0 & b \end{bmatrix}, \; b = \begin{bmatrix} 1 \\ 1 \\ 1 \end{bmatrix}$$

when $m = 2$, $r = 3$. Therefore, the LMI formulation is the below:

Process a

Fix $\hat{v}$ and B_o, solve:

$$\begin{aligned} & U_{P_k} + U_k = \boldsymbol{E}\kappa_k V_k, \\ & V_k \Omega_k = (\boldsymbol{M_o} + B_o \bar{\boldsymbol{F}}_{\boldsymbol{k}})\kappa_k V_k, \\ & \mathbf{He}\Big(N^\top (\boldsymbol{M_o} + B_o \bar{\boldsymbol{F}}_{\boldsymbol{k}})\kappa_k N_k\Big) < \gamma I, \\ & \boldsymbol{G} U_k = \bar{\boldsymbol{F}}_{\boldsymbol{k}} \kappa_k V_k \end{aligned} \tag{5.10}$$

where $\bar{\boldsymbol{F}}_{\boldsymbol{k}} := \boldsymbol{G}F_k$, $\boldsymbol{E} := F_k + C_k$, $\boldsymbol{M_o} := M_k - B_{sf}F_k$, the matrices in boldface are LMI variables. The original parameters can be constructed by

$$\begin{aligned} & F_k := \boldsymbol{G}^{-1} \bar{\boldsymbol{F}}_{\boldsymbol{k}}, \\ & C_k := \boldsymbol{E} - \boldsymbol{F_k}, \\ & M_k := \boldsymbol{M_o} + B_{sf} \boldsymbol{F_k}, \\ & B_{sf} := B_o \boldsymbol{G}. \end{aligned} \tag{5.11}$$

By making G an LMI variable, we improve the manual tuning method in finding sensory feedback B_{sf}.

5.2 PMR design example

Consider a mechanical system composed of a two-link arm and a rotating disk as shown in Fig. 5.2. The pivot O of the arm is fixed to the inertia frame; two joints O and A are attached with actuators to generate torques u_1 and u_2 and sensors to measure the angular displacements θ_1 and θ_2. The tip of the arm B is not fixed to, just touches, the disk, on which it can exert friction force. The center of the disk is affixed to the inertia frame through a bearing and the disk can rotate around C.

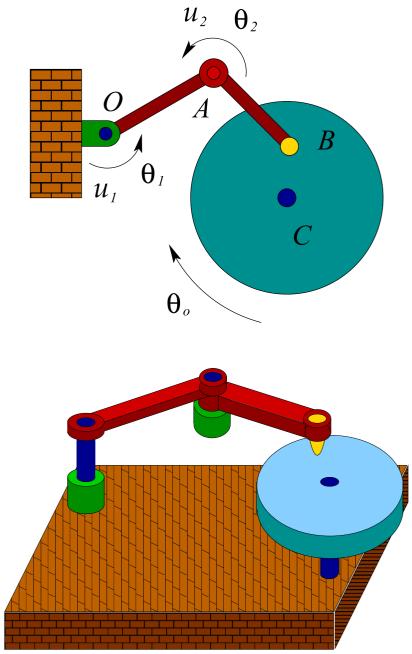

Figure 5.2: Prototype mechanical rectifier (PMR)

The intended movement of the system is to make the disk rotate at a desired angular velocity, through the rectifying friction force exerted at tip B. This property motivates us to call the system a prototype mechanical rectifier (PMR). The system captures the essential dynamics of many forms of animal locomotion. For example, the motion is analogous to human legs propelling a bicycle, but for the fact that tip B is not fixed to the pedal, adding one more

degree of freedom and some more complex dynamics.

5.2.1 PMR model

The differential equations governing the motion of the PMR are presented below. For simplicity, we impose the following:

Assumption 1.
- *Each link has a uniform mass distribution and both links have the same mass density and an identical shape (i.e., proportional dimensions).*
- *There are frictions at the disk bearing C and the contact point B between the disk and arm, and their magnitudes are proportional to the angular velocity of the disk and the relative velocity between the arm tip and point B on the disk, respectively.*

The equations of motion derived from Euler-Lagrange equation can be described as

$$\begin{aligned} &J_\theta \ddot{\theta} + G_\theta \dot{\theta}^2 + cR_\theta^\top (R_\theta \dot{\theta} + n_\theta \dot{\theta}_o) = Bu \\ &J_r \ddot{\theta}_o + cn_\theta^\top (R_\theta \dot{\theta} + n_\theta \dot{\theta}_o) + \dot{\theta}_o = 0, \end{aligned} \tag{5.12}$$

where the time axis has been scaled so that the derivative are with respect to the new variable $\tau := c_b t/J_1$,

$$\theta := \begin{bmatrix} \theta_1 \\ \theta_2 \end{bmatrix}, \quad u := \frac{J_1}{c_b^2} \begin{bmatrix} u_1 \\ u2 \end{bmatrix}, \quad c := \frac{c_c \ell_1^2}{c_b}, \quad \alpha := \frac{\ell_1}{\ell_2}, \quad J_r := \frac{J_o}{J_1}, \quad z_c := \begin{bmatrix} y_c/\ell_1 \\ -x_c/\ell_1 \end{bmatrix},$$

$$C_\theta := \begin{bmatrix} \cos\theta_1 & 0 \\ 0 & \cos\theta_2 \end{bmatrix}, \quad S_\theta := \begin{bmatrix} \sin\theta_1 & 0 \\ 0 & \sin\theta_2 \end{bmatrix}, \quad \Omega_\theta := \begin{bmatrix} \cos\theta_1 & \cos\theta_2 \\ \sin\theta_1 & \sin\theta_2 \end{bmatrix},$$

$$\ell := \begin{bmatrix} 1 \\ \alpha \end{bmatrix}, \quad \begin{matrix} R_\theta := \Omega_\theta L \\ n_\theta := \Omega_\theta \ell + z_c, \end{matrix} \quad J_\theta := J + S_\theta H S_\theta + C_\theta H C_\theta, G_\theta := S_\theta H C_\theta - C_\theta H S_\theta,$$

$$J := \begin{bmatrix} 1 & 0 \\ 0 & \alpha^5 \end{bmatrix}, \quad H := 3 \begin{bmatrix} 1+4\alpha^3 & 2\alpha^4 \\ 2\alpha^4 & \alpha^5 \end{bmatrix}, \quad L := \begin{bmatrix} 1 & 0 \\ 0 & \alpha \end{bmatrix}, \quad B := \begin{bmatrix} 1 & -1 \\ 0 & 1 \end{bmatrix},$$

Table 5.1: Variables and parameters of the PMR

θ_o	rotational angle of disk
θ_1, θ_2	link angles from downward vertical
u_1, u_2	torque inputs
ℓ_1, ℓ_2	link lengths
(x_c, y_c)	coordinate of disk center (O is the origin)
c_b	friction coefficient at disk bearing
c_c	friction coefficient at arm/disk contact
d	friction coefficient between links
J_o, J_1, J_2	moments of inertia for disk and links

and the variables and parameters are summarized in Table 5.1.

The term $cR_\theta^\top(R_\theta\dot{\theta} + n_\theta\dot{\theta}_o)$ and $cn_\theta^\top(R_\theta\dot{\theta} + n_\theta\dot{\theta}_o)$ are environmental forces applied on the disk.

We now consider a periodic link motion $\theta(t)$ about a nominal posture η, in which the tip B is placed at the center of the disk, and η is the nominal angles of the two links defined by $n_\theta = 0$. Assuming the oscillation around the nominal position is small $\vartheta := \theta(t) - \eta$, we can linearize Eqn. (5.12) by expanding each expression into its Taylor series in terms of ϑ, and keeping up to the first order terms. However the essential dynamics for rectification turns out to be embedded in the second or higher order terms in the second equation of Eqn. (5.12), and hence the linearized model fails to capture the locomotion dynamics. For this reason, we choose to linearize the first equation in terms of the linear term in ϑ and its derivatives, but keep up to the quadratic terms of ϑ and $\dot{\vartheta}$ in the second equation.

$$J_\theta \cong J_\eta := J + S_\eta H S_\eta + C_\eta H C_\eta, \quad n_\theta \cong v_\vartheta := \Omega_1 L \vartheta, \quad R_\theta \cong (\Omega_o + \Omega_1 \Theta) L$$

$$\Omega_o := \begin{bmatrix} \cos\eta_1 & \cos\eta_2 \\ \sin\eta_1 & \sin\eta_2 \end{bmatrix}, \quad \Omega_1 := \begin{bmatrix} -\sin\eta_1 & -\sin\eta_2 \\ \cos\eta_1 & \cos\eta_2 \end{bmatrix}, \quad \Theta := \begin{bmatrix} \vartheta_1 & 0 \\ 0 & \vartheta_2 \end{bmatrix}.$$

From these we obtain

$$\begin{aligned} & J_\eta \ddot{\vartheta} + D\dot{\vartheta} + \omega_o \Lambda \vartheta = Bz \\ & J_r \dot{\omega}_o + \left(1 + c\,\|v_\vartheta\|^2\right) \omega_o + \dot{\vartheta}^\top \Lambda \vartheta = 0 \\ & u_P = k\phi + d\dot{\phi} := K_d(s)\phi \\ & \phi = B^\top \vartheta \end{aligned} \tag{5.13}$$

where ω_o is assumed not necessarily small and

$$D := D_1 + B D_2 B^\top, \quad \Lambda := c\alpha \sin(\eta_2 - \eta_1) \begin{bmatrix} 0 & -1 \\ 1 & 0 \end{bmatrix}$$

$$D_1 := c \begin{bmatrix} 1 & \alpha\cos(\eta_2 - \eta_1) \\ \alpha\cos(\eta_2 - \eta_1) & \alpha^2 \end{bmatrix}, \quad D_2 = \mathrm{diag}(d).$$

5.2.2 Optimal gait analysis

The objective here is to minimize the input power.

$$\min_{\substack{T \in R_+ \\ \vartheta, z \in P_T}} \frac{1}{T} \int_0^T \dot{\vartheta}^\top B z dt \quad \text{s.t.} \begin{cases} \int_0^T \omega_o dt = \nu \\ J_\eta \ddot{\vartheta} + D\dot{\vartheta} + \omega_o \Lambda \vartheta = Bz \end{cases} \tag{5.14}$$

where ν is the desired angular velocity of the disk.

If we define

$$
\begin{aligned}
X(\omega) &:= \frac{1}{2}\begin{bmatrix} P(\omega) \\ I \end{bmatrix}^{*} \Pi(j\omega) \begin{bmatrix} P(\omega) \\ I \end{bmatrix} \\
Y(\omega) &:= P(\omega)^{*}\left(S(\omega) - \nu Q_1\right) P(\omega)/\left(2\nu\right) \\
S(\omega) &:= j\omega\left(\Lambda - \Lambda^{\top}\right)/2 \\
P(\omega) &:= \left(\nu\Lambda + j\omega D - \omega^2 J_\eta\right)^{-1} B \\
\Pi(j\omega) &:= \frac{1}{2}\begin{bmatrix} 0 & -j\omega B \\ j\omega B^{\top} & 0 \end{bmatrix} \\
Q_1 &:= c(\Omega_1 L)^{\top}(\Omega_1 L)
\end{aligned}
\tag{5.15}
$$

Then the solution to the original problem(5.14) is approximately given by the 2nd equation in (5.16) where $(\omega, \hat{z})$ is the solution to the 1st equation in (5.16).

$$
\begin{aligned}
&\min_{\omega\in\mathbb{R},\hat{z}\in\mathbb{C}^{\ell h}} \{\hat{z}^{*} X(\omega)\hat{z} : \hat{z}^{*} Y(\omega)\hat{z} = 1\} \\
&\hat{\vartheta} = P(\omega)\hat{z}.
\end{aligned}
\tag{5.16}
$$

When optimization process completes, the input torque phasor $\hat{u}$ can be constructed from $\hat{z}$ and ϑ:

$$
\hat{u} = \hat{z} - D_2 B^{\top} j\omega\hat{\theta}. \tag{5.17}
$$

5.2.3 Design results

Here is the simulation result of Eqn. (5.4) after Process a completes.

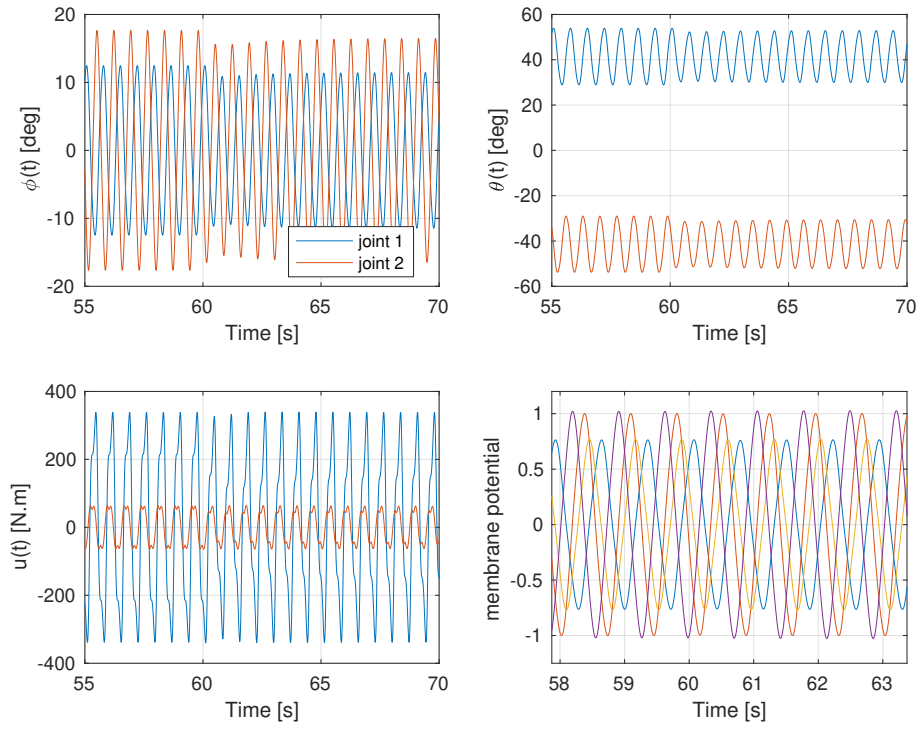

Figure 5.3: Time-domain signal in simulation of nonlinear system in Eqn. (5.4)

In the simulation configuration, at $t = 60$ s the contact damping c_c changed from 30 to 50, mimicking some environmental variation, for example the transition from aquatic to terrestrial locomotion. We see in Fig. 5.3), after $t = 60$ s the amplitude of relative joint angle ϕ immediately decreased. This amplitude drop is expected, because when the contact damping increase, the arm of the PMR shall have lower angular displacement to achieve the same rotating speed of the disc.

In Fig 5.4, the red curve is the optimal trajectory when $c_c = 30$, blue when $c_c = 50$. Yellow curve is the simulated trajectory. The initial condition is on the red curve. After $t = 60$ s when contact damping changed, we can see the yellow curve made transition to blue in the upper part of the figure.

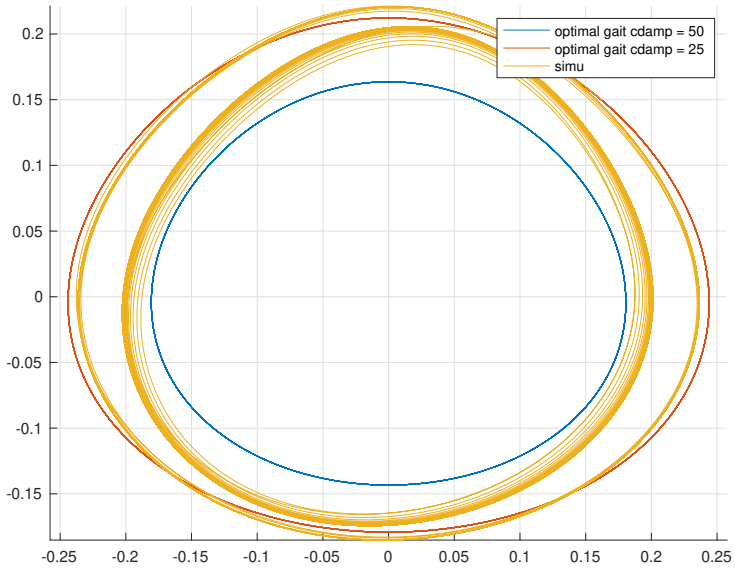

Figure 5.4: Tip trajectory ρ

One thing to be noticed is that Eqn. (5.10) will yield reasonable results under the assumption that $w \cong 0$ in the steady states. These assumption requires G to have small L_2 norm, which will cause numerical error when calculating F_k and later C_k in Eqn. (5.11).

Using $\bar{F}_k = GF_k$ in Eqn. (5.11), we can avoid using variable $\bar{F}_k$:

Process $\tilde{\boldsymbol{a}}$

Fix $\hat{v}$ and B_o, solve:

$$
\begin{aligned}
& U_{P_k} + U_k = \boldsymbol{E}\boldsymbol{\kappa}_k V_k, \\
& V_k \Omega_k = (\boldsymbol{M_o} + B_o \boldsymbol{G}\boldsymbol{F_k})\boldsymbol{\kappa}_k V_k = \boldsymbol{M_o}\boldsymbol{\kappa}_k V_k + B_o \boldsymbol{G} U_k, \\
& \mathbf{He}\Big(N^\top (\boldsymbol{M_o} + B_o \boldsymbol{G}\boldsymbol{F_k})\boldsymbol{\kappa}_k N_k\Big) < \gamma I, \\
& U_k = \boldsymbol{F_k}\boldsymbol{\kappa}_k V_k
\end{aligned}
\tag{5.18}
$$

The original parameters can be constructed by:

$$\begin{aligned} C_k &:= \boldsymbol{E} - \boldsymbol{F_k}, \\ M_k &:= \boldsymbol{M_o} + B_{sf}\boldsymbol{F_k}, \\ B_{sf} &:= B_o\boldsymbol{G}. \end{aligned} \tag{5.19}$$

To confirm weak coupling assumption holds in steady states, we shall first make sure the LMI formulation with $G = 0$ can work as intended:

Process $\tilde{\boldsymbol{a}}_{\boldsymbol{o}}$

Fix $\hat{v}$ and B_o, solve:

$$\begin{aligned} U_{P_k} + U_k &= \boldsymbol{E}\boldsymbol{\kappa}_k V_k, \\ V_k\Omega_k &= \boldsymbol{M_o}\boldsymbol{\kappa}_k V_k, \\ \mathbf{He}\Big(N^\top(\boldsymbol{M_o})\boldsymbol{\kappa}_k N_k\Big) &< \gamma I. \end{aligned} \tag{5.20}$$

The connectivity matrix for decomposed CPG will be the same as the connectivity matrix M_o in the original CPG:

$$M_k := \boldsymbol{M_o} \tag{5.21}$$

When Process $\tilde{a}_o$ completed, the quasi-linear CPG-PMR system will be simulated:

$$\begin{cases} v = f(s)M_k\boldsymbol{\kappa}_k \\ w = C\boldsymbol{\kappa}_k - u_P \\ u = w + F\boldsymbol{\kappa}_k \\ u_P = P(s)u - K_d(s)\phi \end{cases} \tag{5.22}$$

Following is the simulation result for $k = 1$ (contact damping $c_c = 50$). The upper left figure is the relative joint angel $\phi(t)$, upper right is the angular displacement $\theta(t)$. The lower left is the input torque applied on the two joints. Lower left is the membrane potential signal $v(t)$. We see that the v is close to sinusoidal.

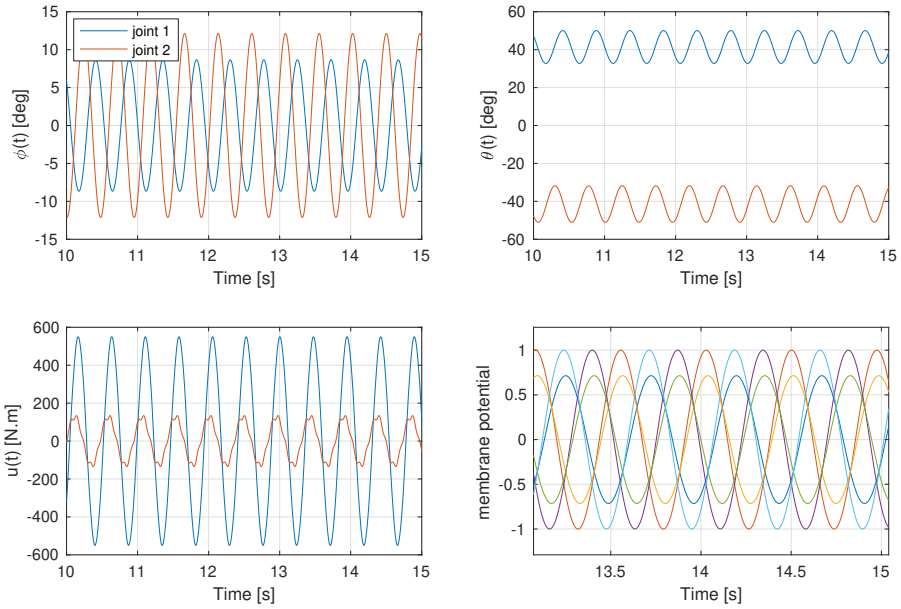

Figure 5.5: Time-domain signal in simulation of quasi-linear system in Eqn. (5.22)

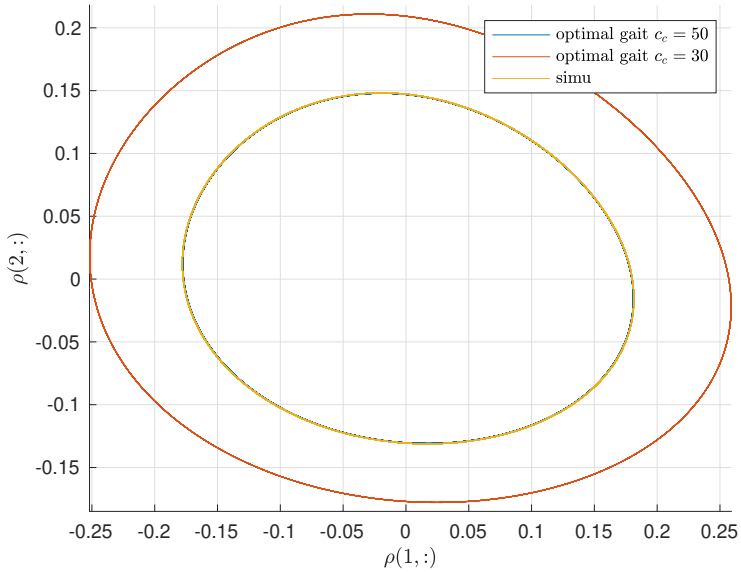

Figure 5.6: Tip trajectory ρ

Fig. 5.6 shows the tip trajectory ρ. The initial condition of the simulation is set to be on

the desired trajectory (blue), and we see the simulation result (yellow) overlaps with the desired blue trajectory, meaning that the CPG synthesized from Process $\tilde{a}_o$ can maintain stable oscillation on desired orbit in the quasi-linear CPG-PMR system.

When simulation is successful on quasi-linear system, we can move on simulating the non-linear system

$$\begin{cases} v = f(s)M_k\varphi(v) \\ w = C\varphi(v) - u_P \\ u = w + F\varphi(v) \\ u_P = P(s)u - K_d(s)\phi. \end{cases} \tag{5.23}$$

The following is the plot of time-domain signal $\phi(t)$, $\theta(t)$, $u(t)$, $v(t)$ and tip trajectory ρ.

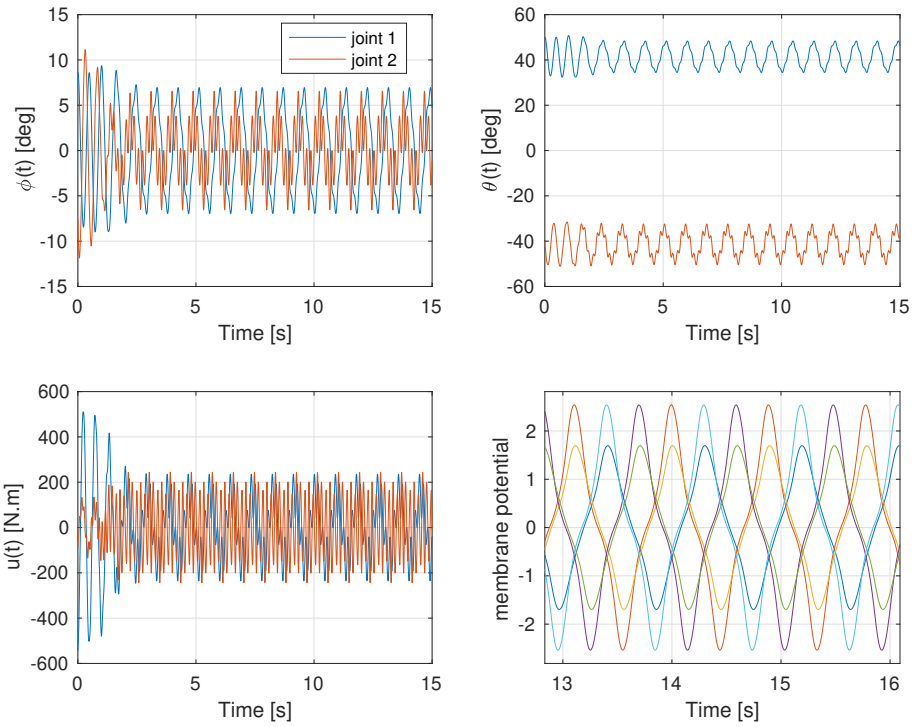

Figure 5.7: Time-domain signal in simulation of nonlinear system in Eqn. (5.23)

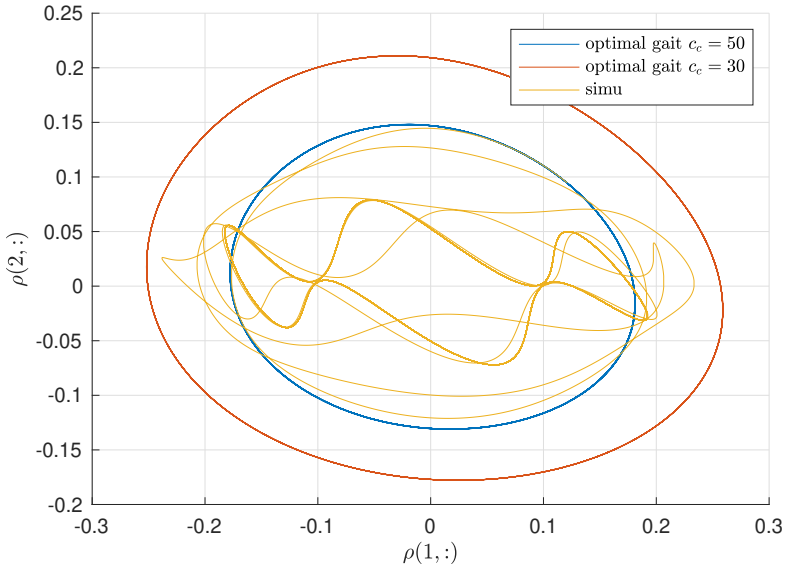

Figure 5.8: Tip trajectory ρ

We see that in Fig 5.7, the membrane potential $v(t)$ deviates a lot from sinusoidal signal. In Fig. 5.8, the simulated trajectory (yellow) failed to stay on the desired trajectory (blue) when the initial condition of the simulation is set to be on the desired trajectory. The reason is that MHB approximation in synthesis process is not accurate enough to represent the non-linear system in the simulation.

CHAPTER 6

Conclusion

6.1 Summary of contributions

This research aims to uncover the control mechanisms of CPG and generalize design guidelines of controllers for robotic systems.

The leech swimming CPG has demonstrated good adaptive and robust properties. Motivated by the desire for designing controllers capable of autonomous transitions or robust stability of limit cycles for robotic systems, we first simplified a fully nonlinear integrated model which captures observed leech behaviors well. The resulting model is more amenable to analytical study, and can reproduce almost identical behaviors as the original model under nominal water and perturbed air conditions.

With a model suitable for analytical study, we obtained results in oscillation profile estimation and coupled oscillator analysis with mechanical linkage. To analyze the closed-loop system, we proposed a numerical algorithm to solve the MHB equation and estimate the oscillation profile. The MHB analysis allowed for study of CPG control mechanisms from the quasi-linear perspective using the controller transfer function $C(s)$. We have found that (i) the neuronal threshold nonlinearity acts as amplitude-dependent gains to adjust $C(s)$ and achieve robustness and adaptivity, and (ii) the CPG control acts as a spatial notch filter to block the desired mode shape by aligning it with the minimum singular vector of $C(s)$, with high-gain feedback under perturbation for fast recovery. These analysis provides insights for designing CPG-inspired controllers, as an input-output operator. To understand effect of

mechanical linkage on the closed-loop system, coupled oscillator analysis are performed in this chapter. We found that strength of mechanical connection are about the same as the neural connection. The effect of mechanical linkage are stronger in the anterior portion than posterior portion of in leech system.

To further understand the internal architecture of CPG, we decomposed the CPG in Chapter 3 into a conservative oscillator and two feed-forward components, using LMI techniques. The conservative oscillator takes no input in the steady states, and generate membrane potential v with 360^o phase lag, which is the desired phase lag for relative joint angle ϕ for leeches. Unlike traditional control using exogenous reference generator sending out reference signal as a function of time, conservative CPG acts as an internal reference generator, and the reference is a function of system states, providing the foundation for adaptivity property. Besides the internal model structure, this decomposition also revealed the weak coupling structure, essential for stability. When the coupling is nonzero but small, the stability property is maintained due to continuity of the eigenvalues, and the CPG (reference generator) receives sensory feedback from the plant through the weak coupling so that the target oscillation pattern can be modified under perturbations. When the coupling connection is zero, the CPG acts as the exogenous reference generator which drives the plant stabilized by feedback loop. The reference tracking would be achieved by stability of the feedback system consisting of the plant and muscle stiffness component. The proof for the necessary and sufficient condition for the stability of the quasi-linear eigenstructure system is given in this chapter.

By uncovering the control mechanism of CPG from decomposition, insights are gained for designing controllers to achieve orbital stability for robotic systems. The weak coupling eigenstructure discovered in Chapter 4 made the design process a lot more straightforward than current existing methods. After specifying desired oscillation profile $(\omega, \hat{\phi})$ of the plant, we can synthesize the conservative CPG assuming weak feedback input. This synthesis can avoid the constraints on the dynamics of either complex or simple but with low fidelity model, making the process direct. In Chapter 5, we take PMR as the design example,

showing single and multiple stable limit cycles can be embedded in the CPG with only one connectivity matrix. The simulation confirms the orbital stability and adaptivity of the closed-loop CPG-PMR system. We saw automatic transition from one desired orbit to another under environmental variations, which shows the synthesized CPG demonstrated the adaptive property as in the biological CPGs.

This research proposed an integrated model amenable for theoretical study, also capable of reproducing adaptive behavior of actual leech undulation in both water and air. Using this model, the internal architecture of CPG was explored, which has never been studied before. The conservative oscillator and weak coupling structure were discovered. In current state of knowledge, the mechanism that how CPGs achieve and maintain orbital stability under perturbations, and how CPGs adjust trajectories under environmental perturbations are unknown to us. This conservative oscillator and weak coupling architecture can well-explain the CPG control mechanism of stabilization and trajectory re-planning. For applications to the community, today's design of CPG controller in robotic system relies heavily on manual tuning of the the sensory feedback or mere open-loop control, lack of established theoretical support. The synthesis also needs to take the complex dynamics of the plant into consideration, which makes the design computationally inefficient. Based on the newly-found architecture in this research, several design guidelines are generalized to embed multiple targeted orbits, with analytically determined sensory feedback gains.

6.2 Future directions

This research also laid a good foundation for future analysis.

First, the study in Chapter 5 shows the limitation of MHB analysis. The marginal stability of the quasi-linear system (linearized by describing function) is not a sufficient condition for the orbital stability of the nonlinear system. The discrepancy results from the sinusoidal approximation of the original periodic signals. The approximation is valid when the original

signal is close to sinusoids. In the later study, one should develop additional mathematical tools amenable for analyzing nonlinear systems with non-sinusoidal oscillation profiles.

Second, the current model of CPG is an abstraction of the biological leech CPGs. In each of the segmental oscillator, 3 neurons with 120^o phase lag apart is a functional abstraction of the actual 13 neurons in each of the ganglion in leech CPGs. This abstraction can reproduce traveling wave undulation in water and air, and standing wave oscillation in air. It can also generates the adaptive behavior of real leeches: automatic gait transition when environment settings is changed from water to air. However, this 3-neuron representation does not capture the robustness properties observed in leeches. The leech yield undulatory movement in the posterior half when the body is cut at the mid body. When the nerve cord is severed in the middle, the leech can maintain traveling wave undulation in water, the oscillation profile of which is similar to intact nerve cord cases. These observations were not reproduced by the integrated model with the CPG model described in this dissertation. More realistic representation of the CPG should be explored later, based on the weakly coupled CPG structure identified in this research.

Bibliography

[1] A. L. Hodgkin and A. F. Huxley, "A quantitative description of membrane current and its application to conduction and excitation in nerve," *The Journal of physiology*, vol. 117, no. 4, pp. 500–544, 1952.

[2] B. Francis and W. Wonham, "The internal model principle of control theory," *Automatica*, vol. 12, no. 5, pp. 457–465, 1976.

[3] F. Delcomyn, "Neural basis of rhythmic behavior in animals," *Science*, vol. 210, no. 4469, pp. 492–498, 1980.

[4] Y. Arshavsky, I. Beloozerova, G. Orlovsky, Y. Panchin, and G. Pavlova, "Control of locomotion in marine mollusc clione limacina i. efferent activity during actual and fictitious swimming," *Experimental brain research*, vol. 58, no. 2, pp. 255–262, 1985.

[5] K. Matsuoka, "Sustained oscillations generated by mutually inhibiting neurons with adaptation," *Biological cybernetics*, vol. 52, no. 6, pp. 367–376, 1985.

[6] P. D. Brodfuehrer and W. O. Friesen, "From stimulation to undulation: A neuronal pathway for the control of swimming in the leech," *Science*, vol. 234, pp. 1002–1005, 1986.

[7] Y.-Q. Ye, Y. Ye, Y.-c. Yeh, S.-l. Cai, and C. Lan-sun, *Theory of limit cycles*. American Mathematical Soc., 1986, vol. 66.

[8] K. Matsuoka, "Mechanisms of frequency and pattern control in the neural rhythm generators," *Biological cybernetics*, vol. 56, no. 5, pp. 345–353, 1987.

[9] A. Cohen, S. Rossignol, S. Grillner, *et al.*, *Neural control of rhythmic movements in vertebrates*. Wiley, 1988.

[10] R. Pearce and W. Friesen, "A model for intersegmental coordination in the leech nerve cord," *Biological cybernetics*, vol. 58, no. 5, pp. 301–311, 1988.

[11] A. Jean, "Brainstem control of swallowing," *Localization and organization of the central pattern generator*, pp. 294–321, 1989.

[12] A. Isidori and C. Byrnes, "Output regulation of nonlinear systems," *IEEE transactions on Automatic Control*, vol. 35, no. 2, pp. 131–140, 1990.

[13] T. McGeer *et al.*, "Passive dynamic walking," *I. J. Robotic Res.*, vol. 9, no. 2, pp. 62–82, 1990.

[14] S. Grillner, P. Wallen, L. Brodin, and A. Lansner, "Neuronal network generating locomotor behavior in lamprey: Circuitry, transmitters, membrane properties, and simulation," *Annual review of neuroscience*, vol. 14, no. 1, pp. 169–199, 1991.

[15] J.-J. E. Slotine, W. Li, *et al.*, *Applied nonlinear control*, 1. Prentice hall Englewood Cliffs, NJ, 1991, vol. 199.

[16] G. Taga, Y. Yamaguchi, and H. Shimizu, "Self-organized control of bipedal locomotion by neural oscillators in unpredictable environment," *Biological cybernetics*, vol. 65, no. 3, pp. 147–159, 1991.

[17] J. Hellgren, S. Grillner, and A. Lansner, "Computer simulation of the segmental neural network generating locomotion in lamprey by using populations of network interneurons," *Biological cybernetics*, vol. 68, no. 1, pp. 1–13, 1992.

[18] W. Friesen and R. Pearce, "Mechanisms of intersegmental coordination in leech locomotion," in *Seminars in Neuroscience*, Elsevier, 1993, pp. 41–47.

[19] H. Traven, L. Brodin, A. Lansner, O. Ekeberg, P. Wallén, and S. Grillner, "Computer simulations of nmda and non-nmda receptor-mediated synaptic drive: Sensory and supraspinal modulation of neurons and small networks," *Journal of neurophysiology*, vol. 70, no. 2, pp. 695–709, 1993.

[20] H. Giacomini, J. Llibre, and M. Viano, "On the nonexistence, existence and uniqueness of limit cycles," *Nonlinearity*, vol. 9, no. 2, p. 501, 1996.

[21] N. G. Hatsopoulos and W. H. Warren Jr, "Resonance tuning in rhythmic arm movements," *Journal of motor behavior*, vol. 28, no. 1, pp. 3–14, 1996.

[22] K. Khalil, "Noninear systems," *Prentice-Hall, New Jersey*, vol. 2, no. 5, pp. 5–1, 1996.

[23] S. Grillner, Ö. Ekeberg, A. El Manira, A. Lansner, D. Parker, J. Tegner, and P. Wallen, "Intrinsic function of a neuronal network—a vertebrate central pattern generator," *Brain Research Reviews*, vol. 26, no. 2-3, pp. 184–197, 1998.

[24] C. Koch and I. Segev, *Methods in neuronal modeling: from ions to networks*. MIT press, 1998.

[25] M. M. Williamson, "Neural control of rhythmic arm movements," *Neural networks*, vol. 11, no. 7-8, pp. 1379–1394, 1998.

[26] I. Delvolvé, P. Branchereau, R. Dubuc, and J.-M. Cabelguen, "Fictive rhythmic motor patterns induced by nmda in an in vitro brain stem–spinal cord preparation from an adult urodele," *Journal of Neurophysiology*, vol. 82, no. 2, pp. 1074–1077, 1999.

[27] R. J. Full and D. E. Koditschek, "Templates and anchors: Neuromechanical hypotheses of legged locomotion on land," *Journal of experimental biology*, vol. 202, no. 23, pp. 3325–3332, 1999.

[28] H. Kimura, S. Akiyama, and K. Sakurama, "Realization of dynamic walking and running of the quadruped using neural oscillator," *Autonomous robots*, vol. 7, no. 3, pp. 247–258, 1999.

[29] G. Orlovski, T. Deliagina, and S. Grillner, *Neuronal control of locomotion: from mollusc to man*. Oxford University Press, 1999.

[30] E. Bizzi, M. C. Tresch, P. Saltiel, and A. d'Avella, "New perspectives on spinal motor systems," *Nature Reviews Neuroscience*, vol. 1, no. 2, pp. 101–108, 2000.

[31] M. H. Dickinson, C. T. Farley, R. J. Full, M. Koehl, R. Kram, and S. Lehman, "How animals move: An integrative view," *science*, vol. 288, no. 5463, pp. 100–106, 2000.

[32] J. Pratt, "Exploiting inherent robustness and natural dynamics in the control of bipedal walking robots," MASSACHUSETTS INST OF TECH CAMBRIDGE DEPT OF ELECTRICAL ENGINEERING and COMPUTER SCIENCE, Tech. Rep., 2000.

[33] A. Taylor, G. Cottrell, and W. Kristan, "A model of the leech segmental swim central pattern generator," *Neurocomputing*, vol. 32, pp. 573–584, 2000.

[34] E. Marder and D. Bucher, "Central pattern generators and the control of rhythmic movements," *Current biology*, vol. 11, no. 23, R986–R996, 2001.

[35] J. Cang and W. Friesen, "Model for intersegmental coordination of leech swimming: Central and sensory mechanisms," *Journal of Neurophysiology*, vol. 87, no. 6, pp. 2760–2769, 2002.

[36] M. Saito, M. Fukaya, and T. Iwasaki, "Serpentine locomotion with robotic snake," *IEEE Control Systems Magazine*, vol. 22, no. 1, pp. 64–81, 2002.

[37] M. Vidyasagar, *Nonlinear systems analysis*. SIAM, 2002.

[38] C. Byrnes and A. Isidori, "Limit sets, zero dynamics, and internal models in the problem of nonlinear output regulation," *IEEE Transactions on Automatic Control*, vol. 48, no. 10, pp. 1712–1723, 2003.

[39] J. Huang and Z. Chen, "A general framework for tackling the output regulation problem," *IEEE Transactions on Automatic Control*, vol. 49, no. 12, pp. 2203–2218, 2004.

[40] J. Nakanishi, J. Morimoto, G. Endo, G. Cheng, S. Schaal, and M. Kawato, "Learning from demonstration and adaptation of biped locomotion," *Robotics and autonomous systems*, vol. 47, no. 2, pp. 79–91, 2004.

[41] Z. Chen and J. Huang, "Robust output regulation with nonlinear exosystems," *Automatica*, vol. 41, no. 8, pp. 1447–1454, 2005.

[42] S. Collins, A. Ruina, R. Tedrake, and M. Wisse, "Efficient bipedal robots based on passive-dynamic walkers," *Science*, vol. 307, no. 5712, pp. 1082–1085, 2005.

[43] W. B. Kristan Jr, R. L. Calabrese, and W. O. Friesen, "Neuronal control of leech behavior," *Progress in neurobiology*, vol. 76, no. 5, pp. 279–327, 2005.

[44] S. Grillner, "Biological pattern generation: The cellular and computational logic of networks in motion," *Neuron*, vol. 52, no. 5, pp. 751–766, 2006.

[45] P. Holmes, R. J. Full, D. Koditschek, and J. Guckenheimer, "The dynamics of legged locomotion: Models, analyses, and challenges," *SIAM review*, vol. 48, no. 2, pp. 207–304, 2006.

[46] T. Iwasaki and M. Zheng, "Sensory feedback mechanism underlying entrainment of central pattern generator to mechanical resonance," *Biological cybernetics*, vol. 94, no. 4, pp. 245–261, 2006.

[47] L. Righetti and A. Ijspeert, "Programmable central pattern generators: An application to biped locomotion control," *IEEE Int. Conf. Robotics and Automation*, pp. 1585–1590, 2006.

[48] C. Christopher and C. Li, *Limit cycles of differential equations*. Springer Science & Business Media, 2007.

[49] A. Ijspeert, A. Crepsi, D. Ryczko, and J. Cabelguen, "From swimming to walking with a salamander robot driven by a spinal cord model," *Science*, vol. 315, no. 5817, pp. 1416–1420, 2007.

[50] B. Verdaasdonk, H. F. Koopman, and F. C. Van der Helm, "Resonance tuning in a neuro-musculo-skeletal model of the forearm," *Biological Cybernetics*, vol. 96, no. 2, pp. 165–180, 2007.

[51] C. A. Williams and S. P. DeWeerth, "A comparison of resonance tuning with positive versus negative sensory feedback," *Biological cybernetics*, vol. 96, no. 6, pp. 603–614, 2007.

[52] M. Zheng, W. Friesen, and T. Iwasaki, "Systems-level modeling of neuronal circuits for leech swimming," *Journal of computational neuroscience*, vol. 22, no. 1, pp. 21–38, 2007.

[53] ——, "Systems-level modeling of neuronal circuits for leech swimming," *J. Computational Neuroscience*, vol. 22, no. 1, pp. 21–38, 2007.

[54] Z. Chen, M. Zheng, W. Friesen, and T. Iwasaki, "Multivariable harmonic balance analysis of neuronal oscillator for leech swimming," *J. Computational Neuroscience*, vol. 25, no. 3, pp. 583–606, 2008.

[55] A. Ijspeert, "Central pattern generators for locomotion control in animals and robots: A review," *Neural networks*, vol. 21, no. 4, pp. 642–653, 2008.

[56] T. Iwasaki, "Multivariable harmonic balance for central pattern generators," *Automatica*, vol. 44, no. 12, pp. 3061–3069, 2008.

[57] C. Chevallereau, J. W. Grizzle, and C.-L. Shih, "Asymptotically stable walking of a five-link underactuated 3-d bipedal robot," *IEEE transactions on robotics*, vol. 25, no. 1, pp. 37–50, 2009.

[58] W. Friesen, "Central pattern generators: Sensory feedback," 2009.

[59] P. A. Guertin, "The mammalian central pattern generator for locomotion," *Brain research reviews*, vol. 62, no. 1, pp. 45–56, 2009.

[60] J. Tian, T. Iwasaki, and W. Friesen, "Analysis of impulse adaptation in motoneurons," *Journal of Comparative Physiology A*, vol. 196, pp. 123–136, 2009.

[61] J. Chen, W. Friesen, and T. Iwasaki, "Mechanisms underlying rhythmic locomotion: Body-fluid interaction in undulatory swimming," *J. Exp. Biol.*, vol. 214, no. 4, pp. 561–574, 2011.

[62] J. Chen, J. Tian, T. Iwasaki, and W. Friesen, "Mechanisms underlying rhythmic locomotion: Dynamics of muscle activation," *J. Exp. Biol.*, vol. 214, no. 11, pp. 1955–1964, 2011.

[63] T. Iwasaki, J. Chen, and W. Friesen, "Biological clockwork underlying adaptive rhythmic movements," *Proceedings of the National Academy of Sciences*, vol. 111, no. 3, pp. 978–983, 2014.

[64] S. Kohannim and T. Iwasaki, "Dynamical model and optimal turning gait for mechanical rectifier systems," *IEEE Trans. Auto. Contr.*, vol. 62, no. 2, pp. 682–693, 2017.